UPC - Universitat Politècnica de Catalunya

Doctoral Thesis

Quantum control of single spin excitations in cold atomic quantum memories

Author:
Boris Albrecht

Supervisor:
Prof. Dr. Hugues de Riedmatten

A thesis submitted in fulfilment of the requirements for the degree of Doctor of Philosophy

in the

QPSA - Quantum Photonics with Solids and Atoms *group*,
ICFO - The Institute of Photonic Sciences

October 2015

"If an apple is magnified to the size of the earth,
then the atoms in the apple are approximately the size
of the original apple."

Richard Feynman

Abstract

Optical quantum memories are important devices in quantum information science. In particular, they are building blocks of quantum repeater architectures that have been proposed to increase the range of quantum communication beyond the limits set by losses in optical fibers. In this thesis, we report experiments with a quantum memory based on cold atoms. We focus on two important aspects relevant for using the memories as quantum repeater nodes: the connectivity to the optical fiber network, and the ability to operate in a time-multiplexed fashion.

The core of the work presented in this thesis was the implementation of a quantum memory based on spontaneous Raman scattering, following the protocol of Duan, Lukin, Cirac and Zoller (DLCZ). The memory is implemented with a cold ensemble of ^{87}Rb atoms loaded in a magneto optical trap. Single collective atomic spin excitations (spin-waves) are created in a heralded manner, before being retrieved by conversion into strongly non-classically correlated single photons. Our system showed measured second-order cross-correlation function values up to 200, an inferred intrinsic retrieval efficiency inside the science chamber up to 44%, and a memory lifetime up to 55 μs.

Current realizations of DLCZ quantum memories present several limitations, reducing the maximum practical distance achievable for quantum repeaters based on these systems. We partially addressed two of them. The first one originates from high absorption in optical fibers at the operating wavelength of 780 nm. The second one is that current demonstrations only allow the creation of spin-waves in single temporal modes, limiting the entanglement generation rates in quantum repeaters protocols.

A good solution to alleviate the first limitation is to translate the wavelength of the generated single photons to the telecom C-band, where absorption is minimal, while preserving their quantum characteristics. For

this, we demonstrated an ultra-low-noise solid state photonic quantum interface based on an integrated-waveguide in a non-linear PPLN crystal. We converted heralded single photons emitted by the DLCZ quantum memory at 780 nm to the telecommunication wavelength of 1552 nm. We achieved a maximum signal-to-noise ratio of 80 for a mean input photon number of 1, allowing us to show significant non-classical correlations between the heralding and converted photons via the violation of the Cauchy-Schwarz inequality.

To address the second limitation, we demonstrated the first experimental steps towards the realization of a temporally multiplexed DLCZ-type quantum repeater node. We showed active control of the spin-waves created in our quantum memory by means of an external magnetic field gradient inducing an inhomogeneous broadening of the atomic hyperfine levels. Acting on this gradient allows active dephasing and rephasing of individual spin-waves, enabling spin-wave creation in multiple temporal modes and read out of a specific time-bin only. We showed that the active rephasing technique preserves the non-classical statistics of the heralded photons via the observation of anti-bunching. We then created spin-waves in two temporal modes and demonstrated selective read-out of only one of them with a selectivity up to 92%.

All these results pave the way towards the realization of future temporally multiplexed quantum repeater nodes based on the DLCZ protocol.

Resum

Les memòries quàntiques òptiques son dispositius importants en el camp científic de la informació quàntica. En particular, són peces fonamentals de les estructures de repetidors quàntics, les quals han estat proposades per tal d'incrementar la distància en la comunicació quàntica més enllà dels límits imposats per les pèrdues en fibres òptiques. En aquesta tesi mostrem experiments duts a terme amb una memòria quàntica basada en àtoms freds. Ens hem centrat en dos aspectes importants que són rellevants a l'hora d'usar les memòries com a nodes de repetidors quàntics: la connectivitat cap a la xarxa de fibres òptiques i l'habilitat d'operar amb multiplexació temporal.

La part central del treball presentat en aquesta tesi és la implementació d'una memòria quàntica basada en la dispersió Raman espontània, seguint el protocol de Duan, Lukin, Cirac i Zoller (DLCZ). La memòria és implementada en un conjunt d'àtoms de ^{87}Rb en una trampa òptico-magnètica. Excitacions individuals col·lectives d'espins atòmics (ones d'espín) són creades de manera anunciada, abans de ser recuperades en una conversió cap a fotons individuals amb fortes correlacions no-clàssiques. En el nostre sistema vam mostrar mesures de la funció de correlació creuada de segon ordre amb valors de fins a 200, una eficiència de recuperació intrínseca dins la cambra experimental de fins a un 44% i un temps de vida de la memòria de 55 μs.

Les realitzacions actuals de memòries quàntiques DLCZ presenten varies limitacions, les quals redueixen la distància màxima que els repetidors quàntics basats en aquests sistemes poden assolir. Nosaltres n'hem adreçat parcialment dues d'elles. La primera és originada per l'alta absorció en fibres òptiques de la longitud d'ona de 780 nm. La segona té a veure amb el fet que altres experiments actuals només permeten la creació d'ones d'espín en un únic mode temporal, limitant el ritme de la generació d'entrellaçament en protocols de repetidors quàntics.

Una bona solució per mitigar la primera limitació és traslladar la longitud d'ona dels fotons individuals, cap a la banda C de telecomunicacions en la que l'absorció és mínima, preservant les seves característiques quàntiques. Per això, vam demostrar l'operació d'una interfície fotònica quàntica d'estat sòlid amb un soroll ultra-baix basada en una guia d'ones integrada en un cristall PPLN. Vam convertir fotons individuals anunciats emesos per la memòria quàntica DLCZ a 780 nm cap a la longitud d'ona de telecomunicacions de 1552 nm. Vam aconseguir una relació senyal-soroll màxima de 80 per a un nombre mitjà incident de fotons de 1, permetent-nos mostrar correlacions no-clàssiques significatives entre el fotó anunciat i el convertit, mitjançant la violació de la desigualtat de Cauchy-Schwarz.

Per tal d'adreçar la segona limitació, vam demostrar els primers passos experimentals cap a la realització d'un node de repetidor quàntic de tipus DLCZ amb multiplexació temporal. Vam mostrar el control actiu d'ones d'espín creades a la nostra memòria quàntica, utilitzant un gradient de camp magnètic extern que indueix un eixamplament inhomogeni dels nivells atòmics hiperfins. Actuar en aquest gradient permet el desfasament i refasament actiu d'ones d'espín individuals, permetent crear ones d'espín en múltiples modes temporals i llegir només un mode temporal específic. Vam mostrar que la tècnica de refasament actiu preserva les estadístiques no-clàssiques dels fotons anunciats a través de l'observació d'anti-agrupament. Seguidament vam crear ones d'espín en dos modes temporals i vam demostrar la lectura selectiva de només un mode amb una selectivitat de fins a un 92%.

Tots aquest resultats obren la porta a la realització de futurs nodes de repetidors quàntics amb multiplexació temporal basats en el protocol DLCZ.

Acknowledgements

First I would like to I thank my thesis advisor Hugues de Riedmatten for giving me the opportunity to do the PhD on a very interesting topic, and this in a very nice group.

I thank all the members of the group, the current ones as well as the past ones.

I thank Giacomo for helping me in my very beginning in the lab and after.

I thank Matteo for helping me for an even longer time, and without whom my thesis work would have been much more challenging.

I thank Mustafa for his moustache, and for sparing me the trouble of being the very first member of the group to have to defend the PhD thesis.

I thank Joachim and Nicolas, thanks to whom I could speak french almost daily, so that I didn't forget it.

I thank Pau and Georg for taking over the experiment after I left.

I thank my family for their support, and to have pushed me towards doing studies, without which I would surely not have ended up doing what I do now.

I thank my friends, especially the ones which came to visit me during my stay in Barcelona, and the ones I met there and had such a great time with.

And finally, I thank Günther, to have produced such good music that I couldn't spend one day in the lab without listening to it.

Publications

B. Albrecht, P. Farrera, G. Heinze, M. Cristiani and H. de Riedmatten: *Controlled rephasing of single collective spin excitations in a cold atomic quantum memory*, Arxiv Prepr. 1501.07559 (2015).

B. Albrecht, P. Farrera, X. Fernandez-Gonzalvo, M. Cristiani and H. de Riedmatten: *A waveguide frequency converter connecting rubidium-based quantum memories to the telecom C-band*, Nat. Commun. **5**, 3376 (2014).

X. Fernandez-Gonzalvo, G. Corrielli, B. Albrecht, M. Grimau, M. Cristiani and H. de Riedmatten: *Quantum frequency conversion of quantum memory compatible photons to telecommunication wavelengths*, Opt. Express **21**, 19473 (2013).

Table of Contents

Abbreviations

AFC	**A**tomic **F**requency **C**omb
AOM	**A**cousto-**O**ptic **M**odulator
APD	**A**valanche **P**hoto**D**iode
ASE	**A**mplified **S**pontaneous **E**mission
BEC	**B**ose-**E**instein **C**ondensate
BSM	**B**ell **S**tate **M**easurement
CCD	**C**harge-**C**oupled **D**evice
CRIB	**C**ontrolled **R**eversible **I**nhomogeneous **B**roadening
DDG	**D**igital **D**elay **G**enerator
DFG	**D**ifference **F**requency **G**eneration
CW	**C**ontinuous **W**ave
DLCZ	**D**uan **L**ukin **C**irac **Z**oller
ECDL	**E**xternal **C**avity **D**iode **L**aser
EOM	**E**lectro-**O**ptic **M**odulator
EPR	**E**instein-**P**odolsky-**R**osen
FBG	**F**iber **B**ragg **G**rating
FFC	**F**requency **F**iltering **C**avity
FPGA	**F**ield-**P**rogrammable **G**ate **A**rray
FSR	**F**ree **S**pectral **R**ange
GEM	**G**radient **E**cho **M**emory

IGBT	**I**nsulated-**G**ate **B**ipolar **T**ransistor
IT	**I**nterrogation **T**ime
MOT	**M**agneto **O**ptical **T**rap
NV	**N**itrogen-**V**acancy
OD	**O**ptical **D**epth
PBS	**P**olarizing **B**eam-**S**plitter
PLL	**P**hase-**L**ocked **L**oop
PPLN	**P**eriodically **P**oled **L**ithium **N**iobate
QFC	**Q**uantum **F**requency **C**onversion
QFCD	**Q**uantum **F**requency **C**onversion **D**evice
QKD	**Q**uantum **K**ey **D**istribution
QM	**Q**uantum **M**emory
QR	**Q**uantum **R**epeater
RF	**R**adio-**F**requency
SFG	**S**um **F**requency **G**eneration
SPD	**S**ingle **P**hoton **D**etector
TDC	**T**ime-to-**D**igital **C**onverter
TOF	**T**ime **O**f **F**light
UHV	**U**ltra-**H**igh **V**acuum
WCS	**W**eak **C**oherent **S**tate

To my family and friends...

Chapter 1

Introduction

Quantum information science is currently a worldwide and very active research field [1], both theoretically and experimentally. It can be seen as the extension of classical information science to the quantum domain, where information encoding and processing obey different rules. The idea is to take advantage of phenomena that only emerge in quantum systems composed of single or ensembles of particles, notably states superposition, entanglement and quantum teleportation. The strong interest for this research field stems directly from its numerous applications. An important one is quantum computing [2], where those processes could allow to perform computationally-heavy tasks taking too long on classical computers, like factorization of large integers. Another one is quantum communication, where the ability to transmit quantum states over large distances will be important. It can be used for secure communications using quantum key distribution (QKD) [3], loophole-free Bell inequalities violation experiments which are of fundamental interest, and future quantum networks for example. Finally, a more practical reason is the miniaturization of the microprocessors used in classical computers, following Moore's law. The main factor for performance improvements is the shrinking of the size of the transistors, allowing to put more of them on the same surface, and to operate them at higher frequencies. However, once their size will become comparable with the dimensions of a few atoms, quantum effects will arise and strongly modify their behavior.

1.1 Quantum information

1.1.1 Qubits

Classical information is encoded on classical bits, taking either of two discrete values 0 or 1. Quantum information, on the other hand, is encoded on quantum bits, called qubits. In the Dirac notation, the state of a qubit can be written as

$$|\psi\rangle = \alpha\,|0\rangle + \beta\,|1\rangle\,, \tag{1.1}$$

where α and β are probability amplitudes, such that $|\alpha|^2 + |\beta|^2 = 1$, and $|0\rangle$ and $|1\rangle$ are two orthogonal basis states. From this, we see that the state of a qubit can take any value between $|0\rangle$ and $|1\rangle$. However, a direct measurement will always project this state onto one of the basis state, depending on the values of α and β. Also, qubits, unlike classical bits, are very sensitive to noise and perturbations that would destroy quantum superpositions.

The support of a qubit can be for example a single atom or ion, a collection of these, an isolated electron, or a photon. A photonic qubit can be encoded in various degrees of freedom, including polarization, photon number, time-bin or frequency. For polarization encoding, the basis states are orthogonal polarization components, like horizontal and vertical for example. The basis for photon number encoding consists of the vacuum and single photon components of a Fock state. Time-bin qubits are encoded in the *early* and *late* time of arrival basis.

1.1.2 Quantum computing and quantum communication

Qubits can be separated into stationary and flying qubits, each corresponding to different applications. The support for stationary qubits can be single atoms in high finesse cavities, ions in electric traps, isolated electrons in NV centers or atomic ensembles for example. They need to be strongly interacting with external fields used to manipulate them, in order to allow an efficient implementation of the operations necessary for quantum computing. These operations are mostly manipulation of the state of qubits by single-qubit rotations, and interactions between pairs of qubits via two-qubit logic gates, like the controlled-NOT gate [4]. Stationary qubits are also used to store quantum information.

The purpose of flying qubits is to be transmitted rapidly over large distances without being absorbed or scattered, which is why they are usually encoded on photons, due to their low interaction with matter. This is not

a trivial problem, since one has to deal with the transfer of single photons over long distances without losing them, destroying them, or even disturbing them. They can serve as quantum information carriers per se as in QKD, or also be used as an interface between several stationary qubits in quantum networks.

The most straightforward way to transmit flying qubits is direct transmission in communication channels which are usually free-space or optical fibers. In atmospheric free-space communication, the distances are limited by the beam divergence, atmospheric perturbations and the need to have a free line of sight. However, this seems to be a promising approach for future inter-satellites quantum communication in space [5], between a ground station and a satellite, or between two mobile stations not too far apart on Earth.

When free-space transmission is not possible, optical fibers are an excellent alternative. The main limiting factor for the distance in this case are losses by absorption or scattering. The losses in the telecom C-band are $\sim 0.2\,\mathrm{dB/km}$, leading to a transmission of 1% after only 100 km. Considering a single photon source with an optimistic rate of 10 GHz, the photon rate after 500 km would be only 1 Hz, and as low as 10^{-10} Hz after 1000 km. This currently limits the operational distance of protocols such as QKD to a few hundreds of kilometers only [6]. In the case of classical information encoded on bright light pulses, classical repeaters are used to overcome this limitation, where the incoming signal is amplified before further transmission. When dealing with quantum information, this is impossible without adding noise to the transmitted states, as explained by the no-cloning theorem [7]. It states that an unknown arbitrary quantum state can not be copied without errors. A potential solution have been proposed in 1998 [8]. It is the quantum repeater (QR), and is based on entanglement and quantum memories. It will be presented in section 1.3.

1.1.3 Entanglement

Entanglement is a purely quantum phenomenon playing a crucial role in quantum information science, and is a useful resource for several applications like QKD or Bell inequalities violation. Two systems are entangled if the joint quantum state describing them cannot be factorized. In an entangled state, this joint quantum state is well defined, but each subsystem is in a mixed state, i.e. it does not have well defined properties before being measured. For example, the state of two photons A and B entangled in polarization in the $\{|H\rangle ; |V\rangle\}$ basis can be written as

$$|\psi_{AB}\rangle = \frac{1}{\sqrt{2}} \left(|H_A\rangle |H_B\rangle + e^{i\phi} |V_A\rangle |V_B\rangle \right). \tag{1.2}$$

This corresponds to a maximally entangled state, where the individual states of A and B are correlated with certainty. In this example, the photons don't have a specific polarization, but the measurement of one of them projects its state to a given polarization and ensures that the other has the same polarization. Entanglement leads to very strong correlations between the measurement outcomes on the two systems, which cannot be explained classically. The distribution of entangled states over long distance is the subject of intense research. Ideally, the entanglement quality between two systems is independent on the distance separating them at the time of the measurement, which explains the interest of entanglement distribution over long distances. In practice however, losses and decoherence limit the possible distance as for the case of qubits transmission. Nevertheless, entanglement can be extended over large distances using a procedure called entanglement swapping, which is based on Bell states measurements.

1.1.3.1 Bell states

Bell states are maximally entangled states of two qubits. There are four of them:

$$\begin{aligned} \left|\phi^{\pm}\right\rangle =& \frac{1}{\sqrt{2}} \left(\left|0_A\right\rangle \left|0_B\right\rangle \pm \left|1_A\right\rangle \left|1_B\right\rangle\right) \\ \left|\psi^{\pm}\right\rangle =& \frac{1}{\sqrt{2}} \left(\left|0_A\right\rangle \left|1_B\right\rangle \pm \left|1_A\right\rangle \left|0_B\right\rangle\right). \end{aligned} \tag{1.3}$$

These states have the particularity to violate the Bell CHSH inequality [9] with the maximal possible value of $2\sqrt{2}$. These inequalities express bounds on the statistics of spatially separated measurements in local hidden variable theories. This means that they can only be violated by non-classical systems, like entangled photon pairs for example.

1.1.3.2 Bell states measurements

A Bell state measurement (BSM) is a joint measurement on two qubits. Since the Bell states constitute and orthonormal basis for any two-qubit state, the result of such a measurement is one of the four Bell states, which are entangled states. Therefore, a BSM is an entangling operation, even if the two qubits were not entangled prior to the measurement. BSMs can be performed in a linear or non-linear way. The linear approach has the advantage to be implementable only with beam-splitters or polarizing beam-splitters, phase shifters such as wave plates and single photon detectors. However, it is impossible to fully distinguish between the four Bell states with this approach, the maximal efficiency being 50% [10]. The non-linear approach allows us to fully distinguish between each Bell state, but requires strong interactions between the qubits. BSMs are a central element in the quantum teleportation and entanglement swapping protocols.

1.1.4 Quantum teleportation

Quantum teleportation allows us to transfer an arbitrary quantum state (as the state of an unknown qubit for example) between two remote parties A and B [11]. The transfer happens instantaneously, and the initial state

is lost in the process. The support for this protocol is an entangled system shared between the two parties, and classical communication is also required. For clarity of explanation, I will consider qubits encoded on single photons.

Let us consider the state to be teleported to be the one of eq. (1.1). Let us also consider that the shared entangled photon pair is prepared in the $|\phi^-\rangle$ Bell state. The state describing the three photons is then

$$|\psi_{XAB}\rangle = \frac{\alpha}{\sqrt{2}}\left(|0_X 0_A 0_B\rangle - |0_X 1_A 1_B\rangle\right) + \frac{\beta}{\sqrt{2}}\left(|1_X 0_A 0_B\rangle - |1_X 1_A 1_B\rangle\right), \tag{1.4}$$

which can be rewritten in the Bell states basis for X and A as

$$\begin{aligned} |\psi_{XAB}\rangle = \frac{1}{2}\Big\{ & \left|\phi^+_{XA}\right\rangle\left(\alpha\,|0_B\rangle - \beta\,|1_B\rangle\right) \quad + \\ & \left|\phi^-_{XA}\right\rangle\left(\alpha\,|0_B\rangle + \beta\,|1_B\rangle\right) \quad + \\ & \left|\psi^+_{XA}\right\rangle\left(-\alpha\,|1_B\rangle + \beta\,|0_B\rangle\right) \quad + \\ & \left|\psi^-_{XA}\right\rangle\left(-\alpha\,|1_B\rangle - \beta\,|0_B\rangle\right) \quad \Big\}. \end{aligned} \tag{1.5}$$

A BSM is performed at location A between the qubit to be teleported and the qubit of the shared entangled pair placed at this location. The result of this measurement is one of the four Bell states, and is communicated classically to location B. After this, depending on the outcome of the measurement, a unitary transform is applied on the state of the photon in B in order to get an identical qubit as the original one.

1.1.5 Entanglement swapping

Entanglement swapping [12] is a special case of quantum teleportation where the teleported state itself is entangled. It allows one to entangle two systems which did not previously interact, and by doing so plays a key role in enabling entanglement distribution over larger distance than the limit set by losses in the communication channels. An example of entanglement

swapping between entangled photons pairs with linear optics Bell state measurements is represented in Fig. 1.1.

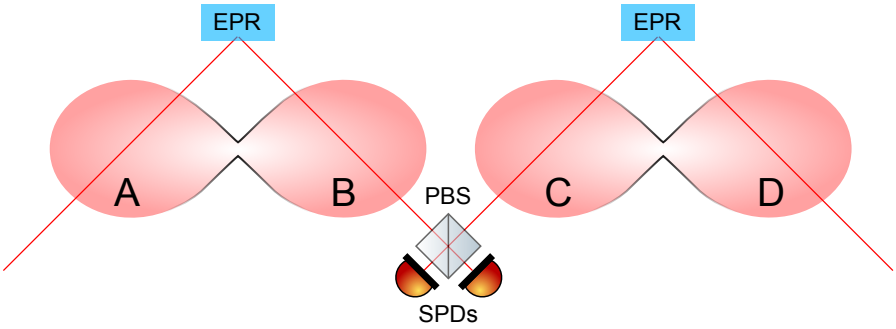

FIGURE 1.1: **Entanglement swapping using linear optics Bell state measurements.** EPR: entangled photon pair source. PBS: polarizing beam-splitter. SPDs: single photon detectors.

Two entangled photon pair sources produce pairs in a given Bell state. A polarizing beam-splitter (PBS) reflects vertically-polarized photons, and transmits horizontally-polarized ones. In this way, when a coincident detection happens, it means that photons B and C had similar polarizations. Since it is known from the entangled state that A and B, as well as C and D have similar polarizations, it comes that now A and D have the same polarization. However, which polarization is it is still unknown, so they are projected onto the same entangled state. For a more detailed explanation, see section 2.1.

1.2 Quantum memories

As in classical information, one needs to be able to store qubits. In this aspect, a major difference arises, which can be understood from the no-cloning theorem. It is generally impossible to read the state of a qubit, store it in a standard memory, retrieve it at a later time and copy it to a new qubit. This is why quantum memories are developed. A quantum memory allows the direct transfer of a quantum state to the memory without reading it. Usually, the information carried by the incoming flying

qubit, which is encoded on light in many cases, is transferred to internal degrees of freedom of the atoms composing the QM. In this section, I will only discuss optical quantum memories [13, 14].

1.2.1 General types of quantum memories

In general, we can distinguish between the absorptive and emissive types of QMs.

Absorptive quantum memories

In absorptive QMs, an input signal emitted from a separate source is stored in the memory before being retrieved. This signal can either be a single photon state, or a general state such as squeezed states, coherent states, or Fock states for example. During the readout, the detection of single photons can be performed via photon counting techniques or homodyne detection, while only the latter is used for general states. In the photon counting case, one can separate the retrieval efficiency from the conditional fidelity, which is the fidelity conditioned on a photon having been emitted by the memory (see section 1.2.2). In the homodyne detection case, the efficiency is part of the fidelity.

Emissive quantum memories

In emissive QMs, such as the Duan-Lukin-Cirac-Zoller (DLCZ, [15]) type, classical pulse are used to create non-classical correlations or entanglement between an emitted photon and an internal degree of freedom of the atomic system. This degree of freedom can be for example the spin of a single atom, or a spin excitation in the case of an atomic ensemble. This excitation can then be retrieved by mapping it on a second single photon. The characterization of the memory performance can be done using SPDs or homodyne detection [16], as for absorptive QMs for single photons.

1.2.2 Figures of merit for quantum memories

There are several figures of merit to characterize the performances of QMs. As a general rule, it is desirable to have efficient writing and reading processes, without any modification of the quantum state by the storage process. Then, depending on the application of the QM, long storage time, on-demand readout, and temporal or spatial multimode capability can be useful. The possibility to easily connect a quantum memory to the telecom network can also be an advantage.

Fidelity of the storage

The fidelity of the storage is a measure of the modification of the quantum state by this process. It is defined as the overlap between the single-photon wave packet which was sent in the QM and the one that is retrieved. In photon counting experiments, the conditional fidelity is used, which is the fidelity conditioned on a photon having been emitted by the memory. For an input state $|\psi_{in}\rangle$, the conditional fidelity is

$$F = \langle \psi_{in} | \rho_{out} | \psi_{in} \rangle \,, \tag{1.6}$$

with ρ_{out} the reduced density matrix of the output state. Quantum state tomography is usually used for this type of characterization.

Storage and retrieval efficiencies

The storage efficiency is not defined for emissive QMs. For absorptive QMs, it corresponds to the probability that the input signal is absorbed by the memory. The retrieval efficiency is then the probability to re-emit a photon once the memory is read-out. For absorptive QMs, The storage and retrieval efficiency is the product of the storage efficiency and of the retrieval efficiency.

Storage time

The atomic levels used for storage of a quantum state should be long lived, with particular requirements for the lifetime depending on applications. For example, for a memory used in a long-distance communication protocol such as a QR, the memory lifetime should be longer than the total time to distribute an entangled pair over the communication channel, which is dependent on the channel length and the number of QR nodes in the chain.

Multimode capability

Multimode storage can only be implemented in systems formed by an ensemble of particles, like atomic ensembles or doped crystals. It can be temporal [17–19], spatial [20] or spectral [21]. The multimode capability is useful for applications where repetition rates are a limitation, in particular for QRs. For temporal multiplexing, the number of modes that can be stored is characterized by the time-bandwidth product. It is the product of the storage time, measured as the $1/e$ Gaussian decay time for example, with the memory bandwidth. However, as will be shown below, not all protocols enable temporal multiplexing. The spatial multimode capability also allows to store images and generate quantum holograms [22].

Memory bandwidth

The memory bandwidth corresponds to the bandwidth of the input light which can be stored in a QM. A larger bandwidth allows the storage of shorter photons and hence a higher repetition rate. It is also an important parameter to consider when connecting different types of quantum memories together, for quantum networks for example.

Connection to telecom wavelength

The different types of quantum memories can store and emit photons at specific wavelengths, given by the atomic species used to implement them. The wavelength range for which the transmission losses are the lowest is the telecom c-band. However, most physical systems used for quantum

memories are not compatible with it, except the one based on erbium atoms [23, 24]. Several techniques have been proposed to couple quantum memories to the telecom C-band, including using quantum frequency conversion [25, 26] which will be studied in this thesis.

1.2.3 State of the art of quantum memories

I will now present a state of the art on the work which has been done on quantum memories. Many different systems can serve as the physical support of the quantum memories, which can then be implemented with various protocols. I will first introduce the different systems which can be used as physical support, before presenting the different protocols.

1.2.3.1 Systems to implement quantum memories

There are two families of systems to implement quantum memories for light. The first one is single-particle systems, which includes single atoms or ions in optical cavities, and vacancy centers in diamond. They often need to be placed in optical cavities to enable the strong light-matter interaction necessary to reach high efficiencies. The second family is atomic ensembles, which allow strong light-matter interaction without the need of cavities, provided that the optical depth is high enough. In these systems, quantum information is usually stored as a collective excitation, which is delocalized and involves all the atoms addressed by the probing beams. Moreover, they can have larger bandwidths and offer the possibility to introduce multiplexing of quantum information. Atomic ensembles are divided into solid-state systems with rare-earth ions doped crystals, and warm or cold atomic vapors.

Single atoms or ions

Due to a weak light-matter interaction at the single-atom level, single atoms or ions need to be placed inside a high finesse cavity to reach the

strong coupling regime [27], and then be able to be an efficient interface to store and retrieve photonic qubits. Initial experiments showing strong coupling between a single atom and a single photon have been realized in 1992 [28], and reversible mapping of a coherent state of light with mean photon number close to unity to and from the hyperfine states of an atom in a high-finesse cavity has been demonstrated in 2007 [29]. An experimental realization has been done in 2007 [30], where a single atom is entangled with a single photon, before mapping of the atomic state onto a second single photon. A quantum memory for polarization qubits has then been realized with this system [31], achieving a fidelity of 93% after $2\mu s$ storage, a total efficiency of 9% and a coherence time over $180\mu s$. An elementary quantum network of two single atoms in separate optical cavities [32], and heralded entanglement between two single atoms in separate cavities [33], have been demonstrated in 2012. Recently, an experiment demonstrating a heralded quantum memory has been demonstrated with a single atom in a cavity [34]. Entanglement of two fixed single-atom quantum memories using single ions have been demonstrated in 2007 [35]. Heralded absorption of a single photon by a single ion has been shown in 2009 [36].

Vacancy centers in diamond

These type of systems can show coherence times of the order of a second [37]. Entanglement between a photon and a solid-state spin qubit in a NV center has been shown [37]. Two-photon quantum interference from remote nitrogen-vacancy (NV) centers in diamond [38, 39] has been shown, before heralded entanglement between two separate NV centers [40]. More recently, unconditional quantum teleportation between two NV centers has been demonstrated [41].

Rare-earth ions doped crystals

This support is broadly studied. It offers the advantage that the active ions used for storage do not move, since they are integrated in the crystalline structure. This allows one to achieve long optical and hyperfine

coherence times at cryogenic temperatures [42]. However, the large inhomogeneous broadening of the optical transitions, due to the fact that each ion sees a slightly different crystal environment, induces a dephasing of the atomic dipoles once light is stored. Photon-echo protocols leading to their rephasing, in combination with spin-state storage, can be used to achieve efficient storage with long storage times [43] (see Atomic Frequency Comb part in section 1.2.3.2).

Warm atomic vapors

Warm atomic vapors experiments are usually done in glass cells with dimensions varying from the cm to the μm range. The strong light-matter interaction can be achieved at room temperature or by heating to increase the optical depth. Because of the inhomogeneous broadening of the atomic transitions due to the Doppler effect, only off-resonant protocols are usually implemented, like Raman memories for example. Storage based on electromagnetically induced transparency (EIT) has also been implemented. However, a high signal-to-noise ratio (SNR) at the single photon level has not been achieved so far [44, 45].

Cold atomic ensembles

Obtaining a cloud of cold neutral atoms allows strong light-matter interactions at the single photon level due to the possibility to reach high optical depth and implement various protocols [46]. It is often sufficient to work with cold atoms trapped in a magneto optical trap (MOT), without the need to go to the temperature and pressure range allowing to obtain a Bose Einstein condensate (BEC). Although a BEC offers much higher densities, potentially leading to increased retrieval efficiencies, a standard MOT offers the advantages of a simplified experimental setup and higher repetition rates, which is important in the frame of quantum information with single photons.

1.2.3.2 Different protocols for quantum memories

In this section I will present the different protocols used to implement QMs on atomic ensembles.

Electromagnetically induced transparency

Electromagnetically induced transparency [46–48] is based on a Λ- or ladder-type 3-level energetic structure. An input probe light is sent on resonance with one of the transitions, together with a strong control light resonant with the second transition. In the presence of the control beam, the medium becomes transparent to the probe light due to quantum interference of the two dressed states created by the control light [49, 50], canceling the imaginary part of the susceptibility. Moreover, the control light makes the medium strongly dispersive, which reduces the group velocity of the probe light. By appropriate timing, an input probe pulse can be compressed inside the medium and stopped for a variable storage time by adiabatic switching off of the control light. Subsequent retrieval is then possible by switching it on again.

Single photon storage in a cold atomic ensemble using EIT has been demonstrated for the first time in 2005 [51], followed by various experiments in the quantum or classical light regime [52–60]. The maximum efficiency measured so far is 78% with classical light [56], and 49% with single photons [55]. Squeezed light storage in cold atoms using EIT has also been realized since 2008 [61, 62].

Raman

Raman memories are based on Raman scattering, first observed in 1928 [63]. It is a two-photon process taking place in Λ-type systems. A detuned pump photon is absorbed, while a Stokes or anti-Stokes photon is emitted, fulfilling the two-photons resonance condition. In Raman QMs however, a signal photon is absorbed, and a strong control field on the other transition stimulates the emission of a photon on this transition. In this case,

a single undetermined atom is transferred to the state addressed by the control beam, creating a collective atomic excitation delocalized in the ensemble, also called a spin-wave. This type of protocol allows the storage of very short (and broadband) photons due to the possibility to have a large single-photon detuning. It has been proposed in 2007 [21], and the first implementations started in 2010 [64–66].

Controlled reversible inhomogeneous broadening

The controlled reversible inhomogeneous broadening (CRIB) protocol [43] is based on photon-echo [67, 68]. It relies on the application of an external inhomogeneous broadening to the atomic transitions of the atoms. This broadening is spatially varying, leading to different resonance frequencies for each atom, and must be reversible in a short timescale. It was first proposed for Doppler broadened atomic vapors in 2001 [69], before being adapted for rare-earth doped crystals in 2005 and 2006 [70, 71].

In solid state systems, a narrow absorption line is created within the naturally inhomogeneously broadened optical transition. This line is then broadened by the application of a controlled external electric field, which reduces the OD and limits the efficiency. When input light is absorbed, the atomic dipoles start to dephase, and rephasing is possible by reversal of the controlled broadening, triggering the re-emission of the stored light at a controllable time. Several experiments were realized with classical light pulses [72, 73], and then at the single photon level [23, 74]. Ref [74] demonstrated the largest storage and retrieval efficiency achieved in a solid state optical quantum memory so far (69%). When the broadening is applied along the propagation direction (longitudinal broadening), the protocol has been called Gradient Echo Memory (GEM).

Λ-gradient echo memory

The Λ-GEM protocol [75] is similar to the CRIB, since it also relies on a controlled and reversible inhomogeneous broadening. It is based on the

Raman protocol, with an inhomogeneous broadening applied while the input light is absorbed, inducing a dephasing of the created spin-wave. The broadening is then reversed, leading to a rephasing of the spin-wave. The stored excitation can then be retrieved onto a photonic field if the readout is performed at the rephasing time. Experiments with classical light and at the single photon level have been performed [73, 76–80]. Λ-GEM has demonstrated the most efficient absorptive quantum memory to date [77] with an efficiency of 89% for bright pulses.

Atomic frequency comb

The atomic frequency comb (AFC) protocol is used in solid-states systems and inspired by the CRIB. Here, the naturally inhomogeneously broadened optical transition is modified to obtain periodically separated absorption lines. This discrete, comb-like spectral structure allows periodic dephasing and rephasing cycles of the atomic dipoles, leading to spontaneous re-emission of stored light at a time set by the parameters of the comb structure. On-demand read-out is possible by transfer of the population from the excited state to a second ground state. This protocol was proposed in 2009 [17]. Several experiments with classical and single photon light storage in the excited state have been performed [81–89]. Time-bin qubits storage have been demonstrated [90, 91]. Heralded entanglement of two separate crystals has been shown [92]. Photonic polarization qubits storage has been realized [93–95]. The multimode capability of this protocol has been shown, temporally [96] and spectrally [97]. All the experiments mentioned previously were done with storage in the excited state, leading to short and pre-determined storage times. Spin-wave storage has also been demonstrated in the classical regime [94, 98–100] and very recently in the quantum regime [101, 102].

Faraday interaction

Faraday interaction is used in the continuous variable regime. Here, the variables are the quadratures of the electric field of the light, and of the

atomic spins. Light is interacting with the atoms, producing an entangled state and rotating the light's polarization. This rotation is measured and the result is fed back to the atoms, effectively mapping the quantum state of the light onto the atoms [14]. This method has been used to implement the first quantum memory [103]. Since then, other quantum memory and quantum teleportation experiments have been performed [104–106].

DLCZ

The DLCZ protocol is named after the authors of its proposal, Duan, Lukin, Cirac and Zoller [15, 107]. It is an emissive-type of QM, originally thought to be the building block for QRs. In this protocol is usually implemented in cold atomic ensembles, where the relevant energy levels structure are in a Λ-configuration, with all the atoms initially prepared in one of the ground states. A weak write pulse is off-resonantly applied on the populated transition, probabilistically creating a single write photon in the detection mode via Raman scattering. The detection of this photon heralds the creation of a correlated spin-wave, defined as for the Raman memory protocol. The spin-wave can then be read-out after a programmable delay by means of a read pulse resonant with the second transition, mapping it onto a single read photon emitted in a well-defined spatio-temporal mode. The write and read photons usually show correlations with a high degree of non-classicality, and have the possibility to be entangled in polarization or time-bin. This type of QM is conceptually similar to an entangled photons pairs source combined with an absorptive QM with on-demand readout allowing to delay one of the photons. It is highly relevant for protocols where synchronization between probabilistic events is necessary, such as entanglement swapping chains used for QRs. This protocol is appealing because it combines a photon pair source and a quantum memory in one physical system, and can therefore also be used as an heralded single photon source.

The first experimental observation of non-classical correlations have been performed in 2003 [108, 109], and the first functional quantum repeaters

segments have been demonstrated in 2007 [110] and 2008 [111]. The DLCZ protocol has been used to entangle two remote atomic ensembles in 2005 [112], and four in 2010 [113]. Experiments showing synchronized single photon pairs source generated from two DLCZ QMs have been performed [114, 115]. High retrieval efficiencies (up to 84%) [16, 116, 117] and long storage times (up to 165 ms) [25, 118, 119] have been shown with this protocol. Both characteristics have been combined in one setup with a retrieval efficiency of 30% and a storage time of 3.2 ms [120]. Connection of DLCZ QMs to telecom wavelength has been realized with four-wave mixing in an atomic ensemble [25], and in this thesis by difference frequency generation (DFG) in a waveguide [26, 121]. Finally, the retrieved single photons have been characterized with homodyne tomography [16]. A combination of CRIB and DLCZ protocol has also been demonstrated in the context of this thesis, where a magnetic field gradient broadens the atomic ground states [19].

1.3 Quantum repeaters based on the DLCZ protocol

Quantum repeaters have originally been proposed in 1998 by Briegel *et. al.* [8]. With the proposed model, the required time for entanglement distribution scales polynomially with the distance instead of exponentially in the case of direct transmission. A communication channel connecting two locations A and B is split into several shorter segments connected by nodes. Each segment comprises an entangled photon pair (EPR) source [11], and the entanglement is propagated between neighboring segments by entanglement swapping, until one high fidelity EPR pair is shared between locations A and B. This is represented in Fig. 1.2. Two important features are necessary due to the probabilistic nature of the creation of EPR pairs. First, QMs must be placed in each arm, in order to store entanglement in each

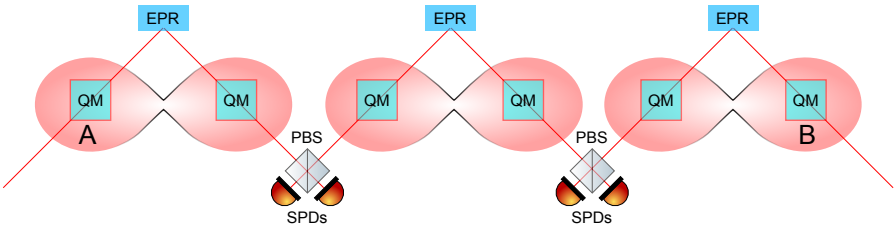

FIGURE 1.2: **Quantum repeater.** EPR: entangled photon pair source. PBS: polarizing beam-splitter. SPDs: single photon detectors. QM: quantum memory.

segment until global success, before being able to proceed with the swapping operations. Second, the entanglement has to be heralded. The DLCZ protocol [15] proposes to replace the EPR sources and QMs with atomic ensembles playing both roles. Several other schemes inspired by this protocol have been proposed since [122, 123]. The performances of several QRs protocols based on atomic ensembles and linear optics are reviewed in [124]. Elementary nodes and links of a DLCZ QR have been realized experimentally [110–112, 115, 125].

Other quantum repeater protocols have been proposed using different physical systems, for example single ions [126], single atoms in cavities [127], and Rydberg atoms [128, 129]. Recently, another type of quantum repeater based on quantum error correction has also been proposed [130–132]. This type of repeaters can potentially achieve much higher bit rate, but are much more demanding in terms of resources.

1.4 Quantum frequency conversion

Frequency conversion via non-linear interactions in dielectric media is a well-understood and developed field. However, it was not straightforward that quantum properties of an input field could be conserved and transferred to the converted field, due to strong noise suppression requirements. Quantum frequency conversion (QFC) allows to shift the carrier frequency of quantum light while preserving its quantum characteristics. Commonly

used processes include sum frequency generation (SFG), difference frequency generation (DFG), and four-wave mixing. It was proposed by Kumar in 1990 [133], and experimentally demonstrated with SFG shortly afterwards [134]. Many QFC experiments have been realized [135–139]. It has been shown that QFC preserves time-bin [140, 141] and polarization entanglement [142]. Conservation of anti-bunching for single photons emitted from a quantum dot [143], temporal shaping by modulation of the pump power [144], phase coherence preservation of a quantum state [145] and photon statistics preservation [146] have been demonstrated. So far, only two experiments have demonstrated QFC compatible with quantum memories [25, 26]. In this thesis, we showed the preservation of non-classical correlations between photons emitted from a DLCZ QM, after conversion of the read photons [26]. For a more detailed study of QFC, refer to [147].

1.5 Content of the Thesis

During my PhD, I worked towards improving the performances of future DLCZ-based quantum repeaters. I will present the results of our efforts towards the realization of a temporally multiplexed DLCZ quantum repeater node for long-distance quantum communication using a cold ^{87}Rb atomic ensemble. This includes the ability to connect our system to the telecom network via quantum frequency conversion from 780 nm to 1552 nm, and the study of controlled rephasing of single spin excitation with selective readout.

In chapter 2, I present more in details the DLCZ protocol, as well as the figures of merit and sources of dephasing of DLCZ quantum memories. I also detail the quantum frequency conversion process.

Chapter 3 describes our experimental setup used to implement the different DLCZ-type experiments. Since I joined the group during its first months, the design and building of the experimental setup from scratch was an important part of my PhD work.

In chapter 4, I explain how we implemented the DLCZ protocol and show a characterization of our DLCZ quantum memory.

Chapter 5 deals with our experimental results on quantum frequency conversion of weak coherent light compatible with atomic quantum memories, and of single photons created with the DLCZ quantum memory.

In chapter 6 I present our experimental results towards the implementation of temporal multiplexing in the DLCZ protocol.

Finally, chapter 7 will be the conclusion to my thesis.

Chapter 2

Theory of the DLCZ protocol and quantum frequency conversion

In this chapter, I will explain more in details the DLCZ protocol, and its underlying theory. I will also explain the DFG process used in our quantum frequency conversion experiment.

2.1 The DLCZ protocol

The DLCZ protocol is the basis of many QR protocols aiming at distributing entangled photon pairs between remote locations over large distances. To implement DLCZ-type QRs, one needs emissive-type QMs based on atomic ensembles capable of on demand-readout and of producing heralded entanglement. Such QMs can be viewed as a combination of an entangled photon pairs source and an absorptive QM. They also have to be connected by entanglement swapping.

In the following, I will explain the underlying processes behind the DLCZ protocol, starting by the states describing the collective atomic excitation, and the atoms-photon system. The theory described here is taken from [15].

2.1.1 Building block: the DLCZ Quantum Memory

Let us consider an optically thick cloud of N identical neutral atoms. The relevant energy levels structure consists of three levels in a Λ-type configuration, as shown in Fig. 2.1. The $|g\rangle$ and $|s\rangle$ states must be long lived, and can be two hyperfine levels of a metastable electronic ground state, while $|e\rangle$ can be one of an excited state. In practice, this structure is easily obtained in alkali metals for example.

Initially, all atoms are prepared in the $|g\rangle$ state. A weak, off-resonant short pulse (typically from ten to several hundreds of nanoseconds) is sent on the cloud, transferring atoms to the $|s\rangle$ state via Raman scattering. Such scattering events, called write photons, are correlated with the excitation

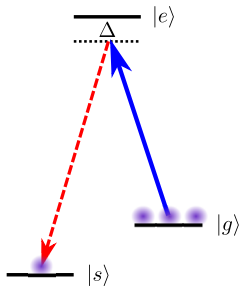

FIGURE 2.1: **Λ-type energy levels structure.** $|g\rangle$, $|e\rangle$, and $|s\rangle$ denote the initial ground state, the excited state, and the so-called storage state. Solid arrow: write pulse. Dashed arrow: write photon

of the symmetric collective atomic mode described by the operator

$$S = \frac{1}{\sqrt{N}} \sum_{j=1}^{N} e^{-i(\mathbf{k}_W - \mathbf{k}_w)\cdot \mathbf{r}_j} \left|g\right\rangle_j \left\langle s\right|, \tag{2.1}$$

where $\mathbf{r}_j$ is the position of atom j, and $\mathbf{k}_W$ and $\mathbf{k}_w$ are the wave vectors of the write pulse and write photon respectively. The write photons emission is isotropic, but they are collected and detected in one single spatial mode only, so the atomic excitations associated with photons emitted outside of the detection mode can be neglected. Defining the ground state of the ensemble as $|0_a\rangle = \otimes_j |g_j\rangle$, the state of the atomic ensemble directly after the detection of a single write photon is

$$|\psi(0)\rangle = S^\dagger |0\rangle_a = \frac{1}{\sqrt{N}} \sum_{j=1}^{N} e^{i(\mathbf{k}_W - \mathbf{k}_w)\cdot \mathbf{r}_j} |g_1 \cdots s_j \cdots g_N\rangle, \tag{2.2}$$

Note that the phase term simplifies in the case of forward detection with respect to the write pulse. However in practice a small angle (typically of the order of one degree) is introduced between the write pulse and write photon detection modes. This is to facilitate the filtering of the single write photons from the much higher photon number of the write pulse. The spin-wave temporal dephasing due to atomic motion increases with this angle, as described in more details in section 2.1.4. This state corresponds to a single collective atomic spin excitation, also called spin-wave.

The state describing the atom-light system is a two-mode squeezed state, which can be written as

$$|\phi\rangle = \sqrt{1-p}\sum_{n=0}^{\infty} p^{n/2}(S^\dagger a^\dagger)^n |0\rangle_a |0\rangle_p \,, \tag{2.3}$$

where p is the probability to create at least one write photon per trial in the detection mode, $a^\dagger$ is the write photon creation operator, and $|0_p\rangle$ is the vacuum state. From this equation, we see that the probability for creating multiple spin-waves and write photons in the same mode is non negligible if p becomes too high. This is detrimental for the fidelity of the generated entanglement, so low values of p are used in practice (typically below 10%, ideally below 1%). Conditioned on the detection of a write photon, the spin-wave can be efficiently read out and mapped onto a single read photon. The read photon is emitted into a well defined spatio-temporal mode. The temporal mode is given by the read pulse temporal shape, while the spatial mode is given by the phase-matching condition $\mathbf{k}_r = \mathbf{k}_W + \mathbf{k}_R - \mathbf{k}_w$, with $\mathbf{k}_R$ and $\mathbf{k}_r$ the wave vectors of the read pulse and read photon respectively.
The creation of such states is the basis for entanglement generation between to separate DLCZ QMs.

2.1.2 Entanglement generation

The setup for entanglement generation between two nodes is shown in Fig. 2.2.

Two atomic ensembles placed at nodes A and B are simultaneously excited by write pulses. The system consisting of both ensembles and the associated write photons and spin-waves is described by the state $|\phi\rangle_A \otimes |\phi\rangle_B$, with $|\phi\rangle_{A,B}$ given by eq. (2.3). For each trial, there are four different possibilities. First, no photon is emitted or detected, in which case the trials continue. Second, either one of the two detectors records a photon arrival. This can be separated into two cases which are indistinguishable. Most of

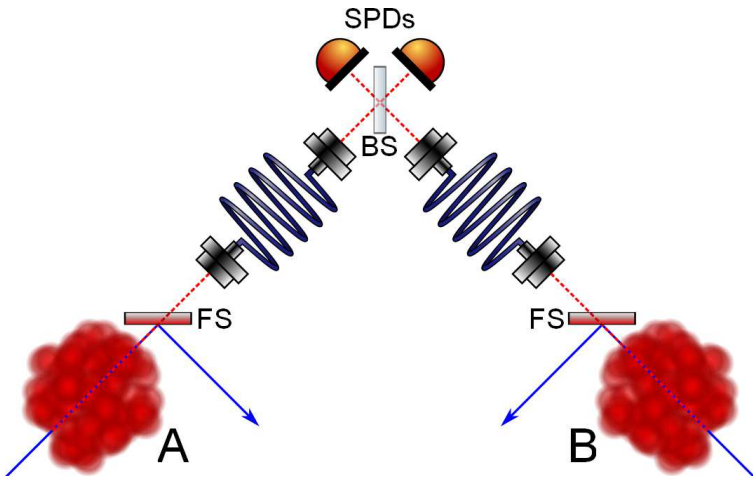

FIGURE 2.2: **Entanglement generation between two nodes A and B.** BS: beam-splitter. FS: Filtering stage. SPDs: single photon detectors. Solid arrow: write pulses. Dashed line: write photons.

the times, one single write photon has been emitted from either of the two ensembles, which happens with a probability p. It can also happen that both ensembles simultaneously emit a write photon, in which case either both photons reach the same detector or one can be lost, leading to an error due to the impossibility to discriminate these events. These events happen with a probability p^2 and are also detrimental to the entanglement fidelity, again demonstrating the necessity of having low values of p. Finally, simultaneous detection events can happen with the same probability, and are simply discarded. In the following, we will focus on the case where only one ensemble emitted a single photon, i.e. $p \ll 1$.

In this case, the detectors measure the combined radiations from the two ensembles, which are $a_+^\dagger a_+$ or $a_-^\dagger a_-$, with $a_\pm = (a_A \pm e^{i\varphi} a_B)/\sqrt{2}$, depending on which detector makes the measurement. Here, φ accounts for a phase difference between the two channels. Conditioned on a detection

event, the state of the system is projected onto the nearly maximally entangled state (to first order in p)

$$\begin{aligned} |\Psi\rangle_{AB}^{\pm} =& \frac{S_A^\dagger \pm e^{i\varphi_{AB}} S_B^\dagger}{\sqrt{2}} |0\rangle_{a,A} |0\rangle_{a,B} \\ =& \frac{1}{\sqrt{2}} \left(|1\rangle_{a,A} |0\rangle_{a,B} \pm e^{i\varphi_{AB}} |0\rangle_{a,A} |1\rangle_{a,B} \right), \end{aligned} \tag{2.4}$$

where $|1_a\rangle_{A,B}$ symbolizes a single atomic excitation in the ensemble A (resp. B), and is equivalent to the state of eq. (2.2). This is an ideal state valid only in the absence of noise sources. To take noise into account (originating from detectors dark counts, classical laser pulses or ambient light), the state of eq. (2.4) becomes

$$\rho_{AB}(c_0) = \frac{1}{1+c_0} \left(c_0 |0_a 0_a\rangle_{AB} \langle 0_a 0_a| + |\Psi\rangle_{AB}^{\pm} \langle \Psi| \right), \tag{2.5}$$

where c_0 is a weight coefficient for the vacuum component and depends on the noise sources.

The entanglement generation rate is

$$R_{gen} \propto \frac{p \cdot \eta_t \cdot \eta_d}{t_{trans}}, \tag{2.6}$$

where $t_{trans} = l_{trans}/c$ is the transmission time through a channel of length l_{trans}, η_t is the transmission efficiency from the ensemble to the detector (including collection, filtering and transmission channel), and η_d is the detection efficiency. Due to the heralded nature of the entanglement, one needs to wait between each trial to verify if entanglement was successfully generated, hence the term t_{trans}. Photon losses limit the achievable entanglement generation rate. They arise due to finite collection efficiency, absorption in the filtering and transmission channels, and limited detector efficiencies. However, they do not affect the fidelity of the generated entangled state. The next step of this protocol is to perform entanglement connection operations once entanglement has been successfully generated in two adjacent segments.

2.1.3 Entanglement connection

The setup for entanglement swapping is shown in Fig. 2.3.

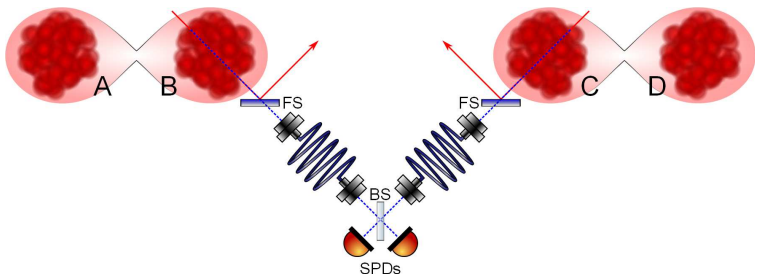

FIGURE 2.3: **Entanglement swapping.** BS: beam-splitter. FS: Filtering stage. SPDs: single photon detectors. Solid arrow: read pulses. Dashed line: read photons.

Here, the ensembles A and B, as well C and D, are entangled together as explained previously. The ensembles B and C are simultaneously excited by read pulses. The system consisting of the two pairs of entangled ensembles is described by the state $\rho_{AB}(c_0) \otimes \rho_{CD}(c_0)$, with $\rho_{AB,CD}(c_0)$ given by eq. (2.5). The detectors now measure the quantities corresponding to the operators $S_+^\dagger S_+$ or $S_-^\dagger S_-$, with $S_\pm = (S_B \pm S_C)/\sqrt{2}$. A successful detection will project the state onto

$$\rho_{AD}(c_1) = \frac{1}{1+c_1}\left(c_1 \left|0_a 0_a\right\rangle_{AD} \left\langle 0_a 0_a\right| + \left|\Psi\right\rangle_{AD}^{\pm} \left\langle\Psi\right|\right), \tag{2.7}$$

similar to the one of eq. (2.5) but with a different weight coefficient. The probability of success for this operation depends on c_1. In addition, the phase term of the maximally entangled term $|\Psi\rangle_{AD}^{\pm}$ is $\varphi_{AD} = \varphi_{AB} + \varphi_{CD}$.

For a more detailed explanation on how the different states shown previously are derived from the interaction Hamiltonian between light and atoms, see supplementary material of [15].

I will now explain the different dephasing mechanisms limiting the memory lifetime.

2.1.4 The dephasing mechanisms

The spin-wave created by the writing process experiences dephasing over time due to several decoherence mechanism. This dephasing can be assessed by measuring the retrieval efficiency which is proportional to

$$\eta_{ret}(t) \propto |\langle\, \psi(0)|\psi(t)\rangle|^2\,, \tag{2.8}$$

where $|\psi(0)\rangle$ is given by eq. (2.2), and $|\psi(t)\rangle$ is this state at the readout time.

Atomic motion

First, the presence of an angle between the write-read pulses and photons arm introduces dephasing due to atomic motion in the probing direction [119]. This can be understood in an intuitive way by associating the wave-vector $\Delta k = |\mathbf{k}_W - \mathbf{k}_w|$ to the spin-wave. Assuming that $k_W \approx k_w = \frac{2\pi}{\lambda}$ and that the angle θ between the write/read pulses axis and the photons detection axis is small, we get $\Delta k = \frac{2\pi}{\lambda}\cos(\theta)$. Finally, we relate this wave-vector to the spin-wave's wavelength

$$\Lambda_{sw} = \frac{2\pi}{\Delta k} \approx \frac{\lambda}{\cos(\theta)}, \tag{2.9}$$

which is rapidly decreasing when the angle increases. Now the intuitive picture suggests that once the atoms moved from a distance greater than Λ_{sw}, the spin-wave cannot be retrieved anymore.

The intuitive view is confirmed by relating the retrieval efficiency with the temperature of the atoms. Considering only atomic motion, we have

$$|\psi(t)\rangle = \frac{1}{\sqrt{N}} \sum_{j=1}^{N} e^{i(\mathbf{x}_j + \mathbf{v}_j t)\cdot(\mathbf{k}_W - \mathbf{k}_w)}\, |g_1 \dots s_j \dots g_N\rangle\,, \tag{2.10}$$

hence

$$\eta_{ret}(t) \propto \left| \frac{1}{N} \sum_{j=1}^{N} e^{i\mathbf{v}_j \cdot (\mathbf{k}_W - \mathbf{k}_w)t} \right|^2 . \tag{2.11}$$

Considering a three dimensional Maxwell-Boltzmann distribution for the atomic velocities, the previous equation simplifies to

$$\eta_{ret}(t) \propto e^{-\frac{k_B T \Delta k^2 t^2}{m}} = e^{-\frac{t^2}{\tau^2}}, \tag{2.12}$$

where k_B is the Boltzmann constant, T the temperature of the atoms, m the atomic mass and $\Delta k = |\mathbf{k}_W - \mathbf{k}_w|$. This corresponds to a Gaussian temporal decay with a $1/e$ time constant $\tau = \sqrt{\frac{m}{k_B T \Delta k^2}}$. We see that for a given angle, an increase of T corresponds to a faster dephasing. This expression also allows to calculate an upper bound (since other dephasing mechanisms are not considered here) for the temperature from storage times measurements.

Inhomogeneous broadening

Second, inhomogeneous broadening of the atomic levels can induce a rapid dephasing. The main cause for inhomogeneous broadening are spurious magnetic field gradients, which can be constant (fields created by magnetic elements in the vicinity of the MOT for example) or transient (fields created by Eddy currents induced during the switching of the MOT coils).

Considering the influence of inhomogeneous broadening only, we have

$$|\psi(t)\rangle = \frac{1}{\sqrt{N}} \sum_{j=1}^{N} e^{i \int_0^t \Delta\omega_j(t')dt' + i\mathbf{x}_j \cdot (\mathbf{k}_W - \mathbf{k}_w)} |g_1 \dots s_j \dots g_N\rangle , \tag{2.13}$$

where $\Delta\omega_j(t) = \Delta E_j(t)/\hbar$ is the relative detuning of the state $|j\rangle = |g_1 \dots s_j \dots g_N\rangle$, with respect to the same state with no Zeeman splitting, such that

$$\Delta E_j(t) = \sum_{i=1}^{N} \delta E_i^g(t) - \delta E_j^g(t) + \delta E_j^s(t), \tag{2.14}$$

where $\delta E_j^{g/s}$ is the Zeeman splitting for the state $|g/s\rangle$ of atom i. Therefore,

$$\eta_{ret}(t) \propto \left| \frac{1}{N} \sum_{j=1}^{N} e^{i \int_0^t \Delta\omega_j(t')dt'} \right|^2 . \tag{2.15}$$

However, inhomogeneous broadening can also be used at our advantage if they are actively controlled. Indeed, the application of such broadenings followed by a change of the sign can lead to a rapid dephasing of the spin-wave followed by a rephasing at a chosen time, allowing an efficient readout. This is the technique which is employed in Chapter 6.

Zeeman levels splitting

Third, splitting of the atomic levels, for example Zeeman splitting due to the presence of homogeneous magnetic fields, can lead to periodic cycles of dephasing and rephasing. This can happen if several atomic transitions are involved in the writing process, leading to the creation of several classes of spin-waves with different relative energies. When the atomic levels are non-degenerate, interference between the various classes will occur.

In the presence of an homogeneous magnetic field B, the Zeeman sub-levels m_F are split by an amount

$$\Delta\omega(m_F) = \frac{\Delta E(m_F)}{\hbar} = \frac{\mu_B g_F m_F B}{\hbar}, \tag{2.16}$$

with μ_B the Bohr magneton, $\hbar$ the reduced Planck constant, and g_F the Landé g-factor. Hence, the relative detuning between the two states $|g\rangle$ and $|s\rangle$ defining a spin-wave with respect to the case with no field, or for clock transitions, is

$$\Delta\omega(m_{F,|g\rangle} \leftrightarrow m_{F,|s\rangle}) = \Delta\omega(m_{F,|g\rangle}) - \Delta_\omega(m_{F,|s\rangle}) = \frac{\mu_B |g_F| B}{\hbar} \sigma_{m_F}, \tag{2.17}$$

with $\sigma_{m_F} = m_{F,|g\rangle} + m_{F,|s\rangle} \in [-3,-2,...,2,3]$, since $g_{F,|g\rangle} = |g_F| = -g_{F,|s\rangle}$. Due to angular momentum conservation, the maximal difference in m_F between the ground and storage states defining a spin-wave is 2.

When a spin-wave is created, it is distributed between the different cases depending on the polarization of the write pulse and of the detected write photons. This leads to temporal fluctuation of the phase of the spin-wave. Since the energy differences are discrete and multiples of each-other, periodic dephasing and rephasing of the spin-waves is observed. In this case, we have

$$|\psi(t)\rangle = \frac{1}{\sqrt{N}} \sum_{\sigma_{m_F}=-3}^{3} \sum_{j=1}^{N_{\sigma_{m_F}}} e^{i\int_0^t \Delta\omega_{\sigma_{m_F}}(t')dt' + i\mathbf{x}_j\cdot(\mathbf{k}_W - \mathbf{k}_w)} |g_1 \cdots s_j \cdots g_N\rangle \,. \tag{2.18}$$

Here, $N_{\sigma_{m_F}}$ corresponds to the number of atoms involved in each case. Overlapping this state with the one at zero time written in eq. (2.2), we can derive the expression for the retrieval efficiency

$$\eta_{ret} \propto e^{-\frac{t^2}{\tau^2}} \left| \sum_{\sigma_{m_F}=-3}^{3} C_{\sigma_{m_F}} e^{i\frac{\mu_B |g_F| B}{\hbar}\sigma_{m_F} t} \right|^2 , \tag{2.19}$$

where τ is the $1/e$ decay time and $C_{\sigma_{m_F}}$ indicates the distribution of the spin-wave into the different cases.

Loss of atoms

Last, the atoms involved in the collective state will eventually leave the probe beams mode volume due to free fall and thermal motion. The timescale at which free fall effects can be observed is of the order of the millisecond. The time required for the atoms to drop of 150 μm, corresponding to the $1/e$ beam waist radius of our probe beams, is 5.5 ms. To quantify the effect of thermal motion, let us consider the root-mean-square speed of the atoms

$$v_{rms} = \sqrt{\frac{3k_B T}{m}}. \tag{2.20}$$

Considering a cloud temperature of 100 μK, this speed is $\sim 170\,\mu\text{m} \cdot \text{ms}^{-1}$ for ^{87}Rb atoms.

How to deal with these issues

Fortunately, each of the previous dephasing mechanism can be addressed individually and storage times on the millisecond time scale can be achieved [25, 118, 119]. The dephasing due to the detection angle can be minimized by using a collinear configuration. However, this in turn strongly increases the requirements on the frequency filtering capability in order to isolate the single photons from the classical pulses. This can be done by means of Fabry-Perot etalons with appropriate extinction ratio, and in the case of cold atoms, by means of warm atomic vapor cell with high OD and efficient optical pumping of the atoms to the desired state. Magnetic fields effects in general can be minimized by working with magnetic insensitive clock transitions. If such transitions cannot be used, other techniques allow to counter their effects. Spurious constant magnetic field gradients can be negated by the introduction of a mu-metal magnetic shielding around the MOT. Spurious transient fields can be reduced by using a non-metallic vacuum chamber, and acting on compensation coils for magnetic gradient. Homogeneous magnetic fields can be cancelled if no optical pumping in a specific Zeeman sub-level is required for the initial preparation of the atomic ensemble by means of compensation coils in the Helmholtz configuration. If such optical pumping is required, efficient initial pumping placing most of the atoms in the desired state followed by appropriate emptying of the other states ensures that only one spin-wave class will be created. Finally, to prevent atom loss on the millisecond time scale, the atomic cloud can be loaded in an optical dipole trap.

2.1.5 Figures of merit for DLCZ quantum memories

DLCZ-type QMs can be used either as heralded single photon sources, as QR nodes, or as light-matter entanglement sources. The performance of

such QMs are assessed by several measurable parameters.

Memory lifetime

The memory lifetime is defined as the duration after which the initial retrieval efficiency at zero delay is divided by a factor equal to e^{-1}. The delay is the time between the successful creation of a spin-wave and its readout. As explained previously, it is principally limited by the dephasing of the stored spin-waves due to various decoherence sources. Achieving a sufficient memory lifetime is of particular importance in the case of QR applications, since the QM must be able to retain the quantum state long enough so that entanglement has been successfully generated for all the elementary segments of the QR channel. Experiments with storage time in the millisecond and even 100 ms regime have been realized, using clock states and atoms trapped in an optical lattice [118, 119].

Retrieval efficiency

The retrieval efficiency is the proportion of retrieved single read photons per successful heralded spin-wave creation. It is maximal at zero delay, when decoherence mechanisms are still negligible. It principally depends on the optical depth of the atomic ensemble [148, 149], as well as the correct mode matching between the 4 beams. Ideally, efficiencies close to unity could be achievable with the DLCZ protocol. However, in practice it is limited by inhomogeneities of the write and read beams, imperfect mode matching, and limited optical depth. Efficiencies up to 50% have been achieved in free space [116], and up to 84% by placing a cavity around the atoms [16, 117, 120].

Write and read photons statistics

The statistics of the write and read photonic modes taken independently are those of thermal fields [150, 151]. This means that the second-order intensity auto-correlation functions $g^{(2)}_{w,w}$ and $g^{(2)}_{r,r}$ are higher than one, and

ideally equal to two. They are generally defined as

$$g^{(2)}_{f_1,f_2} = \frac{p_{f_1,f_2}}{p_{f_1} \cdot p_{f_2}} = \frac{\left\langle a^\dagger_{f_1} a^\dagger_{f_2} a_{f_2} a_{f_1} \right\rangle}{\left\langle a^\dagger_{f_1} a_{f_1} \right\rangle \cdot \left\langle a^\dagger_{f_2} a_{f_2} \right\rangle}, \tag{2.21}$$

where $f_i \in \{w_i; r_i\}$ denotes the write or read photonic modes after passing through a balanced beamsplitter, p_{f_i} (resp. p_{f_1,f_2}) is the probability to detect a single photon from the photonic mode f_i (resp. a coincidence), and $a^\dagger_{f_i}$ (resp. a_{f_i}) is the creation (resp. annihilation) operator for the photonic mode f_i.

The statistics of the read photons conditioned on the detection of a write photon is the one of a single photon, and therefore exhibits anti-bunching. This means that the value of the conditioned auto-correlation function, also called the anti-bunching parameter α, is lower than one, and tending towards zero for perfect single photons. The definition of α is [152]:

$$\alpha = \frac{p_{(r_1,r_2|w)}}{p_{(r1|w)} \cdot p_{(r2|w)}} = \frac{p_{w,r_1,r_2} \cdot p_w}{p_{w,r_1} \cdot p_{w,r_2}} = \frac{\left\langle a^\dagger_w a^\dagger_{r_1} a^\dagger_{r_2} a_{r_2} a_{r_1} a_w \right\rangle \cdot \left\langle a^\dagger_w a_w \right\rangle}{\left\langle a^\dagger_w a^\dagger_{r_1} a_{r_1} a_w \right\rangle \cdot \left\langle a^\dagger_w a^\dagger_{r_2} a_{r_2} a_w \right\rangle}. \tag{2.22}$$

It can be expressed as a function of the probability p to create one or more spin-wave as [19] (see appendix A)

$$\alpha = \frac{2p(2+p)}{(1+p)^2}. \tag{2.23}$$

For very small values of p, $\alpha \xrightarrow[p\to 0]{} = 4p$.

Second-order cross-correlation function between write and read photons

The second-order cross-correlation function between write and read photons $g^{(2)}_{w,r}$ is a measure of the non-classicality of the correlations between the write and read photons, which can be related with the fidelity of the

heralded entanglement between two separate ensembles. It is defined as

$$g^{(2)}_{w,r} = \frac{p_{w,r}}{p_w \cdot p_r} = \frac{\left\langle a^\dagger_w a^\dagger_r a_r a_w \right\rangle}{\left\langle a^\dagger_w a_w \right\rangle \cdot \left\langle a^\dagger_r a_r \right\rangle}. \tag{2.24}$$

As in the case of α, $g^{(2)}_{w,r}$ can be expressed as a function of p as (see appendix A)

$$g^{(2)}_{w,r} = 1 + \frac{1}{p}. \tag{2.25}$$

From equations (2.23) and (2.25), we see that α and $g^{(2)}_{w,r}$ are related, and α can be expressed as a function of $g^{(2)}_{w,r}$ as

$$\alpha = \frac{4}{g^{(2)}_{w,r}} - \frac{2}{\left(g^{(2)}_{w,r}\right)^2}. \tag{2.26}$$

The previous expression shows that high single read photons quality (or low value of α) is correlated with high values of $g^{(2)}_{w,r}$. High values of $g^{(2)}_{w,r}$ will also be related with a high fidelity of the entangled states in a QR architecture [26].

Cauchy-Schwarz inequality

For a pair of independent classical fields, the second order cross-correlation function between the two modes $g^{(2)}_{1,2}$ and the individual auto-correlation functions for each mode $g^{(2)}_{1,1}$ and $g^{(2)}_{2,2}$ have to satisfy the inequality

$$R = \frac{\left(g^{(2)}_{1,2}\right)^2}{g^{(2)}_{1,1} \cdot g^{(2)}_{2,2}} \leq 1, \tag{2.27}$$

which constitutes a particular case of the Cauchy-Schwarz inequality [153]. A violation of the condition expressed by eq. (2.27) indicates that non-classical correlations are present between the two modes. For DLCZ-type quantum memories, the joint quantum state for the write and read photons can be described by a two mode squeezed state. The write and read photonic modes individually display a thermal statistic, i.e. their second

order auto-correlation is equal to 2. In that case, the joint photon statistic shows a quantum behavior when the cross-correlation function exceeds the value of 2.

Fidelity of the memory

For DLCZ-type quantum memories, it has been shown that the fidelity of the memory can be directly inferred from the normalized cross-correlation function [125, 154]. For example, if the memory is used to create heralded qubits (using polarization or time bin encoding), the coherence of the state can be measured through a visibility given by

$$V = \frac{g^{(2)}_{w,r} - 1}{g^{(2)}_{w,r} + 1}. \tag{2.28}$$

The fidelity F can be related to V by the expression $F = (V + 1)/2$ (valid for qubit states), thus obtaining

$$F = \frac{g^{(2)}_{w,r}}{g^{(2)}_{w,r} + 1}. \tag{2.29}$$

It is worth noting that the classical threshold of $2/3$ for the qubit fidelity [155] is surpassed as soon as $g^{(2)}_{w,r}$ exceeds the value of 2.

Limitations of DLCZ quantum memories

The main and most obvious limitation of DLCZ QMs arises from the previous observation. One the one hand, high values of $g^{(2)}_{w,r}$ and low values of α are highly desirable. On the other hand however, these can only be achieved in the limit of low values of p (typically less than ten percent). Having a low value for p means that many write pulses have to be sent before successfully creating an heralded spin-wave. The direct consequence is that the spin-waves creation rate of the DLCZ QMs (entanglement generation rate of the DLCZ QRs) will inherently be limited. Depending on the requirements for the system, a tradeoff between photons detection rate and quality of the single photon or the correlations has to be met.

Fortunately, a solution to address this critical issue exists, which is the introduction of multiplexing in the existing protocol. The most convenient form of multiplexing for DLCZ QMs is the temporal one, allowing us to create and store spin-waves in many temporal modes with a train of write pulses. In case of a write photon detection, only the spin-wave correlated with the detected write photon is then read out. In the case of QRs application, this would increase the entanglement generation rate on the elementary segments by a factor equal to the number of storable modes in the memory, to first approximation. The part of my PhD work dedicated to this matter is presented in chapter 6.

A second limitation arises from the atomic species most commonly used to implement DLCZ QMs. Alkali metals are often used, due to their convenient electronic structure allowing to trap them efficiently in a MOT. Moreover, they can offer long coherence time making possible to obtain long memory lifetimes. The drawback is that the optical wavelengths used to interact with them are in the visible to near-infrared range (around 780 nm for ^{87}Rb), which is relatively highly absorbed in optical fibers (around 3 dB/km at 780 nm). This strongly limits the potential entanglement distribution distance for realistic QR applications, or the long distance transmission of single photons in general. A good solution to address this issue is to convert the frequency from alkali atoms resonant ones to the telecom C-band. The part of my PhD work dedicated to this matter is presented in chapter 5.

2.2 Quantum Frequency Conversion

In general, frequency conversion relies on non-linear processes happening in non-linear media. The various processes have to satisfy two conditions, which are energy conservation and momentum conservation. The conversion can take place either in bulk crystal, or in waveguides. Each one presents an advantage and an inconvenient in terms of efficiency and phase

matching. In bulk crystal, the beams must be focused in order to reach high efficiency, but a strong focus also reduces the interaction length. Waveguides offer the advantage of a stronger non-linear interaction, because the light is confined over the entire interaction length, permitting to use several centimeter length crystals. As a result, the efficiency is increased.

In both systems, dispersion due to a different refractive index for each wavelength involved prevents phase matching. This can be compensated in bulk crystals by taking advantage of birefringence, allowing to fulfill the phase matching condition by appropriate selection of the crystal orientation and the polarization of the fields. In commonly used waveguides realized by soft proton exchange, this technique is not possible because only one polarization is guided. The birefringence can also not be used in this waveguides, since the largest non-linear coefficient is achieved when all the fields are polarized along the crystalline axis. Quasi phase-matching can be used instead, as proposed in 1962 by Armstrong *et. al.* [156]. This technique is commonly implemented by means of periodical poling of the refractive index of the crystal.

2.2.1 Difference frequency generation

The theory presented in this section comes from [147, 157]. The most commonly used non-linear processes are three- and four-wave mixing. Here, we will focus on difference frequency generation (DFG), which is a three-wave mixing process where an incident field at frequency ω_i, associated to a pump field at ω_p, is converted into light at a lower frequency $\omega_s = \omega_i - \omega_p$.

Maxwell's equations in a dielectric media

We consider a non-linear, dispersive, homogeneous, isotropic and spatially non-dispersive dielectric material. Maxwell's equations in a material in

their general form write

$$\nabla \cdot \mathbf{D} = \rho_f, \tag{2.30}$$

$$\nabla \cdot \mathbf{B} = 0, \tag{2.31}$$

$$\nabla \times \mathbf{E} = -\frac{\partial \mathbf{B}}{\partial t}, \tag{2.32}$$

$$\nabla \times \mathbf{H} = \mathbf{J}_f + \frac{\partial \mathbf{D}}{\partial t}, \tag{2.33}$$

where $\mathbf{D} = \epsilon_0 \mathbf{E} + \mathbf{P}$ is the electric displacement, ρ_f is the density of free charges, $\mathbf{B} = \mu_0 \mathbf{H} + \mathbf{M}$ is the magnetic flux density, $\mathbf{E}$ is the electric field, $\mathbf{H}$ is the magnetic field, $\mathbf{J}_f$ is the free current density, $\mathbf{P}$ is the polarization density (electric dipole moment per unit volume), and $\mathbf{M}$ is the magnetization density (magnetic dipole moment per unit volume). In dielectric materials, $\mathbf{M} = 0$. The polarization $\mathbf{P}$ is the response of the medium to the electric field, such that in general $\mathbf{P}(\mathbf{r}, t) = \mathbf{P}(\mathbf{E}(\mathbf{r}, t); \mathbf{r}, t)$. In non-linear media, it can be decomposed into a linear and a non-linear part

$$\mathbf{P} = \mathbf{P}_L + \mathbf{P}_{NL} = \epsilon_0 \chi^{(1)} \mathbf{E} + \sum_j \epsilon_0 \chi^{(j)} \mathbf{E}^j, \tag{2.34}$$

where $\mathbf{P}_L = \epsilon_0 \chi^{(1)} \mathbf{E}$ is the linear component, $\mathbf{P}_{NL}$ is the non-linear component, $\chi^{(1)}$ is the linear susceptibility, and $\chi^{(j)}$ are the non-linear susceptibilities of order j. From this expression, it comes that $\mathbf{D} = \epsilon_0 \epsilon_r \mathbf{E} + \mathbf{P}_{NL}$, with $\epsilon_r = 1 + \chi^{(1)} = n^2$ the relative permittivity of the material, and n its refractive index. We also do the approximation $\mathbf{J}_f = \sigma \mathbf{E}$, with σ the electrical conductivity.

Using the identity $\nabla \times (\nabla \times \mathbf{E}) = \nabla(\nabla \cdot \mathbf{E}) - \Delta \mathbf{E}$ applied to eq. (2.33) in the case of a uniform charge density ($\nabla(\nabla \cdot \mathbf{E}) = 0$), we obtain the following wave equation for the electric field

$$\Delta \mathbf{E} - \mu_0 \sigma \frac{\partial \mathbf{E}}{\partial t} - \frac{\epsilon_r}{c^2} \frac{\partial^2 \mathbf{E}}{\partial t^2} = \frac{1}{\epsilon_0 c^2} \frac{\partial^2 \mathbf{P}_{NL}}{\partial t^2}. \tag{2.35}$$

We will now study the case of the DFG for classical light.

Let us come back to the expression of $\mathbf{P}$ of eq. (2.34). Since three-wave mixing processes arise from the second order non-linear susceptibility $\chi^{(2)}$, we will not take into account the higher order terms. For an electric field of the form $\mathbf{E}(t) = \mathbf{E}_1(t)\cos(\omega_1 t) + \mathbf{E}_2(t)\cos(\omega_2 t)$ corresponding to the signal and pump fields, we get

$$\mathbf{P}_{NL} = \epsilon_0 \frac{\chi^{(2)}}{2} \left[E_1^2(1 + \cos(2\omega_1 t)) + E_2^2(1 + \cos(2\omega_2 t)) \right. \\ \left. + 2\mathbf{E}_1\mathbf{E}_2 \left(\cos((\omega_1 - \omega_2)t) + \cos((\omega_1 + \omega_2)t) \right) \right]. \quad (2.36)$$

The terms oscillating at frequencies $\omega_1 - \omega_2$ (resp. $\omega_1 + \omega_2$) are responsible for DFG (resp. sum frequency generation).

The electric fields can be written as

$$E_j(x, y, z, t) = \xi_j u_j(x, y) a_j(z) e^{i(\omega_j t - k_j z)}. \quad (2.37)$$

Here, $\xi_j = \sqrt{2Z_0/n_j \hbar \omega_i}$ is a scale factor with $Z_0 = \sqrt{\mu_0/\epsilon_0}$ the impedance of free space and n_j the effective refractive index of mode j, $u_j(x, y)$ is the normalized spatial mode of the waveguide, $a_j(z)$ is a slowly varying envelope corresponding to the amplitude of mode j, and $k_j = \omega_j n_j / c$ is the propagation constant.

The scalar magnitudes of the nonlinear polarization at the three considered frequencies $\omega_s = \omega_i - \omega_p$ are [137]

$$P_{NL}(\omega_i) = \epsilon_0 \chi^{(2)} E(\omega_s) E(\omega_p), \quad (2.38a)$$

$$P_{NL}(\omega_s) = \epsilon_0 \chi^{(2)} E(\omega_i) E^*(\omega_p), \quad (2.38b)$$

$$P_{NL}(\omega_p) = \epsilon_0 \chi^{(2)} E(\omega_i) E^*(\omega_s). \quad (2.38c)$$

Combining equations (2.38) and (2.35), we get the following system of coupled equations

$$\left(\frac{d}{dz}+\frac{\alpha_i}{2}\right)a_i = -i\kappa a_s a_p e^{i\Delta k' z}, \tag{2.39a}$$

$$\left(\frac{d}{dz}+\frac{\alpha_s}{2}\right)a_s = -i\kappa a_i a_p^* e^{-i\Delta k' z}, \tag{2.39b}$$

$$\left(\frac{d}{dz}+\frac{\alpha_p}{2}\right)a_p = -i\kappa a_i a_s^* e^{-i\Delta k' z}. \tag{2.39c}$$

Here, $\Delta k' = k_s - k_i + k_p$ is the phase mismatch, α_j is the power attenuation coefficient, and

$$\kappa = \epsilon_0 \frac{\chi^{(2)}}{2}\left(\frac{2\hbar\omega_s\omega_i\omega_p Z_0^3}{n_s n_i n_p}\right)^{1/2}\Theta \tag{2.40}$$

is the coupling coefficient, where Θ is the mode overlap.

Let us now consider a totally converted weak signal, a strong undepleted pump, perfect phase matching ($\Delta k' = 0$) and no propagation losses ($\alpha_j = 0$). The initial conditions are $a_i(z=0) = a_{i0}$ and $a_s(z=0) = 0$. The undepleted pump assumption comes from the fact that it is much stronger than the input, such that $a_p(z) = a_p(z=0) = a_{p0}$ and $\frac{da_p}{dz} = 0$. The coupled equations simplify to

$$\left(\frac{da_i}{dz}\right) = -\gamma a_s \tag{2.41a}$$

$$\left(\frac{da_s}{dz}\right) = -\gamma a_i \tag{2.41b}$$

$$\left(\frac{da_p}{dz}\right) = 0, \tag{2.41c}$$

where $\gamma = \kappa a_p e^{-i\pi/2}$. Solving this system leads to

$$a_i(z) = a_{i0}\cos(\gamma z) \tag{2.42a}$$

$$a_s(z) = a_{i0}\sin(\gamma z). \tag{2.42b}$$

In this case, the intensities of the input signal and the output field show sinusoidal oscillations with a phase difference of $\pi/2$. This means that

periodically, the input signal is totally converted, followed by total back-conversion.

Defining the conversion efficiency as the ratio of the power at the signal target frequency at the output of the waveguide by the input power at the input of the waveguide, we obtain

$$\eta = \frac{|a_s(L)|^2}{|a_{i0}|^2} = \sin^2(\gamma L) = \sin^2(\sqrt{\eta_{norm} P_p} L), \tag{2.43}$$

where η_{norm} is the normalized efficiency and P_p the pump power.

Chapter 3

Experimental setup

In this chapter, I will explain the implementation and function of the different components of our experimental setup, which is used for DLCZ-type experiments. The core of this setup is a magneto-optical trap (MOT) [158], in which neutral ^{87}Rb atoms are cooled down to the 100 μK level and trapped. This trap is realized in an ultra-high vacuum (UHV) chamber, using continuous wave (CW) laser beams and a magnetic field gradient. The lasers used for the MOT also provide the probing beams used in our experiments. The coils for magnetic fields are controlled by a current driver, allowing to modify the current flowing through them in a short time scale of few tens of microseconds. Since I joined the group at its early beginning and started with an empty laboratory, the design and building of this experiment represents an important part of my PhD work. I will start by a description of the MOT in section 3.1, followed by the laser system necessary for our experiments in section 3.2. Then I will detail the composition of our vacuum system (section 3.3) and present the different coils we used to control the required magnetic fields (section 3.4). I will also present the detection apparatus and control system of our experiments (sections 3.5 and 3.6). The last section (3.7) of this chapter is a general characterization of the MOT. The QFC setup characterization will be detailed in the chapter dedicated to the QFC experiment.

3.1 The Magneto Optical Trap

A MOT is an apparatus allowing to obtain cold clouds of neutral atoms, suitable to be used for various types of experiments. Atoms originating from a low pressure vapor created in a vacuum chamber are laser-cooled below the Doppler limit, and trapped at a specific position thanks to the introduction of a quadrupolar magnetic potential. The final velocity of atoms in such traps can be as low as a few tens of centimeters per second. The first experimental realization of a MOT with neutral atoms has been done with sodium in 1987 [158]. In this section, I will introduce ^{87}Rb,

the atomic species used in our experiment, before describing the physical processes involved in the magneto optical trapping.

3.1.1 Atoms trapped in our MOT: Rubidium 87

Rubidium is a chemical element of the alkali metal group, with atomic number 37 and an atomic mass of 85.4678u. Alkali metals appear in the first column of the periodic table, and have one valence electron in the s-shell. Natural rubidium is a mixture of two isotopes: ^{85}Rb and ^{87}Rb. ^{85}Rb is stable and forms 72% of the mixture. The remaining 28% is formed by ^{87}Rb, which is radioactive with a half-life of 48.8×10^9 years, making it effectively stable. It decays to strontium 87 (^{87}Sr), which is stable, by negative beta decay: ${}^{87}_{37}Rb \rightarrow {}^{87}_{38}Sr + e^- + \bar{\nu}_e$. This means that the ^{87}Rb atom is converted to an atom with one higher atomic number (^{87}Sr in this case), while emitting an electron and an electron antineutrino [159, 160].

Rubidium was discovered in 1861 by Robert Bunsen and Gustav Kirchhoff by spectroscopy, one year after the invention of the spectroscope by themselves. It is frequently used for laser-cooling based experiments, due to the fact that it has a cycling transition, the ability to fabricate relatively low priced diode lasers at the resonant frequencies, and the moderate temperatures required to obtain substantial vapor pressures.

We use the D_2 line of ^{87}Rb. We chose ^{87}Rb over ^{85}Rb mainly because of its simpler energy levels structure, simplifying the optical pumping processes. Its energy levels are shown in Fig. 3.1. The D_2 line corresponds to a transition between the ground and first excited states. The fine structure results from the coupling between the orbital angular momentum $\mathbf{L}$ of the outer electron and its spin angular momentum $\mathbf{S}$, giving a total electron angular momentum

$$\mathbf{J} = \mathbf{L} + \mathbf{S}. \tag{3.1}$$

The associated quantum number can then range between

$$|L - S| \leq J \leq L + S. \tag{3.2}$$

In the case of ^{87}Rb, S equals 1/2. In the ground state, L equals 0 so J equals 1/2. For the first excited state, L equals 1 so $J \in \{\frac{1}{2}, \frac{3}{2}\}$. For the D_2 line, J equals 3/2, and the transition is labeled as $5^2S_{1/2} \rightarrow 5^2P_{3/2}$. Here, 5 is the principal quantum number of the outer electron, the superscript 2 is equal to the multiplicity $2S + 1$, the letters S and P refer to the value of L (resp. 0 and 1), and the subscript is equal to J. The fine structure comprises hyperfine levels, resulting from the coupling of **J** with the nuclear spin **I**, giving a total atomic angular momentum

$$\mathbf{F} = \mathbf{J} + \mathbf{I}. \tag{3.3}$$

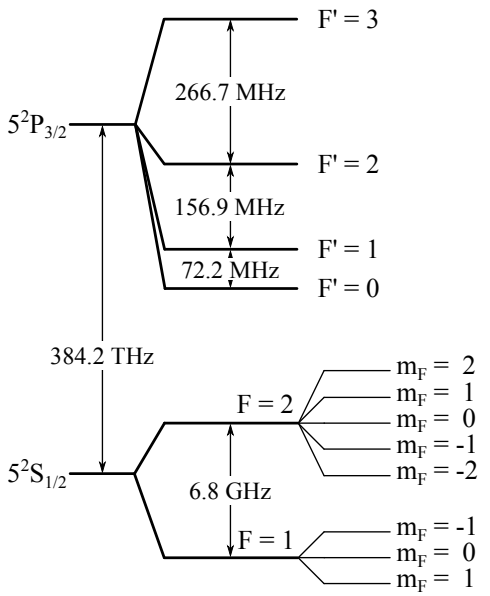

FIGURE 3.1: **Rubidium 87 D_2 transition energy levels.** F (resp. F') are the hyperfine ground (resp. excited) states, and m_F are the Zeeman states represented only for the ground states.

The rule for the associated quantum number is

$$|J - I| \leq F \leq J + I. \tag{3.4}$$

In the case of ^{87}Rb, $I = 3/2$, so for the ground state, $F \in \{1, 2\}$, and for the excited state of the D_2 line, $F \in \{0, 1, 2, 3\}$. The D_1 and D_2 lines are approximately 15 nm apart, which is much bigger than the hyperfine splitting and the linewidth of our laser radiation, such that it can be completely neglected.

The hyperfine levels also contain $2F + 1$ magnetic sub-levels called Zeeman levels, which determine the angular distribution of the electron wave function. In the absence of external magnetic fields, the Zeeman levels are degenerate. However, when an external magnetic field is applied, their degeneracy is broken. To lowest order, the levels split linearly, proportionally to the magnetic field and the Landé g-factor [160].

In the rest of the thesis, I will refer to the atomic hyperfine levels used for ground states as F, and for excited states as F', for ease of distinction (see Fig. 3.1).

3.1.2 Physical processes in a MOT

A MOT combines optical and magnetic fields in order to achieve stable trapping of atomic species. The light by itself creates a velocity-dependent potential similar to a friction force, allowing to cool atoms down to temperatures of the order of 100 μK. The combination with a magnetic field gradient allows to go further down in temperature, and creates a position-dependent harmonic potential. See appendix B for a detailed explanation of these processes.

3.1.3 Configuration of our MOT

Our trap is a single stage 3D MOT done in a single vacuum chamber at UHV pressure levels. A schematic view of the setup is shown in Fig. 3.2. The rubidium atoms are released from the dispensers towards the science

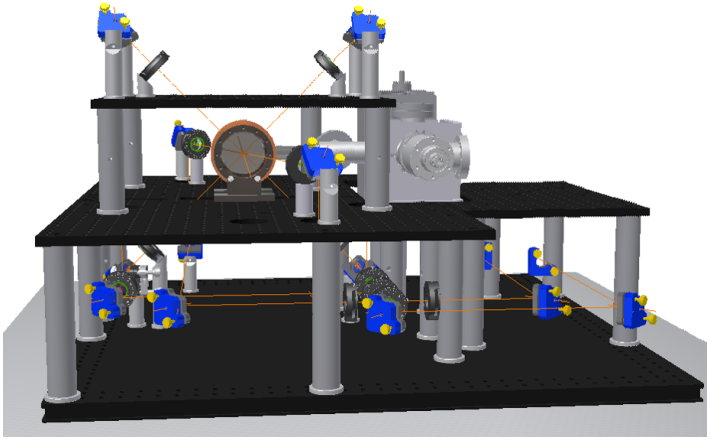

FIGURE 3.2: **3D view of our setup.**

chamber. The MOT is passively loaded from the background gas. Initially, a set of 6 independent counterpropagating beams combining trapping and repumping light was used. This has been replaced by a set of 3 back-reflected beams for the cooling laser, and one back-reflected beam for the repumper, for simplicity of the experimental setup. At low beam intensities, the retro-reflected configuration can be problematic due to a shadowing effect caused by the atoms on the reflected beams. However, at our intensity levels, this effect is negligible. One beam of the cooling laser is sent horizontally, while the other two are sent diagonally with a 45° angle. The repumping beam is sent horizontally and back-reflected. A pair of standard magnetic coils is used to produce the quadrupolar magnetic field. A set of 3 pairs of coils are used to control the homogeneous magnetic field on the atoms. All these elements are going to be detailed in the next sections of this chapter. In order to be able to place optics at the height of the trapped atoms, we have placed an intermediate breadboard

around the science chamber. A second breadboard on top of this one has been placed in order to support the diagonal cooling beams.

3.2 The laser system

We used three different lasers for the experiments in which I was involved. Two of them are used for the cold atoms trapping and the beams of the DLCZ experiments: the cooling and the repumper lasers. The third one is used for the QFC experiment: the telecom pump laser.

3.2.1 The cooling laser

The cooling laser is a combination of an external cavity diode laser (ECDL) acting as a master laser followed by a tapered amplifier, delivering up to 1.5 W at 780 nm, from Toptica (TA pro). It is frequency stabilized, because we have to address absolute optical transitions of ^{87}Rb. This laser is used to drive the transitions starting from the $|F = 2\rangle$ ground state. The high power amplified output is split into the several laser lines required for the experiments. The amount of light sent to each laser line is selected by a half-wave plate and a polarizing beam-splitter, sending the vertically-polarized component of the beam into the laser line. Each line is based on a double-pass acousto-optic modulator (AOM) configuration, allowing us to apply a controlled frequency shift which can be different for each line, and to modulate the light amplitude to create pulses. This control of the frequency is necessary to address the different relevant atomic transitions, which are split by few tens or hundreds of MHz from each other as seen in Fig. 3.1.

The first line is used for the cooling beams of the MOT. It is off-resonantly addressing the $|F = 2\rangle \rightarrow |F' = 3\rangle$ transition, in order to Doppler cool the atoms. The second line is used for the write or read beam, depending on the atomic levels configuration for each experiment. In both cases, it is

addressing the $|F = 2\rangle \rightarrow |F' = 2\rangle$ transition, off-resonantly if used as a write beam, and resonantly if used as a read beam. The third line is used for optical pumping in the case of the controlled rephasing experiment (see chapter 6. It is slightly off-resonantly addressing the $|F = 2\rangle \rightarrow |F' = 2\rangle$ transition. Light from an auxiliary output of the master diode (before amplification) is used for the frequency stabilization. This allows us to bring the frequency of the light of this laser close to the atomic transitions used in our experiments, and to use AOMs in order to precisely address each one of them. The frequency locking method is explained in 3.2.5.

3.2.2 The repumping laser

In order to cool rubidium, light with a significantly different frequency is required in order to transfer back the atoms decaying in the $|F = 1\rangle$ ground state on the $|F = 2\rangle$ state to maintain the interaction with the cooling laser. Since these two levels are split by about 6.8 GHz, it is common to use a second laser in order to interact with the transitions from this first level. However, this could also be achieved by modulating light from the cooling laser with an electro-optic modulator (EOM).

The repumping laser is also an ECDL. The required power for this laser being lower than for the cooling one, it is not amplified. First we used an ECDL from Radiant Dyes (NarrowDiode), before switching to a DL Pro from Toptica. The output of the laser is split into several lines controlled by AOMs, similarly to the cooling laser. The first line is used as a repumper for the MOT. It is resonantly addressing the $|F = 1\rangle \rightarrow |F' = 2\rangle$ transition. The second line is used for the same purpose as the second line of the cooling laser, with opposite roles, i.e. as read or write beam. It is addressing the $|F = 2\rangle \rightarrow |F' = 2\rangle$ transition as well. A third line is used for the frequency stabilization.

3.2.3 The probing beams

In order to perform all the DLCZ-type experiments, two pairs of counter-propagating beam lines are necessary. They are separated by an angle between 1° and 3° depending on the experiment, and are focused and overlapping on the atomic cloud, near the center of the quadrupolar magnetic field. The first pair is used for the write and read beams. The $1/e$ beam waist radius is about $150\,\mu$m. The write beam typically has a power of several hundreds of microwatts, and the read beams is in the low milliwatt range. The second pair is not used to send light, but to collect the write and read photons. The $1/e$ beam waist radius is narrower, about $50\,\mu$m, in order to ensure a good overlap with the write/read beams mode, and to collect the photons from a region where the intensity of the write and read beams is more homogeneous.

3.2.4 The telecom pump

This laser is used exclusively for the QFC experiment. It is an ECDL amplified using an external amplifier. The master laser is a DL Pro from Toptica. Its wavelength is set to 1569 nm. The amplifier is an erbium doped fiber amplifier from Keopsys. The total power available with this system is more than 2 W, from which up to 800 mW could be used for our QFC experiment, while the rest was used for other experiments. Since the bandwidth of the difference frequency generation process in our experiment is much larger than the linewidth of this system, it was not actively stabilized in frequency.

3.2.5 Frequency stabilization of the lasers

We need to address precise atomic transitions with the lasers in our experiments, which has two consequences. First, the laser linewidth must be much narrower than the one of the excited levels which we are using. For

^{87}Rb, this linewidth is approximately 6 MHz. Since we use two ECDLs, with intrinsic linewidths of few tens to hundreds of kHz, this is not a problem. Second, we must maintain the laser frequency close to the atomic transitions frequencies, in order to be able to address them by means of several AOM lines. This frequency stabilization is done with the standard Doppler-free saturated absorption spectroscopy technique, which is explained in the following.

A single laser beam is split into three different paths by passing it through a thick uncoated glass substrate tilted by 45°. The reflection on the front and back surfaces are about 4% for each one. This produces two weak parallel reflected beams w_1 and w_2 with low intensity, while the transmitted one has higher intensity. The two weak beams are passing together through a transparent glass cell filled with a mixture of rubidium 87 and 85. The cell is at room temperature, corresponding to a vapor pressure of about 5.0×10^{-10} bar at 25°C. The strong beam s is sent almost counter-propagating and overlapped with only one of the two weak beams. This is depicted in Fig. 3.3.

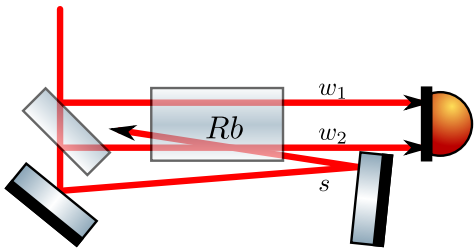

FIGURE 3.3: **Setup for the Doppler-free saturated absorption spectroscopy.**

First, let us focus on w_1. If the frequency of the light is swept around the rubidium resonances, a Doppler-broadened absorption spectrum is observed on the photodiode. This will be used as a reference to be subtracted in order to obtain the Doppler-free signal. The velocity distribution of the

atoms follow a Maxwell-Boltzmann distribution:

$$P_v(v)dv = \sqrt{\frac{m}{2\pi k_B T}} e^{-\frac{mv^2}{2k_B T}} dv \tag{3.5}$$

The expression for the Doppler shift in frequency is:

$$f = f_0 \left(1 + \frac{v}{c}\right) \tag{3.6}$$

From this, we find that

$$v = c\left(\frac{f}{f_0} - 1\right), dv = \frac{c}{f_0} df \tag{3.7}$$

Replacing v and dv by f and df in 3.5, we obtain:

$$P_f(f)df = \sqrt{\frac{mc^2}{2\pi k_B T f_0^2}} e^{-\frac{m\left[c\left(\frac{f}{f_0}-1\right)\right]^2}{2k_B T}} df \tag{3.8}$$

This corresponds to a Gaussian profile with a FWHM equal to:

$$\Delta f = 2\sqrt{2ln(2)}\sqrt{\frac{k_B T f_0^2}{mc^2}} \tag{3.9}$$

In the case of rubidium at room temperature, this gives $\sim 500\,\text{MHz}$, which is much larger than the linewidth of the atomic transitions.

The beam w_2 combined with the pump s allows to resolve the spectral features which are narrower than the Doppler broadening, like the hyperfine transitions we are interested in. At frequencies where both the probe and the pump are resonant with an atomic transition, the pump saturates the atomic transition, promoting about half of the atoms to the excited state, which allows the probe to be transmitted. This situation occurs in two different cases. First, let us consider a frequency with no detuning from an atomic transition. Both the probe and the pump will be resonant with atoms having no velocity component in the direction of the beams, meaning no Doppler shift. Second, moving atoms can be resonant with the probe and the pump light on two separate transitions

starting from the same ground state. This is true if more than one excited states are present, which is the case for alkali atoms in general. It happens at frequencies which are exactly between two atomic transitions, called crossover frequencies ν_c. Considering two transitions with frequencies ν_1 and ν_2, some atoms will see the pump Doppler-redshifted with the transition frequency ν_1 and at the same time the probe beam blueshifted to ν_2, and vice versa, such that

$$\begin{aligned} \nu_1 &= \nu_c - \frac{v_a}{c}\nu_c \\ \nu_2 &= \nu_c + \frac{v_a}{c}\nu_c, \end{aligned} \tag{3.10}$$

resulting in the following expression for the crossover frequency

$$\nu_c = \frac{\nu_1 + \nu_2}{2}. \tag{3.11}$$

Finally, the signal produced by w_1 is subtracted from the one produced by w_2 and s, allowing to remove the Doppler broadening from the final spectrum. Such a spectrum obtained with this method is shown in Fig. 3.4 (top) for the D_2 line of ^{87}Rb, starting from the ground state $|F = 2\rangle$. We observe 6 transmission peaks. Three correspond to frequencies resonant with the transitions $|F = 2\rangle \rightarrow |F' = 1, 2, 3\rangle$, and three to the crossovers between these three excited states. The excited state $|F' = 0\rangle$ does not appear here, since it is a forbidden transition.

This spectrum is then used in order to stabilize the frequency of the laser, which is achieved by means of frequency modulation and demodulation. The idea is to produce an error signal which is the derivative of the absorption spectrum, as explained in appendix C, and to use it for frequency correction. The error signal , shown in Fig. 3.4 (bottom), is sent to a PID controler implemented on a microcontroller board. The target is the zero-crossing of the error signal for the crossover between the $|F = 2 \rightarrow F' = 2\rangle$ and $|F = 2 \rightarrow F' = 3\rangle$ transitions. The correction is finally done with a

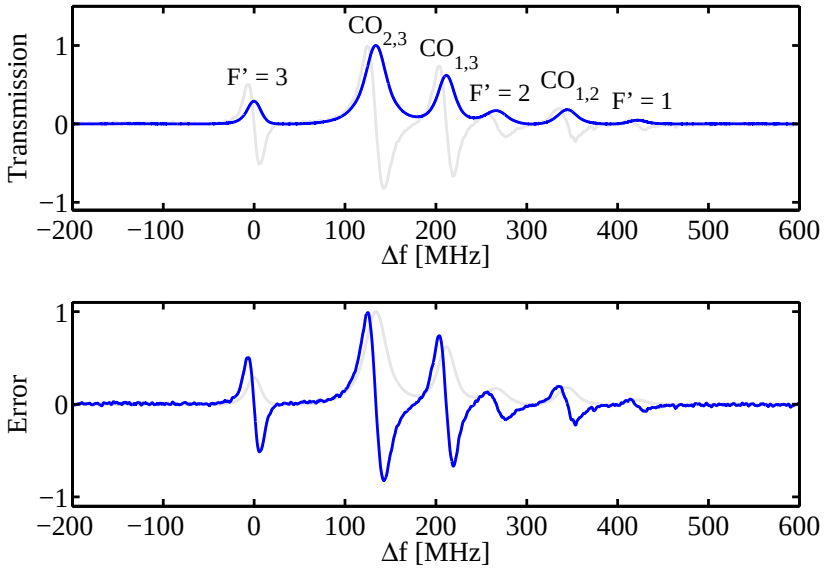

FIGURE 3.4: **Doppler-free saturated absorption spectroscopy spectrum.** (Top) Normalized transmission, with the corresponding transitions and crossovers. (CO) Crossover frequencies. (Bottom) Corresponding normalized error signal. The horizontal axis is the frequency detuning with respect to the $|F = 2\rangle \rightarrow |F' = 3\rangle$ transition.

feedback on the piezoelectric element controlling the grating forming the external cavity of the master laser.

Frequencies of the cooling laser lines.

I will now explain how the frequencies of the different AOMs are chosen, based on the setup of Fig. 3.5.

The frequency of the laser light at the master or amplified output is ν_{laser}, and the frequencies after the different AOM lines are labeled with $\nu_{...}$. The frequencies shifts given by the AOMs are labeled as $\nu^{...}_{AOM}$. The frequencies of the atomic transitions between levels a and b are labeled as $\nu_{a\rightarrow b}$. All the AOMs are set in double-pass configuration on the -1 order. By definition, $\nu_{lock} = \nu_{laser} - 2\nu^{lock}_{AOM}$ or equivalently

$$\nu_{laser} = \nu_{lock} + 2\nu^{lock}_{AOM}. \tag{3.12}$$

We lock on the crossover between the $|F = 2\rangle \rightarrow |F' = 2\rangle$ and $|F = 2\rangle \rightarrow |F' = 3\rangle$ transitions, because it is the transmission peak with the highest amplitude, allowing us to obtain the best possible error signal. Moreover, all the other AOM frequencies necessary to address the transitions of interest are easily accessible from there. Hence, we choose $\nu_{lock} = \nu_{2\rightarrow 3'} - \frac{1}{2}\nu_{2'\rightarrow 3'}$. From this we obtain

$$\nu_{laser} = \nu_{2\rightarrow 3'} - \frac{1}{2}\nu_{2'\rightarrow 3'} + 2\nu_{AOM}^{lock}. \tag{3.13}$$

For the trapping line addressing the $|F = 2\rangle \rightarrow |F' = 3\rangle$ transition, we have $\nu_{trap} = \nu_{laser} - 2\nu_{AOM}^{trap} = \nu_{2\rightarrow 3'}$. Replacing ν_{laser} by its previous

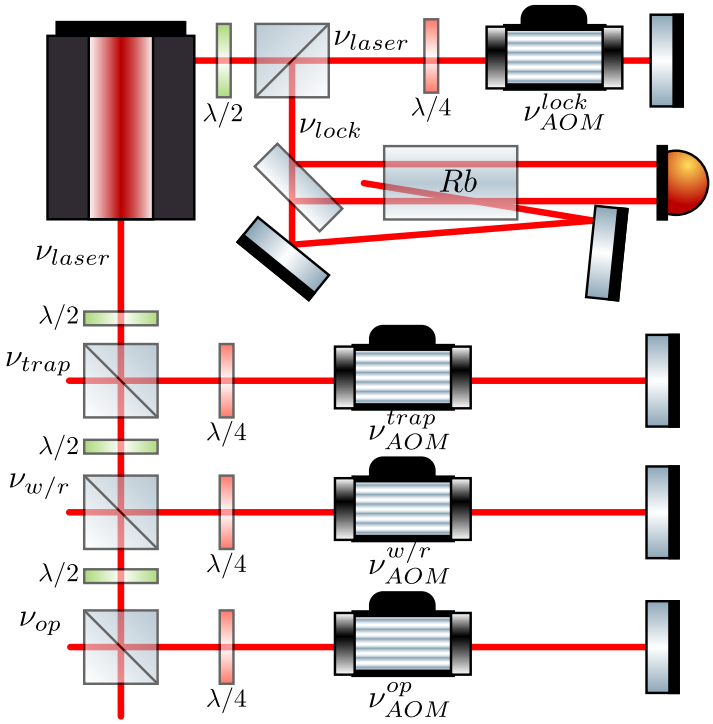

FIGURE 3.5: **Representation of the cooling laser lines.** The master output is sent to the frequency stabilization setup after passing through an AOM. The amplified output is split into the several beams necessary to perform the DLCZ experiments. All the AOMs are set in double-pass configuration.

expression, we get after simplification

$$\nu_{AOM}^{trap} = \nu_{AOM}^{lock} - \frac{1}{4}\nu_{2'\to 3'}. \tag{3.14}$$

We chose $\nu_{AOM}^{lock} = 180\,\text{MHz}$, and knowing that $\nu_{2\to 3'} = 266\,\text{MHz}$, we find the resonant AOM frequency for the trapping light to be $\nu_{AOM}^{trap} = 180 - \frac{266}{4} = 113.5\,\text{MHz}$. Similarly, we find the resonant AOM frequency for the write/read light on the $|F = 2\rangle \to |F' = 2\rangle$ transition to be $\nu_{AOM}^{w/r} = 246.5\,\text{MHz}$.

Frequencies of the repumping laser lines.
This case is simpler than the previous one, since both laser lines derived from this laser, used for repumping and read/write, are on the same transition ($|F = 1\rangle \to |F' = 2\rangle$). This allows us to use the same AOM frequencies for the locking and both laser lines. We chose to use double-pass configuration AOM lines on the +1 order at 250 MHz.

3.3 The ultra high vacuum chamber

The vacuum chamber is the central element for any cold atoms experiment. Its goal is to provide an extremely low pressure environment, allowing to load a low pressure pure vapor of the chosen atomic species. If the pressure is too high, the collisions with the background gas prevents the loading of cold atoms in a MOT. The typical pressure range to operate a MOT is on the order of $10^{-9}\,\text{mbar}$, which is in the UHV region. This requires that all the vacuum parts are thoroughly cleaned, with no organic matter present, such as fingerprints. This would lead to sublimation of this matter at low pressures, preventing from reaching the desired low pressure levels. The connections between the different elements also have to be carefully sealed with copper gaskets. The final pressure achievable is then an equilibrium between the pumping speed, the outgasing due to gas trapped in the metallic walls of the chamber and organic matter, and the leakage

through the connections. The chamber used in our setup meets three main requirements, namely compactness, ability to reach UHV pressure levels, and limited sensitivity to spurious magnetic fields, thanks to its design and choice of components. A schematic view is shown in Fig. 3.6. The chamber

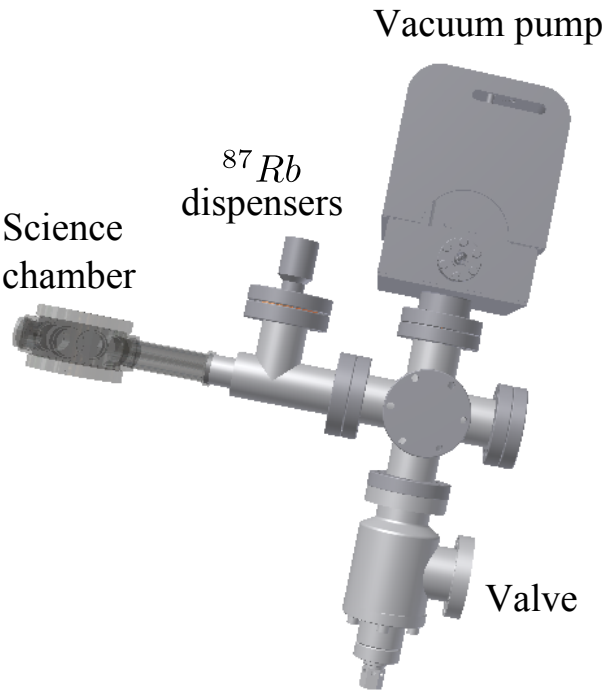

FIGURE 3.6: **3D top-view of the vacuum chamber.**

is composed of 3 main parts: a vacuum pump, a science chamber where the MOT is created, and a rubidium source. Additionally, there is a corner valve allowing to connect an auxiliary vacuum pump in order to reach a low enough pressure level before turning the ion pump on when starting from atmospheric pressure. This auxiliary pump usually consists in a rotary pump allowing to reach the 10^{-2} mbar region, and a turbomolecular pump going down to the 10^{-8} mbar region. All the components are connected via a central 5-ways cross. The pressure achieved in our chamber when the rubidium dispensers were off was as low as 3.61×10^{-10} mbar, and the

pressure with the dispensers switched on in order to observe a MOT was typically of a few times 10^{-9} mbar.

The vacuum pump

We use an ion pump from Gamma Vacuum (TiTan CV) with a pumping speed of 40 l/s. Its dimensions are 209 mm × 251 mm × 130 mm and it weighs 16 kg. It is surrounded by a magnetic shielding strongly reducing the magnetic field gradient around the pump. The valve allowing us to connect an external turbo pump is an all-metal angle valve from Tecnovac.

The science chamber

We use a custom cylindrical quartz chamber with an octagonal circumference, from Precision Glassblowing. A picture of the chamber is shown in Fig. 3.7.

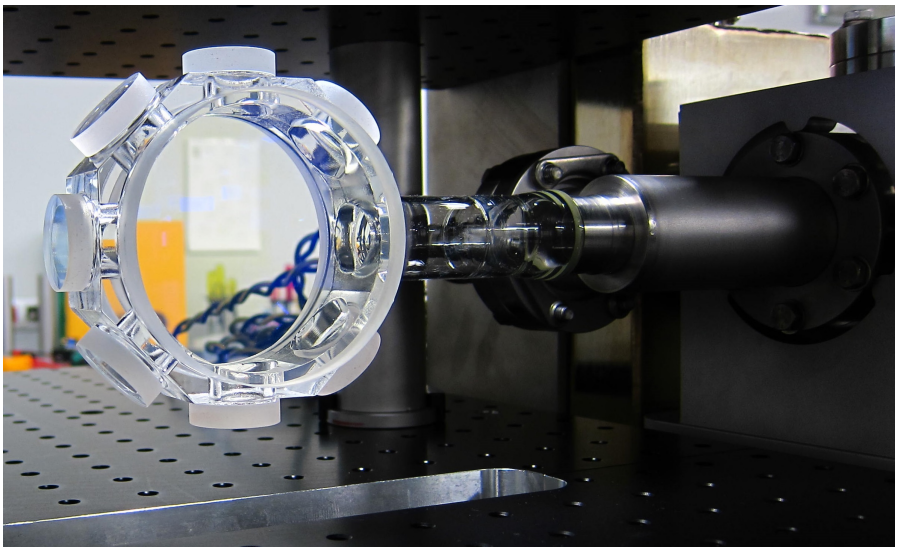

FIGURE 3.7: **Side view of the science chamber.**

Each base of the chamber is a single large viewport of 3" diameter. Each facet of the octagon is a smaller viewport of 1" diameter, except for one where a tube is connected to a standard vacuum flange via a glass-metal

transition. The chamber is also externally and internally anti-reflectively coated for light at 780 nm. There are two reasons to justify the choice of that type of chamber. The first one is that for some of our experiments, we need to control the magnetic field produced by the MOT coils in very short timescales. The fact that the chamber is entirely made of quartz, which is non magnetic, greatly limits induced currents which in turn could produce spurious magnetic fields. The second one is that this shape offers large optical access to the atoms trapped inside.

The rubidium source

The rubidium atoms sources are two independent cylindrical dispensers from Alvatec. They contain an alloy made of rubidium and bismuth, with 300 mg of rubidium in each dispenser. The alloy allows the rubidium to be stable in its solid form at room temperature under the low pressure condition. Rubidium is then released through a cut on the side of the cylinders by heating the dispensers via Joule effect. In the proper temperature range, only rubidium is sublimated, while the remaining part of the alloy remains stable in its solid form. They are oriented in such a way that the rubidium is released in the direction of the science chamber and not of the ion pump, in order to maximize the ratio of captured atoms over released atoms.

3.4 The magnetic coils

The final required component for a MOT are the magnetic coils producing the magnetic field gradient. However, they are not the only magnetic coils present in our setup. Since most of the atomic transitions used in our experiments are magnetic-sensitive, we need to be able to control the homogenenous magnetic field around the position of the MOT. This is done via a set of 3 pairs of large coils allowing to produce an homogenenous magnetic field independently in the three directions of space.

3.4.1 The MOT coils

Building of the coils

Our MOT coils consist of 7 layers of 8 windings, using a copper wire of 1.5 mm diameter. The inner radius of the coils is 4 cm. The distance separating the two coils is approximately 4 cm, allowing us to operate near the anti-Helmholtz configuration regime. They are glued on a mount made of machinable plastic, serving the same purpose as having a quartz cell, namely avoiding the creation of induced current when rapidly varying the current flowing in the coils. The wire is maintained in its original shape with epoxy. The typical current used is 7 A, making active cooling of the coils unnecessary. The coils are mounted along an horizontal axis, creating an axial gradient of 20 G/ cm and a radial gradient of 10 G/ cm, measured with a Hall probe. We measured an inductance $L \approx 400\,\mu$H for each coil. The main requirement for these coils is that they must allow a total current inversion in a few tens of microseconds. This requires a specific current driver, since simple passive loading or unloading would lead to switching times in the order of a few milliseconds.

Current driver

Our MOT coils current driver is based on insulated-gate bipolar transistors (IGBTs). This type of transistors are commonly used as electronic switches, since they allow very fast switching (typically few hundreds of nanoseconds), and are able to handle high currents and current spikes. Two different modes can be used: either the current is just switched off for standard DLCZ experiments, or it is reversed for the controlled rephasing experiment. The driver schematic is shown in Fig. 3.8. A standard power supply acts as a current source for the coils. An H-bridge allows us to select the direction of the current flowing through the coils. The compensation arm is connected while the coils are switched off, to provide the power supply with a constant impedance load. A capacitor loaded by a high voltage power supply is connected in parallel with the coils during the switching

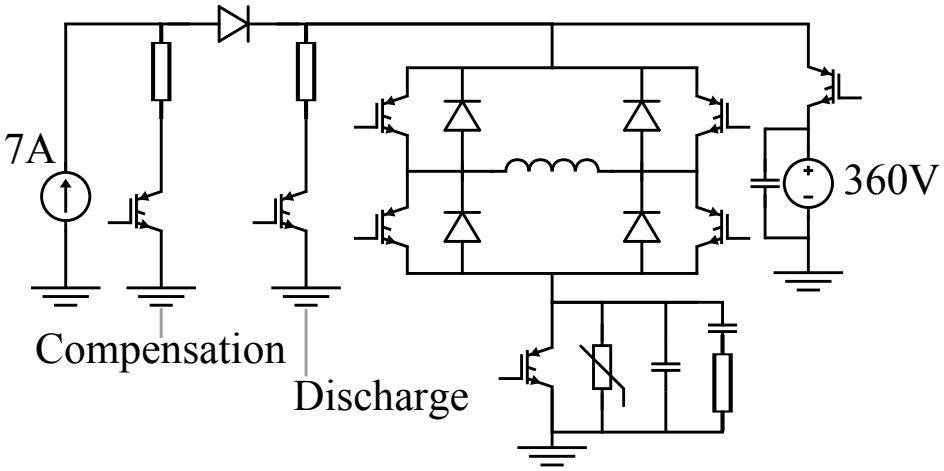

FIGURE 3.8: **Current driver schematic for the MOT coils.**

on, in order to rapidly load them via an RLC resonance mechanism. During the switching off, the power supply is decoupled via the compensation arm, and then the IGBTs of the H-bridge and of the discharge arm are switched on together in order to allow a fast discharge of the coils towards the ground. The sign of the current can also be changed while the coils are active. For this, a switching off phase is directly followed by a switching on with the H-bridge inverted. This circuit is controlled by a state machine programmed on a field-programmable gate array (FPGA). There are two inputs, one for the on/off state an one for the current sign, and eight outputs, one per IGBT. Only a change in one or both of the inputs can modify the configuration of the outputs. The state at any given time is conditioned on the previous state and on the inputs' state at that time. Timings for the coils charge and discharge, in particular during the high voltage transition, are carefully adjusted in order to reach a stable steady state value in a minimum amount of time.

3.4.2 The compensation coils

These coils are designed to cancel the static homogeneous magnetic field at the position of the MOT. Its principal contribution is the Earth's magnetic

field, whose magnitude is typically around 0.5 G, mainly in the vertical direction. The environment of the experiment also affects it, including other neighboring labs, particularly active electrical devices like power supplies generating magnetic fields. Since it can vary depending on the environment, it is necessary to have a controllable compensation method. For this, we use a set of 3 pairs of coils in an approximate Helmholtz configuration. It is approximate, because the coils are rectangular for simplicity of integration in the experimental setup, and the distance between two coils of the same pair is not exactly equal to their mean radius. However, since these coils are fairly big (typically around 50 cm side), this is a good approximation. According to our simulations, we expect the magnetic field produced to be homogeneous within less than five percent over a few centimeters around the center, such that the magnetic field on the MOT, which is only a few millimeters, should be constant within our precision requirements.

The main constraint for the compensation coils was the ability to integrate them in our existing setup without any major modification, while maintaining them in a configuration close to the Helmholtz one. For this purpose, we designed them to fit around the middle and top breadboards of the setup for the set of coils oriented along the horizontal **x** and **y** axes. We placed the third pair closer to the cell in order to be able to create a stronger field in the vertical **z** direction. Moreover, we wanted to be able to supply them with currents much lower than one Ampere, without requirements on the charge or discharge speed. This allowed us to conveniently use standard computer ribbon cables and standard insulation-piercing contact connectors. The frame is made of electrical wire gutter trunking elements, allowing us to build these coils in a rectangular shape in a very easy way.

The coils must be stabilized in current at the tens of milli-Ampere level. For this, we use 3 independent current drivers, one for each pair of coils. They stabilize the current, and offer a monitoring output with a voltage proportional to the applied current. Precise calibration via a microwave

spectroscopy technique yielded values of 0.1 G/ V for the X and Y coils, and 0.45 G/ V for the Z coil.

3.5 Detection apparatus

Our experiments rely on single photon counting. For this purpose, we used up to 4 different SPDs. However, this kind of measurement is extremely sensitive to spurious light, which can be ambient light or can originate from the experiment beams or from the atoms. In order to isolate the single photons from spurious light at different frequency, which can be collected into the same optical fibers, we use frequency filtering cavities (FFCs).

3.5.1 The frequency filtering cavities

We place one FFC between the single photons collection fibers and the SPDs for both detection arms. They consist of monolithic Fabry-Perot cavities with a FWHM of 60 MHz and a free spectral range (FSR) of 12 GHz. The cavity is formed by a plano-concave lens coated on both sides with a high reflectivity layer at 780 nm, following the design described by [161]. The single photons are delivered by the collection optical fiber to a free-space setup where they are shaped to match the TEM_{00} mode of the cavity. The length is tuned by acting on the lens temperature and is adjusted to be resonant with the single photon's frequency. The cavity transmission is 50% when measured with monochromatic light. The photons filtered by the resonator are then coupled with 50% efficiency into another fiber connected to the SPD. The total transmission of the system, including losses and fiber in-coupling efficiency, is measured to be 25% when probed with monochromatic cw light.

3.5.2 The single photon detectors

In the standard DLCZ-type experiments, we usually use a pair of single photon detectors (COUNT-100-FC, from Laser Components), with a measured detection efficiency of 43% and dark counts rates around 100 Hz. For some measurements like anti-bunching experiments using a Hanbury-Brown and Twiss type of interferometer, we introduce a third detector with similar efficiency and dark counts rate (SPCM-AQRH, from Excelitas). Finally, for the frequency conversion experiments, we replace one of the two main SPDs by a telecom one (ID201, ID210, ID220, from IDQuantique).

3.6 Software experimental control

All our experiments are controlled by the same hardware/software solution. It consists of a National Instruments rack in which digital and analog FPGA-based modules are mounted, developed by an ICFO start-up called Signadyne. More specifically, we have one digital module with 32 input/output channels (SD-PXE-DIO-H0002), one analog module with 4 output channels able to deliver frequencies up to 200 MHz (SD-PXE-AOU-H0002), another one reaching up to 400 MHz (SD-PXE-AOU-H0004), and finally a time-to-digital converter (TDC) module with 4 inputs and a resolution of 320 ps (SD-PXE-TDC-H0002). The digital module allows us to generate all the triggers used in our experiment, as well as to control the coils driver circuit. The analog modules are used as source to drive the AOMs which create the different beams required for our experiment. They also support arbitrary waveforms for amplitude and frequency modulation, making it possible to temporally shape light pulses as well as chirp them if needed. Finally, the TDC module is used in combination with the SPDs in order to record the single photons arrival times. This allows us to calculate the relevant characteristic values of our experiment, as well as to construct real-time histograms for data visualization.

These different modules are controlled via a user interface developed by the same company, including two different softwares. One allows us to manually control each of the analog and digital channels, as well as to display real-time histograms based on the TDC module acquisitions. The other one is a sequencer, with which we implement the experiment timelines for each of our experiments. An example can be seen in chapter 4. Moreover, we developed a LabView interface allowing us to run sets of measurement in an automatized way by communicating with the sequencer.

3.7 MOT characterization

In this section, I will show measurements about the number of atoms trapped in our MOT, and then optical depth (OD) measurements.

3.7.1 Atom number measurement

The measurement of the number of atoms trapped in a MOT can be done in various ways. We performed a fluorescence measurements with a charge-coupled device (CCD) camera. The detector is made of 1024×768 pixels of $4.65\,\mu$m size.The CCD camera is set up as a 1:1 imaging system, such that the size of the image of the atomic cloud projected on the CCD chip is as close as possible to the actual one. To do so, we place a converging lens equidistant from the center of the atomic cloud and the CCD chip, such that the distances chip-lens and lens-atoms are equal to the double of the focal length f. The lens is carefully placed at a distance $2f = 10\,$cm from the CCD chip by placing it in a variable-length tube. Then the position of the CCD camera is adjusted such that the most distinct possible image of the atomic cloud is formed. A typical fluorescence image is shown in Fig. 3.9.

We calibrated the CCD camera to know the relationship between gain, exposure, incident power and the zero-order moment M_0 of the image.

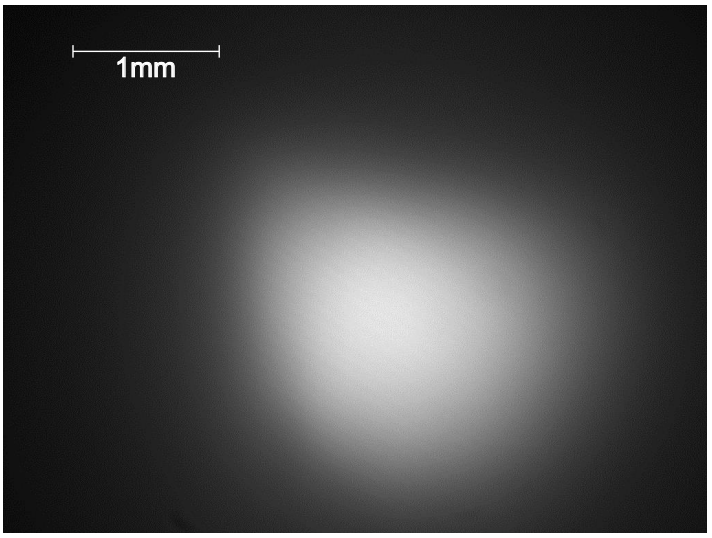

FIGURE 3.9: **CCD image of the trapped atoms**

The calibration was done by sending beams of well known powers on the CCD for various gains and exposure times. For a given gain value, $M_0 = P_{det} \cdot f_{CCD} \cdot t_{exp}$ with P_{det} the incident power on the detector, f_{CCD} the calibration factor and t_{exp} the exposure time. This allows to calculate the number of atoms N_{atoms} corresponding to a given image by expressing P_{det} as a function of N_{atoms}. The power of the light detected on the CCD is

$$P_{det} = P_{atoms} \cdot \Omega_{det} \cdot \eta_{det} \tag{3.15}$$

where η_{det} is the detection efficiency, accounting for losses on the path between the atoms and the CCD chip. P_{atoms} is the power emitted by the atoms, and Ω_{det} is the fraction of the detection solid angle. It corresponds to the cone delimited by the imaging lens of diameter d_l at a distance $2f$ from the atoms, with apex angle 2α.

$$\Omega_{det} = \frac{2\pi(1-\cos(\alpha))}{4\pi} \approx \frac{\alpha^2}{4} \approx \frac{1}{16}\frac{d_l^2}{4f^2}. \tag{3.16}$$

P_{atoms} is equal to the scattering rate R multiplied by the energy of a photon $\hbar\omega_p$. R is the number of atoms in the excited state N_e multiplied by the

linewidth of the transition Γ.

$$N_e = N_{atoms}\frac{1}{2}\frac{s}{1+s+\left(\frac{\Delta}{2\Gamma}\right)^2} \tag{3.17}$$

where Δ is the detuning of the light from the atomic resonance and $s = \frac{I}{I_s}$ is the saturation parameter with I_s the saturation intensity and $I = \frac{2\cdot 6\cdot P_{beam}}{\pi w^2}$, where P_{beam} and w are the power and waist of each individual cooling beam. Finally, we obtain

$$M_0 = N_{atoms}\frac{1}{2}\frac{s}{1+s+\left(\frac{\Delta}{2\Gamma}\right)^2}\cdot\Gamma\cdot\hbar\omega_p\cdot\Omega_{det}\cdot\eta_{det}\cdot f_{CCD}\cdot t_{exp}. \tag{3.18}$$

From the previous equation we extract

$$N_{atoms} = \frac{2\left(1+s+\left(\frac{\Delta}{2\Gamma}\right)^2\right)}{s\cdot\Gamma\cdot\hbar\omega_p\cdot\Omega_{det}\cdot\eta_{det}\cdot f_{CCD}\cdot t_{exp}}. \tag{3.19}$$

According to this calculation, we typically achieved values of several times 10^8 atoms trapped in our MOT. Referring to eq. (B.10), the radiation pressure force applied to the trapped atoms depends on the Rabi frequency and detuning of the cooling beam, and on the strength of the magnetic field gradient. In Fig. 3.10, we show the dependency of the trapped number of atoms as a function of the cooling beam detuning Δ_{Trap} and the MOT coils current I_{coils}, proportional to the magnetic field gradient strength. We observe an optimal magnetic field gradient, whose value remains fairly constant. If the available power is sufficient, a larger detuning allows to trap more atoms. However, the temperature of the cloud also increases with the detuning, which will reduce the memory lifetime in the DLCZ experiments.

3.7.2 Optical depth measurement

The optical depth is a measure of the opacity of a medium. It is an important parameter for our experiments, since the maximum achievable

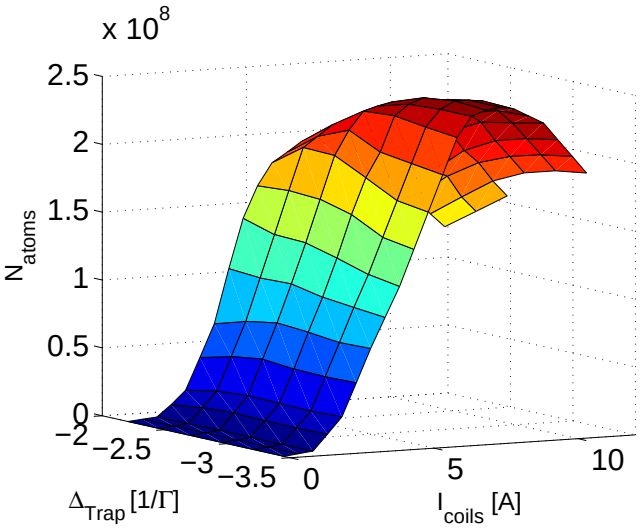

FIGURE 3.10: **Number of atoms in the MOT measured with CCD camera**

retrieval efficiency in DLCZ-type experiments strongly depends on it, as previously seen in chapter 2. The OD depends on the number of atoms within a probing volume of the atomic cloud. It is calculated from the normalized transmission T_{norm} as

$$\mathrm{OD} = -\ln(T_{norm}) = -\ln(I/I_0), \tag{3.20}$$

where I_0 is the intensity of the light incident on the medium and I is the intensity after passing through it. However, its value depends of the frequency of the light due to the linewidth of the atomic transitions. We measure I by sending single-photon level probe light with a frequency chirp on the atomic cloud, and detecting the transmitted light with a SPD. I_0 is measured in a similar way in the absence of atoms in the MOT, as shown inf Fig. 3.11. The data are taken for the $|F = 1\rangle \rightarrow |F' = 2\rangle$ transition, with linearly polarized light.

The normalized transmission calculated from this data is shown in Fig. 3.12 (a). In the case of an atomic cloud, the OD follows a Lorentzian profile in

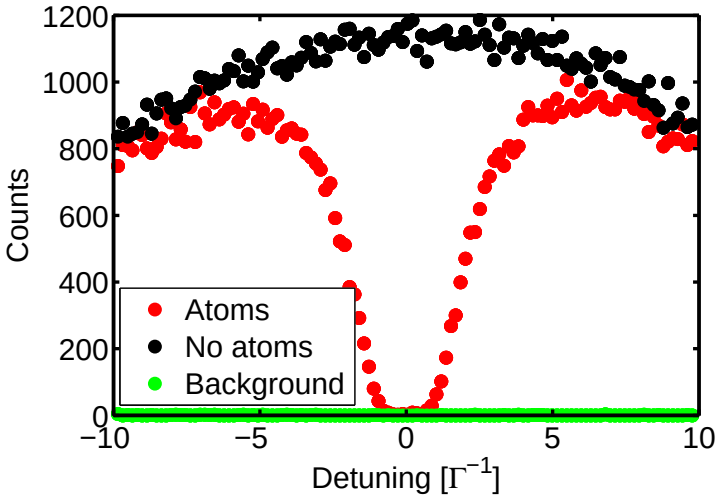

FIGURE 3.11: **Transmission of light through the atomic cloud.** The transmission of light is measured with (red data) and without (black data) atoms, as a function of the detuning expressed as multiples of the atomic transition's linewidth Γ. The background noise is in green.

frequency and its expression becomes

$$\mathrm{OD}(\omega) = \frac{\mathrm{OD}_{res}}{1 + 4\left(\frac{\omega - \omega_{res}}{\Gamma}\right)^2}, \tag{3.21}$$

where OD_{res} is the maximum value on resonance, and Γ is the natural linewidth of the transition centered on the angular frequency ω_{res}. The value of Γ is taken from [160]. The corresponding measurement for the OD is shown in Fig. 3.12 (b), with a maximum value on resonance of 15.3. The data are fitted with eq. (3.20).

Note that the maximum measured OD from the data is limited to ~ 4.5. This is because of the limited dynamic range of the SPD. Thus, the fit is performed considering only the values lower than a threshold of 4, and the rest of the points are not shown here.

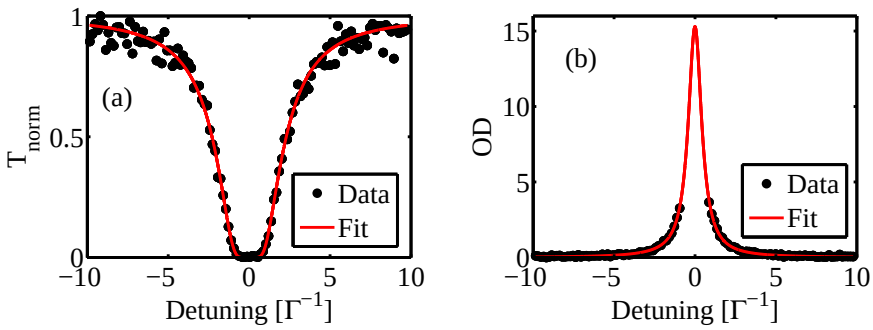

FIGURE 3.12: **Normalized transmission and optical depth.** (a) Normalized transmission of light through the atomic cloud. (b) Optical depth measurement. The data are shown in black and plotted as a function of the detuning in units of the natural linewidth. The red lines correspond to a fit according to eq. (3.20).

Chapter 4

Characterization of the DLCZ Quantum Memory

This chapter is divided into two parts. In the first one, I will explain how we implemented the DLCZ QM experiment in our lab. In the second part, I will show experimental data of various measurements performed in order to characterize our DLCZ quantum memory.

4.1 Implementation of the DLCZ protocol

In Fig. 4.1, I remind the energy levels structure of ^{87}Rb. We consider a 3-levels lambda-type structure, with an initial ground state $|g\rangle$, an excite state $|e\rangle$ and a storage state $|s\rangle$. Depending on the experiment, the ground and storage states were either a degenerate hyperfine level, or a specific Zeeman sub-level.

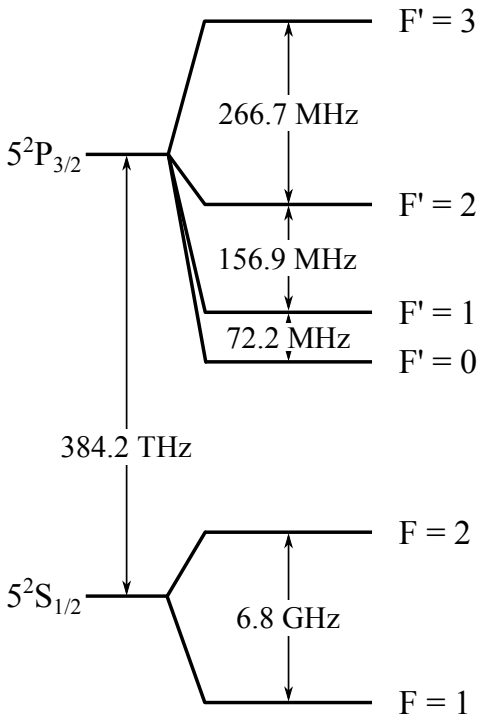

FIGURE 4.1: **Rubidium 87 D_2 line energy levels.**

4.1.1 Alignment of the setup

The alignment of the setup is a crucial point of our experiment (see Fig. 3.2 for a general view). It can be decomposed into two distinct parts. First, the alignment of the MOT beams, and second the alignment of the probe beams. The MOT beams are the cooling and repumping beams. The probe beams comprise the write/read beams arm through which pulses are sent, and the write/read photonic mode arm used to collect the generated photons.

4.1.1.1 MOT beams alignment

In order to align the MOT beams, we mainly rely on fluorescence imaging of the atomic cloud with a CCD camera. We start by a geometrical alignment of the cooling beams. An iris is placed after the initial fiber out-coupler in order to obtain smaller beams. This initial beam is then split into three other beams by means of PBSs and half-wave plates. We ensure that they intersect at the geometrical center of the science chamber, which also corresponds to the zero-crossing region of the magnetic field gradient. For this, we use an infrared viewer which allows us to see the beams on the surface of the chamber via the weak reflections, and inside of the chamber due to scattering in the presence of the atoms. The counter-propagating beams are then overlapped using the same method. The repumping beam alignment being much less critical, it is shone and back-reflected in only one direction, but still intersecting with the cooling beams. The alignment is then fine-tuned by optimizing the fluorescence with the CCD camera.

4.1.1.2 Probe beams alignment

We use four probe beams in total. One pair forms the write/read beams arm, and the second one forms the write/read photonic mode arm. Since we do not use a fully collinear configuration for the write/read beams

and photons arms, we have to ensure that they overlap precisely with each-other at the center of the atomic cloud by other means than simple geometrical alignment. We first align the write/read beams arm on the center of the cloud looking at the CCD image, thanks to the visible effect of the focused beams on the atoms when sent in continuous and on resonance. We then intersect the write/read photons arm with the write/read beams arm. In order to do this precisely, we load atoms in the MOT and optically pump them in one hyperfine level with light from the write/read beams arm. A weak probe light resonant with a transition involving the populated level is then sent through the photons arm. The best overlap corresponds to maximal absorption of the probe. The second fiber couplers of each arm are then collinearly aligned by optimizing the fiber coupling, which maximizes the mode overlap between the beams.

This method allows us to have a good overlap between the two arms, ensuring that they are passing near the center of the cloud. However, it does not ensure that the beams intersect precisely at the zero-crossing of the magnetic field gradient, since the shape of the cloud can deviate from a sphere whose center is this zero-crossing. This did not cause any problem in the data presented in this chapter, neither in the data of the QFC experiment presented in chapter 5. However, this proved to be important for the experiment of chapter 6. In this case, we used a more elaborate method, implementing a magnetic-field sensitive Raman memory, as explained in section 4.1.4.

4.1.2 Sequencing

The experimental sequence used to implement the DLCZ protocol is realized with the sequencer from Signadyne. All the parameters such as beams powers and frequencies are initialized and can then be accessed and modified while the experiment is running.

The first step is the loading of the atoms into the MOT, followed by an optional optical molasses period and then optical pumping. The optical molasses was not used in all the presented data, because it lowers the optical density of the atomic cloud, reducing the possible retrieval efficiency at short storage times. Optical pumping serves to initially prepare the atoms in $|g\rangle$. For the experiment presented in chapter 5, we initially prepared the atoms in the ground state $|g\rangle \equiv |F = 1\rangle$ and the Zeeman levels were degenerate, while for the experiment presented in chapter 6, we optically pumped the atoms in the specific Zeeman sub-level $|g\rangle \equiv |F = 2, m_F = +2\rangle$. Several parameters have to be considered in order to simultaneously achieve a low-temperature cloud allowing for long storage times and a high optical density allowing high retrieval efficiency. The cooling beams power and frequency must be optimized in order to achieve a MOT with a good compromise between atoms number and temperature. The duration of the trapping period, typically between 15 and 20 ms, must be short enough in order to allow an acceptable repetition rate, but long enough to trap as many atoms as possible. After switching off the MOT beams and magnetic field gradient, we wait for a short time ($\sim 300\,\mu$s) to allow the induced spurious magnetic fields to dissipate.

The second step is the realization of the measurement per se. We typically send a series of write pulses followed by a cleaning stage in order to empty the $|s\rangle$ state of atoms transferred by these pulses. The detection of a write photons triggers the read pulse. This is repeated during a predefined interrogation time T_{int}. We typically limit this time to about 1 ms, to avoid a significant decrease in optical depth due to free-fall of the atoms and thermal expansion of the cloud, which would limit the photons rates and retrieval efficiency.

The SPDs are connected to the TDC module, allowing us to perform coincidences measurements between the write and read photons.

4.1.3 Homogeneous magnetic field compensation

For some measurements, it was necessary to cancel the homogeneous magnetic field. One method to do so is to perform a spectroscopy of the Zeeman sub-levels. Since the natural linewidth of the used transitions is much bigger than the typical Zeeman splitting obtained with low magnetic fields of the order of a few Gauss, it is necessary to perform a so-called micro-wave spectroscopy. The idea is to initially prepare the atoms in $|F = 2\rangle$, so that they are transparent to a probe resonant with the $|F = 1\rangle \rightarrow |F' = 2\rangle$ transition. Then, micro-wave pulses with frequencies near the $|F = 1\rangle \rightarrow |F = 2\rangle$ ground state resonance are sent on the atoms. The frequency is incremented for each pulse, and the probe light is sent. When the micro-wave frequency matches a resonance between two Zeeman sub-levels, atoms are transferred to the $|F = 1\rangle$ state, and the probe is absorbed. There are seven possible resonance frequencies, giving rise to seven separated absorption lines in the spectroscopy traces, whose splitting is 700 kHz/G, given by the Landé-g factor. An example is shown in Fig. 4.2.

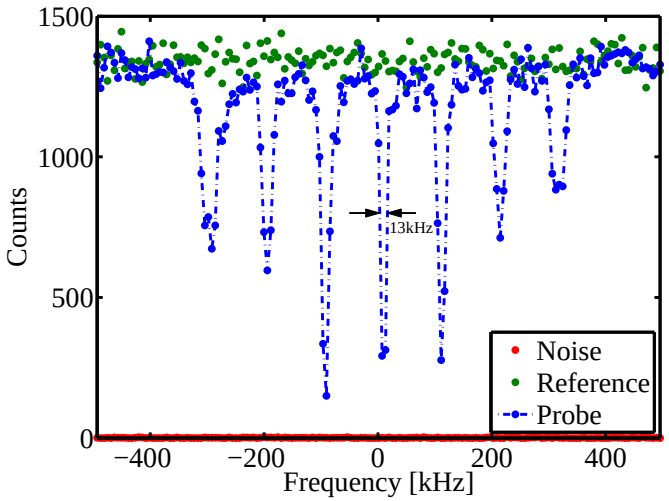

FIGURE 4.2: **Microwave spectroscopy of the ground states.** Red: Detector noise. Green: Reference signal without atoms. Blue: signal with atoms in the presence of a 140 mG homogeneous magnetic field.

The splitting in this case is $\sim 100\,\text{kHz}$, corresponding to a magnetic field of $\sim 140\,\text{mG}$. The frequency step is 6 kHz, and the microwave pulses duration is $\sim 100\,\mu\text{s}$, limiting the frequency resolution to about 10 kHz. Taking several of these measurements at different times of flight (TOF), we can measure the temporal variation of the homogeneous magnetic field induced by the switching of the MOT coils as shown in Fig. 4.3.

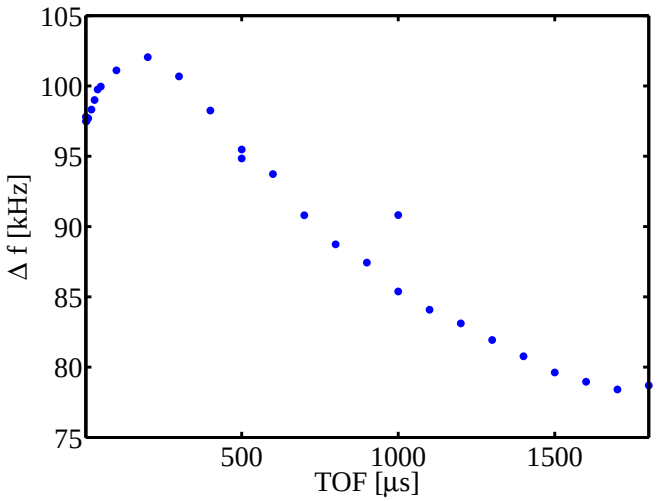

FIGURE 4.3: **Homogeneous magnetic field fluctuation after switching off the MOT coils.**

Adjusting the current in the compensation coils to reduce this splitting allows us to precisely compensate any kind of moderate homogeneous magnetic field at a given time. We usually compensate this field at a time centered on the interrogation time in our experiments. The result of such a procedure is shown in Fig. 4.4. The width of the absorption spectrum is $\sim 24\,\text{kHz}$, with a resonant OD ~ 2.4. Since there are seven absorption lines each separated by 700 kHz/G, the total splitting between the two outer peaks is 4.2 MHz/G. The maximum corresponding magnetic field is then $B_{Null} \approx \frac{24}{4200} = 5.7\text{mG}$. This method allows us to stabilize the magnetic field at the milligauss level.

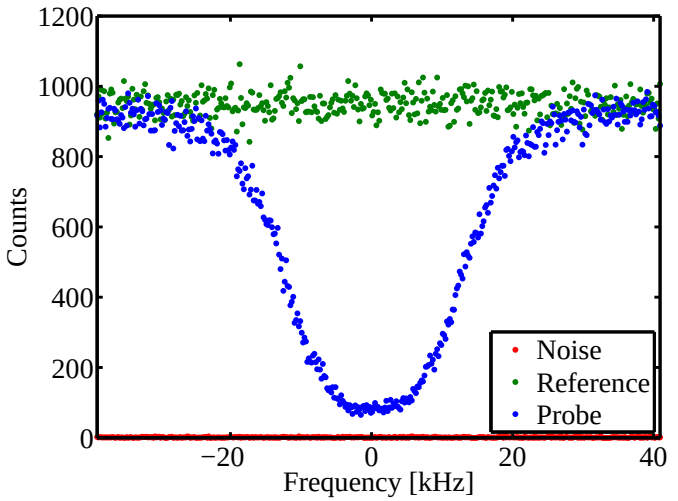

FIGURE 4.4: **Homogeneous magnetic field compensation.** Red: Detector noise. Green: Reference signal without atoms. Blue: signal with atoms when the homogeneous magnetic field is compensated.

To perform these measurements, we built a radio-frequency (RF) source, which is represented in Fig. 4.5. The initial 10 MHz source is provided by a fixed reference channel from an analog card of the control system from Signadyne. The first phase-locked loop (PLL) stage is an evaluation board from Analog Devices (model AD9522/PCBZ) with a stabilized output frequency at 205 MHz. The second stage is a high frequency PLL synthesizer from Analog Devices (model EVAL-ADF4007EB1) with an output frequency of $6.56GHz$. This signal is mixed with a variable frequency around 274 MHz provided by an analogical channel of Hydra, in order to match the ground-states resonance and be able to tune the final frequency.

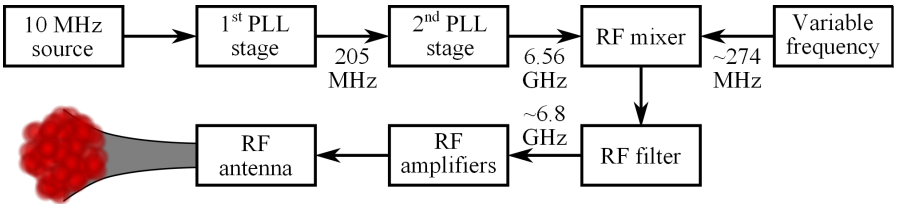

FIGURE 4.5: **Micro-wave source schematic.** PLL: phase-locked loop. RF: radio-frequency.

The mixed signal is then filtered in order to remove any side-band and leakage, before being amplified by a series of preamplifiers followed by a $3W$ amplifier (model ZVE-3W-83+ from Mini-Circuits). Finally, we use a dipole antenna to bring the RF signal to the atoms.

4.1.4 Raman memory

We also used a Raman memory protocol with classical light in order to optimize the magnetic field and the alignment of the beams for the DLCZ experiment. We initially prepare the atoms in $|F = 1\rangle$. The input probe light, red-detuned from the $|F = 1\rangle \rightarrow |F' = 2\rangle$ transition by 40 MHz is sent through the write/read photons arm, and the control beam, red-detuned from the $|F = 2\rangle \rightarrow |F' = 2\rangle$ transition by 40 MHz, is sent through the write/read beams arm. The output probe is detected with an avalanche photodiode (APD), and the FFC are not used because the noise level from the control beam leakage was lower than the electronic background noise from the APD. A typical measurement is shown in Fig. 4.6, with a total storage plus retrieval efficiency of 21%. Here, the duration of the probe pulse is about 50 ns, while the control pulse was switched on in advance, and switched off together with the probe pulse. The peak power is $\sim 5\,\mu$W for the probe and ~ 1 mW for the control. Since with this memory protocol, the probe is converted into an atomic coherence, it can also be used in order to determine the magnetic field on the atoms. As in the case of the DLCZ, an homogeneous field will generate periodic dephasing and rephasing of the stored state visible when measuring the retrieval efficiency as a function of the storage time. The small bump in the retrieved pulse is due to the remaining presence of spurious magnetic fields.This method can sometimes be an interesting alternative to the micro-wave spectroscopy.

We also implemented the Raman GEM protocol. The magnetic field gradient of the MOT coils is kept on during the writing process, before being reversed at a later time. Very similarly to the case of the controlled rephasing in the DLCZ experiment which will be presented in chapter 6, this field

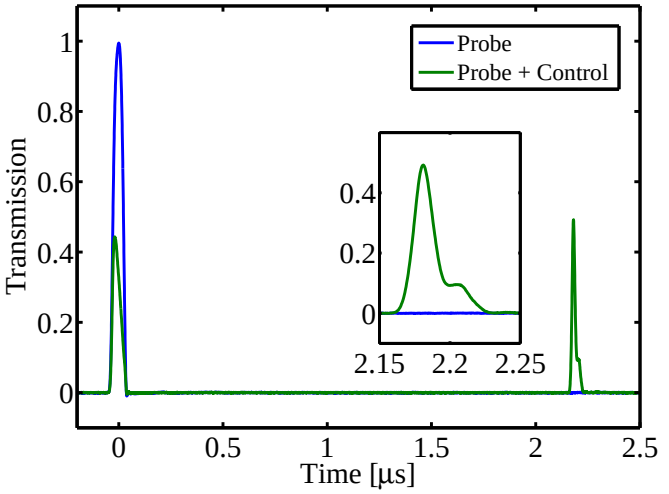

FIGURE 4.6: **Classical Raman memory.** Normalized transmission of the probe alone (blue) and with the control pulse during writing and readout (green). The inset shows the retrieved probe.

reversal induces a rephasing at a given time. Sending the control pulse at that time allows to retrieve the stored input probe light efficiently. We observed that depending on the alignment of the beams on the atomic cloud, sometimes several "side rephasings" were appearing. This is expected when the beams do not intersect at the position of the magnetic field gradient's zero-crossing, but are slightly shifted. In this case, an extra time-dependent offset component appears in the magnetic term of the phase describing the atomic state. Since this offset is proportional to the magnetic field gradient amplitude and sign, it varies during the storage time when the gradient is reversed. This phenomenon is shown in Fig. 4.7, together with a model based on the formula given in (6.14), adding an extra phase term corresponding to the temporally varying magnetic field offset accounting for the off-axis alignment.

This observation allowed us to precisely align the beams at the zero-crossing of the magnetic field gradient (see Fig. 4.7, right plot).

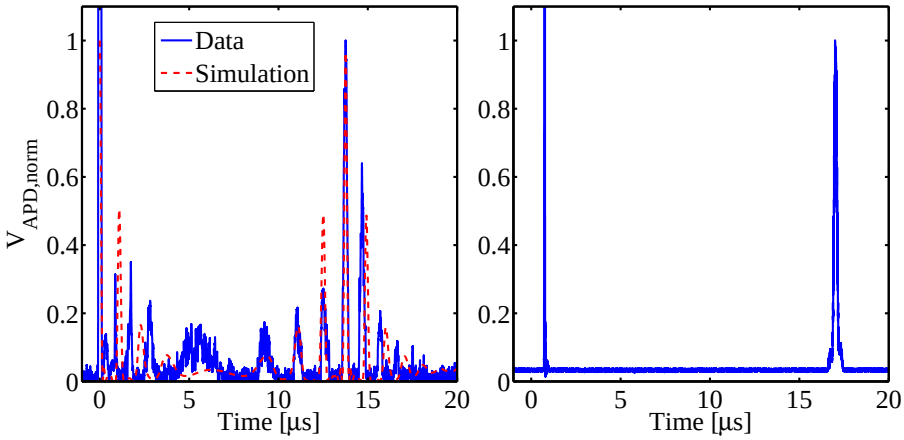

FIGURE 4.7: **Raman GEM protocol with off-axis alignment.** (Left plot) Temporal evolution of the normalized phase when the probe and control beams do not intersect with the zero-crossing of the magnetic field gradient in the radial direction of the coils. (Solid blue line) Signal on the avalanche photodiode. (Dashed red line) Simulation of this configuration. (Right plot) Example of a similar trace after optimization of the alignment.

4.2 Characterization of the DLCZ quantum memory

In this section, I will show experimental data characterizing our DLCZ QM, as introduced in section 2.1.5. I will first shows a measurement of the second order cross-correlation function $g^{(2)}_{w,r}$, together with the retrieval efficiency from the same set of data. I will then show data illustrating the memory lifetime, and demonstrate how this can be used in some cases to estimate the spin-wave distribution among several Zeeman sub-levels of non-degenerate hyperfine ground states.

4.2.1 Second-order cross-correlation function and retrieval efficiency

For the data presented in this section, the atoms were initially prepared in the ground state $|g\rangle \equiv |F = 1\rangle$, with $|s\rangle \equiv |F = 2\rangle$ and $|e\rangle \equiv |F' = 2\rangle$.

As explained previously in section 2.1.5, the value of $g^{(2)}_{w,r}$ depends on the spin-wave creation probability p. In Fig. 4.8, I show a typical histogram used to infer the $g^{(2)}_{w,r}$. The write photon detection probability was 0.07% corresponding to $p = 1.54\%$, 20×10^3 MOTs were loaded at a rate of 50 Hz and 1000 write pulses were sent each time for a total interrogation time of 1.4 ms.

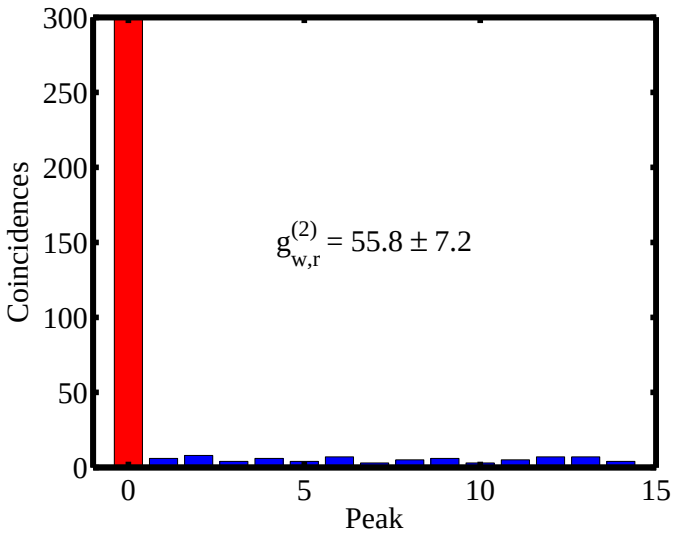

FIGURE 4.8: $g^{(2)}_{w,r}$ **histogram.** Red: Coincidences from correlated photons. Blue: Accidental coincidences. A total of 2×10^7 write pulses were sent with $p = 1.54\%$.

This histogram is constructed from a start-stop measurement with a write photon detection as a start and read photon detection as a stop. The first bar in red corresponds to the coincidences between a write photon and a correlated read photon created by the readout of the memory in the same trial. The remaining blue bars correspond to accidental coincidences between a write photon, and a read photon in a different subsequent trial. Those can originate from noise, or read photons correlated with undetected write photons, but these events are not correlated with the detected write photons. The coincidence probability is then the product of the photons detection probabilities of each detector. As a consequence, the value of

$g^{(2)}_{w,r}$ is equal to the ratio of the number of correlated coincidences and the average number of accidental coincidences.

In Fig. 4.9, I show $g^{(2)}_{w,r}$ plotted as a function of the write photon detection probability p_w, with a log-log scale. The star data point corresponds to the histogram shown in Fig. 4.8. The values of $g^{(2)}_{w,r}$ are calculated with

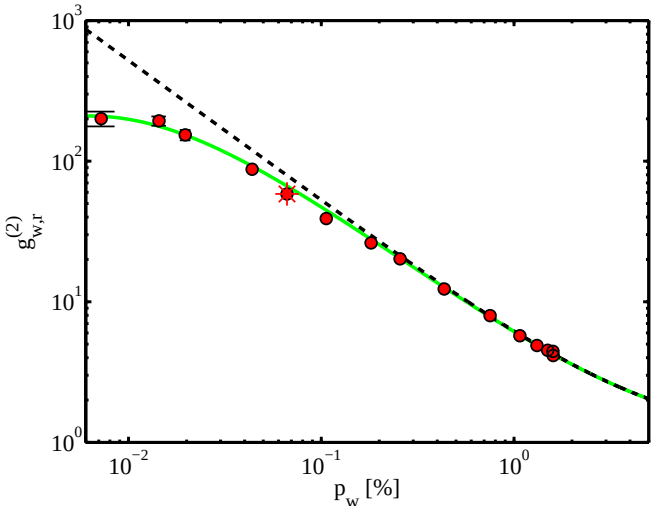

FIGURE 4.9: $g^{(2)}_{w,r}$ **as a function of** p_w**.** Red points: Measured values. Green solid line: Fit of the experimental data, considering noise contribution. Black dashed line: Asymptotic value without noise.

the formula

$$g^{(2)}_{w,r} = \frac{p_{w,r}}{p_w \cdot p_r}, \tag{4.1}$$

where each probability is calculated as the total number of counts (or coincidences) divided by the number of write pulses. The dashed black line is a fit based on eq. (2.25), where we assume a proportional relation $p_w = \eta^{tot}_{trans} \cdot p$, such that the expression becomes

$$g^{(2)}_{w,r} = 1 + \frac{\eta^{tot}_{trans}}{p_w}. \tag{4.2}$$

It corresponds to the maximum value of $g^{(2)}_{w,r}$ achievable in a noiseless situation. The fit yields a value of 0.052 ± 0.003 for η^{tot}_{trans}. This is consistent

with the estimated transmission efficiency of the write photons $\eta_{t,w} = \eta_c \cdot \eta_{FFC} \cdot \eta_{fc} \cdot \eta_{det} = 0.065$, where $\eta_c \approx 0.6$ is the photons collection efficiency, $\eta_{FFC} \approx 0.5$ is the FFC transmission, $\eta_{fc} \approx 0.5$ is the subsequent fiber coupling efficiency, an $\eta_{det} = 0.43$ is the detection efficiency. However, this fit doesn't agree with the data for low values of p_w. This is because the noise contribution starts to be significant when the photons detection rates become lower. The solid green line is a fit where the noise contribution has been added. The formula used is

$$g^{(2)}_{w,r}(p_w) = 1 + \frac{p_w}{(p_w + a)(p_w + b)}, \tag{4.3}$$

where a, and b are coefficients accounting for noise counts in the write and read photons detectors [162]. For this fit, we consider equal contributions for a and b, and the calculated value is $p_N = 1.2 \times 10^{-3}$, corresponding to the probability to get a noise detection per write/read pulse. We observe a deviation from the ideal case when p_w becomes comparable with this value. Moreover, the finite retrieval efficiency is not taken into account for simplicity. Its effect in this formula would be a decrease of the calculated noise level.

In Fig. 4.10, I show the retrieval efficiency η_{ret} in the optical fiber after collection of the read photons, calculated as

$$\eta_{ret} = \zeta \cdot \frac{p_{w,r}}{p_w}, \tag{4.4}$$

where ζ accounts for the transmission and detection efficiencies, but not the photons collection efficiency from the atomic ensemble to the first single mode fiber. In the central part, where the dark counts are negligible and the higher order excitations don't artificially increase the measured value, we find $\eta_{ret} \approx 24\%$. Assuming that the photons' collection efficiency equals the classical coupling of $\approx 55\%$, this corresponds to an intrinsic retrieval efficiency inside the chamber of $\approx 44\%$. Another figure showing this behavior is presented in chapter 5 (Fig. 5.12) with a higher retrieval efficiency but lower values for $g^{(2)}_{w,r}$, because in that case the filter cavity

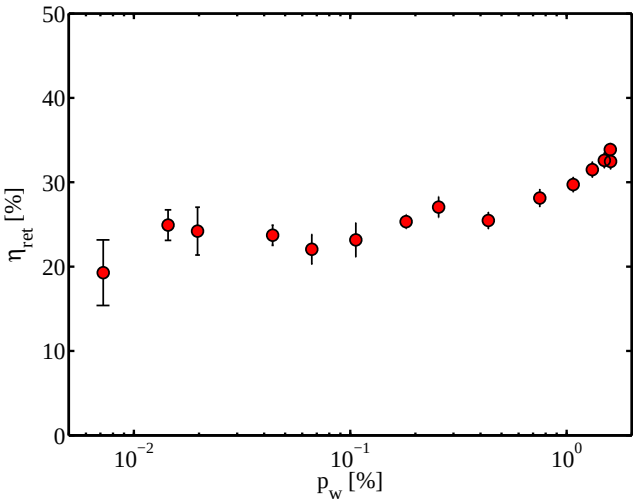

FIGURE 4.10: **Retrieval efficiency as a function of p_w.**

for the read photons was not present in the setup due to the connection with the QFCD.

4.2.2 Memory lifetime

In this section, I will show data on the memory lifetime of our QM for two different configurations. The first one with no optical pumping corresponds to the quantum frequency conversion experiment presented in chapter 5, and the second case with optical pumping corresponds to the controlled rephasing experiment presented in chapter 6

No optical pumping

Here, the atoms were initially prepared in $|F = 1\rangle$, with no optical pumping in a specific Zeeman sub-level, and the homogeneous magnetic field was nulled. The write and read beams were linearly polarized with orthogonal polarizations, and there was a 3° angle between the write/read pulses and photons detection modes. The temporal evolution of the $g^{(2)}_{w,r}$ as a function of the storage time is shown in Fig. 4.11. We did not attempt to optimize

the memory time for this data, because at this point we operated the system at short storage times, as for the QFC experiment. We find a $1/e$ memory time $\sim 15\,\mu$s.

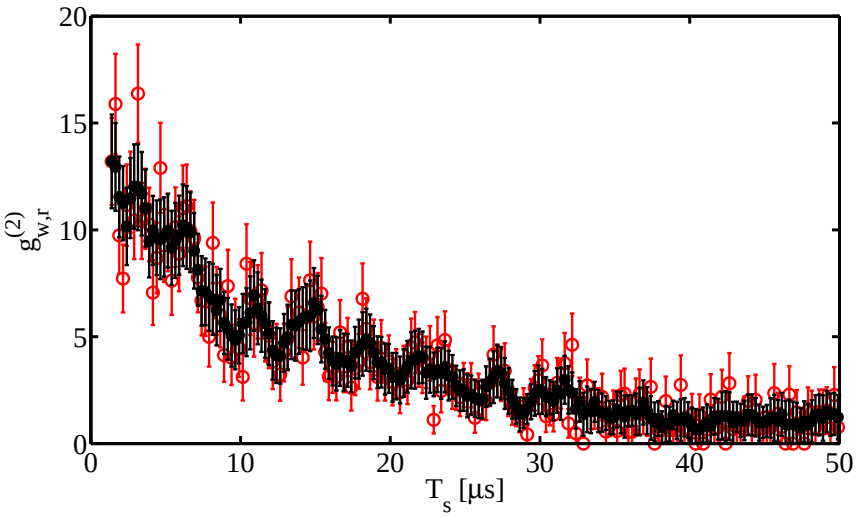

FIGURE 4.11: $g^{(2)}_{w,r}$ **as a function of storage time, without optical pumping.** Red circles: experimental data. Black dots: moving average of 5 points to reduce the effects of experimental fluctuations. The $1/e$ memory time for this data is $\sim 15\,\mu$s.

Optical pumping in a Zeeman sub-level

Here, the atoms are initially optically pumped in $|F = 2, m_F = 2\rangle$, and the polarization of the write and read beams is respectively σ^- and σ^+. The polarization of the detected write and read photons is respectively σ^+ and σ^-. Like this, only one spin-wave can be defined, between the $|F = 2, m_F = 2\rangle$ and $|F = 1, m_F = 0\rangle$ states. The reason for this choice is to enable a controlled broadening of the spin transition with a magnetic field gradient, as was used for the experiments presented in chapter 6. The angle between the write/read pulses and photons detection modes was 0.95°. Here, a 1.6 ms optical molasses was applied to reduce the temperature of the cloud and increase the memory time. The measured retrieval efficiency η_{ret}^{meas} with the associated read photon detection

probability p_r, together with the $g^{(2)}_{w,r}$ as a function of the storage time are shown in Fig. 4.12. From the graphs, it is clear that the decay for the $g^{(2)}_{w,r}$

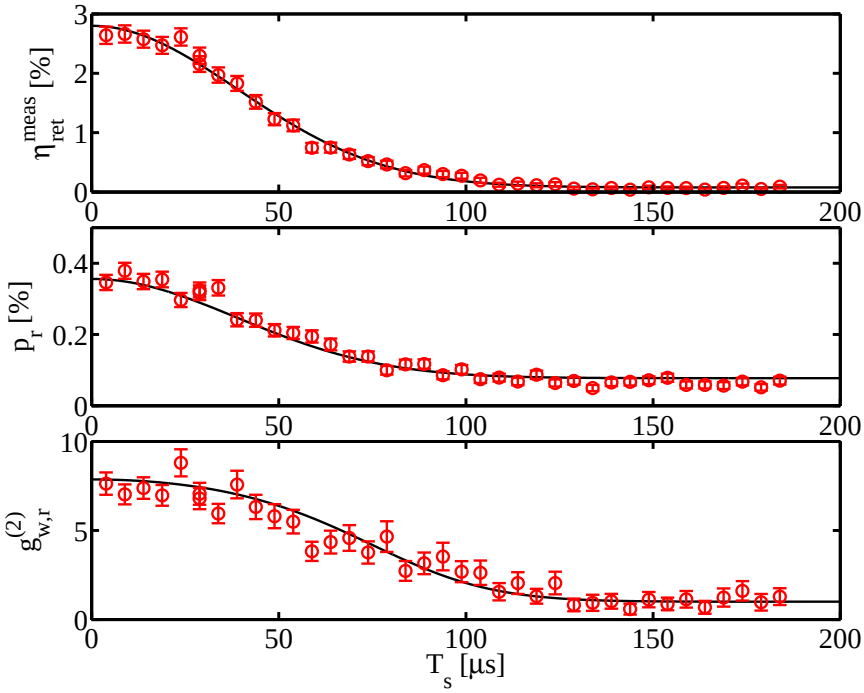

FIGURE 4.12: **Retrieval efficiency, p_r and $g^{(2)}_{w,r}$ as a function of storage time, with optical pumping.** Red circles: experimental data. The retrieval efficiency is the measured and uncorrected value. Solid black lines: fits using equations (4.5) and (4.6).

happens on a longer timescale as in the case of η_{ret} and p_r. This can be modeled according to [162] as shown by the fitted black lines. The relevant probabilities are defined as

$$p_w = p \cdot \eta_t^w, \tag{4.5a}$$

$$p_r = (p \cdot \gamma + p_{r,N}) \cdot \eta_t^r, \tag{4.5b}$$

$$p_{w,r} = p \cdot \gamma \cdot \eta_t^w \cdot \eta_t^r + p_w \cdot p_r, \tag{4.5c}$$

where p is the probability to create at least one write photon, $\eta_t^{w,r}$ are the combined transmission and detection efficiencies for the write (resp.) read photons, $p_{r,N}$ is the noise probability in the read channel (its counterpart

for the write channel is neglected here for simplicity), and $\gamma = \gamma_0 e^{-t^2/\tau^2}$ is the decay of the retrieval efficiency with γ_0 the intrinsic retrieval efficiency, and τ the $1/e$ time constant given by any dephasing mechanism. From these equations, the calculated expressions for Fig. 4.12 are

$$\eta_{ret} = \frac{p_{w,r}}{p_w} = [\gamma \cdot (1+p) + p_{r,N}] \cdot \eta_t^r, \tag{4.6a}$$

$$g^{(2)}_{w,r} = \frac{p_{w,r}}{p_w p_r} = 1 + \frac{\gamma}{p \cdot \gamma + p_{r,N}}. \tag{4.6b}$$

Note that eq. (4.6b) is consistent with the expression calculated from the two-mode squeezed state in eq. (2.25), the two being equal in the absence of the noise term $p_{r,N}$. The values of p and η_t^r are known from the measurement and the setup characterization. A fit of the retrieval efficiency is used to calculate the values of γ_0, τ, and $p_{r,N}$, which are then used in the expressions of (4.5b) and (4.6b) in order to produce the green lines of Fig. 4.12 (b) and (c) respectively. We observe a good agreement between this model and our data. The fit yields values of 47% for the intrinsic retrieval efficiency, and a memory lifetime of 55 μs. This memory lifetime is principally limited by two dephasing mechanisms. One is due to spurious magnetic field gradients, and the other to the finite temperature of the atomic cloud. Considering only atomic motion, as explained in section 2.1.4, the corresponding temperature would be $\sim 180\,\mu$K, which gives a higher bound for the actual value achieved in our MOT. Note however that this configuration maximizes the sensitivity to spurious magnetic fields, such that it is likely that a significant part of the dephasing is due to that reason.

4.2.3 Collapse and revival of spin-waves

In this section, I will show experimental data illustrating the oscillatory behavior of the retrieval efficiency over time described in section 2.1.4. The configuration here is similar to the one with no optical pumping described above, except that here an homogeneous magnetic field was applied in a random direction. This led to periodic de- and rephasings of the spin-waves

over time as shown in Fig. 4.13. The oscillatory behavior of the retrieval efficiency over time described in section 2.1.4 was observed, and is shown in Fig. 4.13. The data are fitted with eq. (2.19). The displayed efficiency

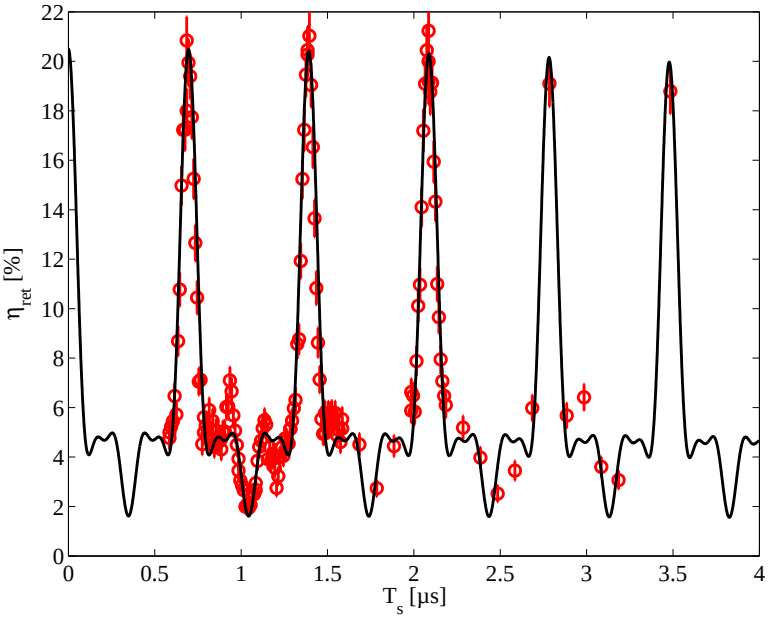

FIGURE 4.13: **Retrieval efficiency as a function of storage time in the presence of an homogeneous magnetic field.** Red circles: experimental data. Solid black line: fit.

is only corrected for the detection efficiency. For this measurement the FFC were not present in the setup. A magnetic field of $\sim 2G$ was applied, in a non-specific orientation, such that there were no precise quantization axis, and processes corresponding to several different polarizations could happen.

Chapter 5

Quantum Frequency Conversion compatible with Quantum Memories

In this chapter, I will present our experimental results on Quantum Frequency Conversion compatible with atomic Quantum Memories. It will be based on the two following papers: [121] and [26]. The first paper, described in section 5.1, presents our experimental results on the QFC of weak coherent states (WCSs) at frequencies resonant with ^{87}Rb from 780 nm to 1552 nm. It describes in detail the experimental setup and the methods employed for the characterization of the quantum frequency conversion device (QFCD). The second paper, presented in section 5.2, deals with the conversion of true heralded single photons emitted by the DLCZ QM and demonstrates our ability to perform this conversion while preserving the non-classical nature of the correlations between the photon pairs.

5.1 Quantum Frequency Conversion of weak coherent states

In this section, I will start by detailing the experimental setup, which was built by two master students of our group, Giacomo Corrielli and Xavier Fernandez-Gonzalvo. I will then present our experimental results taken from [121]. After the characterization of the input weak coherent states, I will present the performances of our QFCD as a function of the pump power and the frequency filtering bandwidth, showing its operation in the low noise regime. Finally, I will show results demonstrating the coherence preservation of this frequency conversion. My main contribution to this work has been the verification of the resonant nature of the converted light with the atomic ensemble, while the rest of the measurement have been realized mainly by Xavier Fernandez-Gonzalvo.

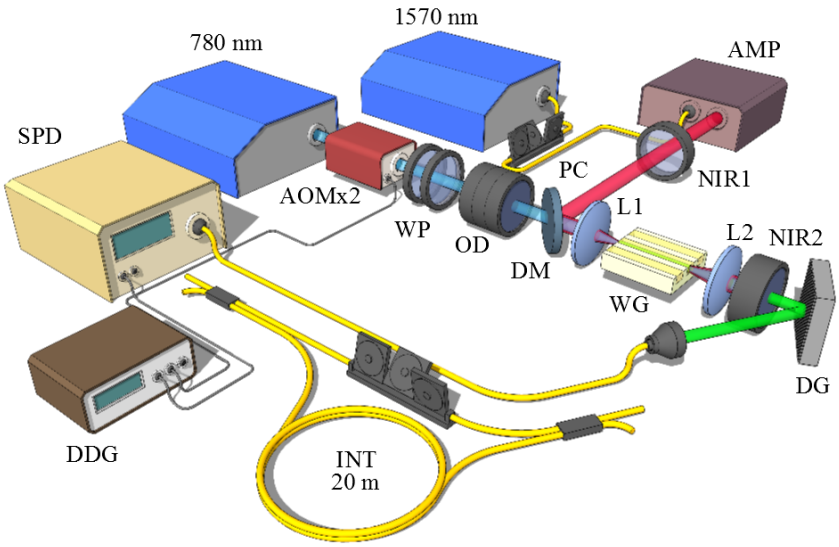

FIGURE 5.1: **Experimental setup for the QFCD** [121]**.** PC: polarization controller. AMP: fiber amplifier. NIR1: band-pass filter centered at 1569 nm. AOMx2: acousto-optic modulator in double passage. WP: half- and quarter- waveplates. OD: neutral density filters. DM: dichroic mirror. L1: in-coupling lens. WG: non-linear waveguide. L2: out-coupling lens. NIR2: band-pass filter centered at 1552 nm plus long-pass filter with cut-off at 1450 nm. DG: diffraction grating. SPD: single photon detector. DDG: digital delay generator. INT: fiber interferometer.

5.1.1 Experimental setup

The experimental setup for the QFC of weak coherent state is show in Fig. 5.1. It can be divided into 4 distinct parts: the laser sources, the waveguide, the filtering stage and the detection stage.

Laser sources

The input light for the weak coherent states is provided by the trap laser at 780.24 nm, resonant with the D_2 line of ^{87}Rb. The pulses are produced with an AOM in double-pass configuration. In this experiment,

they exhibit a FWHM duration of 30 ns. The AOM is controlled by a digital delay generator (DDG), generating pulses at a repetition rate of 1 MHz. The pulses are then attenuated by a set of neutral density filters with a measured OD of 16.6 ± 0.1. The mean input photon number per pulse is tuned between 0.3 and 25 by adjusting the laser power. The pump light used for the conversion is delivered by the telecom pump laser at 1569 nm described in section 3.2.4. The broad amplified spontaneous emission (ASE) background present at the target wavelength is suppressed by two bandpass filters centered at 1570 nm, with a 9 nm bandwidth. The ASE is suppressed by more than 100 dB at 1552 nm.

Waveguide

For this experiment, the conversion takes place in a 3 cm long periodically poled lithium niobate (PPLN) waveguide, anti-reflection coated for 780, 1552 and 1569 nm. The cross-section of the selected waveguide is $7.08 \times 11.35\,\mu\text{m}^2$, leading to multi (resp. single)-mode propagation of visible to near-IR (resp. telecom) wavelengths. The specified transmission losses are 0.7 dB/cm (resp. 0.35 dB/cm) at 780 nm (resp. $1552 - 1569$ nm). The waveguide is stabilized in temperature around $320°K$ with a Peltier element in order to achieve the quasi-phase matching condition. The input and pump lights are combined on a dichroic mirror after appropriate polarization control, before being coupled into the waveguide. The incoupling is realized by a 15.9 mm focal length and 0.16 numerical aperture lens, which is AR-coated for 780 nm. The outcoupling is realized by a similar lens, AR-coated for 1552 nm. It is important that the coatings of these lenses allow maximum transmission of the input and converted signal light. We estimate a similar incoupling efficiency for the pump and signal lights around 30%. However, due to the multi-mode propagation at the input signal wavelength, the maximum conversion efficiency does not necessary correspond to the maximum value for the incoupling of the signal.

Filtering stage

There are two main sources of noise with our configuration. First, leakage of the strong pump at 1569 nm, which could be detected by the telecom SPD. This light is blocked using two band-pass filters centered around 1552 nm with a bandwidth of 7 nm and a transmission of 93% at 1552 nm. Second, spontaneous Raman scattering of the pump light occurs on a broad wavelength range. Due to its broadband nature, the only way to suppress it is to apply a narrow frequency filtering around the frequency of the converted signal. A diffraction grating coupled to a single mode fiber is used for this purpose, allowing to have a transmission bandwidth $\Delta\lambda$ from 0.65 to 2.3 nm (or 80 to 287 GHz). In the following, we selected a value of 0.7 nm (85 GHz). In addition to this, there can be leakage of unconverted signal light at 780 nm, and SHG of the pump around 785 nm. This light is blocked using a long-pass filter with a cutoff frequency of 1450 nm, with a transmission of 85% at 1552 nm. The total transmission of the filtering stage at 1552 nm is about 26%, taking into account the transmission of the frequency filters, and the diffraction grating and fiber coupling efficiencies.

Detection

The converted light is sent to a telecom SPD (ID201, from ID Quantique) operated in gated mode with 10% detection efficiency, after a fiber connection with 70% efficiency. At this detection efficiency, the dark count rate is about 10 kHz. The dead time after a detection is set to 20 μs in order to avoid noise from after-pulses. This detector was usually used with two different gate times of 20 or 50 ns. The synchronization between the pulses and SPD gating was done with the DDG used to create the pulses.

5.1.2 Experiment results

5.1.2.1 Input pulses characterization

The input WCPs which we prepare are set to be resonant with an atomic transition, such that they can simulate real single photons emitted from our QM. They also exhibit a duration compatible with the photons obtained from such QMs.

Atom-resonant pulses

We first verify the interaction between the WCPs and the atomic ensemble prepared in a MOT. The frequency of the WCPs is scanned around the relevant atomic resonance. After interacting with the atoms, the pulses are sent to the QFCD and detected with the telecom SPD. We observe an absorption profile indicating that the light pulses effectively interact with the rubidium atoms, as shown in Fig. 5.2. The data are plotted as a function of Δf, the relative detuning of the pulses frequency with respect to the atomic resonance, spanned over approximately 110 MHz. The fit of the experimental data gives a FWHM of 16 ± 1 MHz for the absorption profile. This is comparable to the convolution between the natural linewidth of the atomic transition (6 MHz) and the bandwidth of the WCP of $0.44/(30\,\text{ns}) = 14.7$ MHz for Gaussian pulses.

Pulses shape after conversion

An important feature of the QFCD in order to achieve high fidelity is the ability to conserve the temporal shape of the input signal. For this, we prepare input pulses with a mean photon number of 5 and convert them. We center a 100 ns detection window around the center of the pulses arrival time. The trigger and the single photons detection times are recorded with a high resolution time stamping card (time resolution of 640 ps, from Signadyne). The photons shape is reconstructed via a start-stop measurement using the triggers as starts and photons detections as stop, as shown

in Fig. 5.3. The dark counts (green) are obtained by blocking the waveguide input. The noise (blue) is obtained by blocking the input signal, and also includes dark counts. The signal (red) includes noise and dark counts.

Since we use photons shorter than this 100 ns window, it would be detrimental in terms of SNR to use this value in typical experiments. This is why we selected two possible values for the detection gate ($\Delta t_G = 20$ or 50 ns) eligible with our detector. We define the probability to detect a signal count as $p_S = \frac{1}{N_p} \int_{\Delta t_G} s\mathrm{d}t$ where s is the complete signal temporal shape and N_p is the number of pulses. We define the noise (p_N) and dark counts (p_{DC}) detection probabilities in a similar way. This allows us to calculate the β parameter corresponding to the detected fraction of the signal as $\beta = (p_S - p_N)/(p_{S_\infty} - p_{N_\infty})$, with p_{S_∞} (p_{N_∞}) is the signal (noise) when $\Delta t_G \to \infty$. The signal-to-noise ratio with (without) dark counts subtraction is defined as $\mathrm{SNR} = (p_S - p_N)/(p_N - p_{DC})$ ($\mathrm{SNR_{DC}} = (p_S - p_N)/(p_N)$).

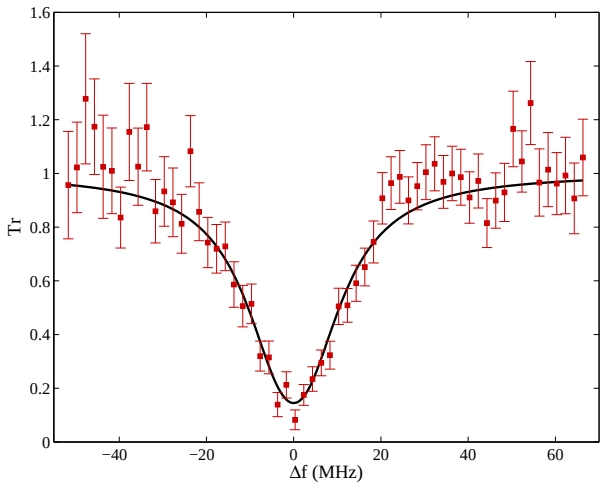

FIGURE 5.2: **Transmission of the weak coherent states through the atomic ensemble** [121]**.** Input pulses at 780 nm are converted to 1552 nm after interacting with the atoms. Red squares: experimental data plotted as a function of Δf, the relative detuning of the pulses frequency with respect to the atomic resonance. Solid line: Lorentzian fit of the data.

Using shorter values for Δt_G allows higher values for the SNR, at the expense of the β parameter, leading to a lower detection efficiency, and vice versa. This behavior is illustrated in the inset of Fig. 5.3. However, the reduced detection efficiency can be compensated in the calculations by knowing the value of β, and we define it as $\eta_{det} = 0.07 \times \beta$, including the detector efficiency and the fiber connection. The value of $\Delta t_G = 20\,\text{ns}$ leads to $\beta = 0.57$ with the highest SNR, while $\Delta t_G = 50\,\text{ns}$ leads to $\beta = 0.97$. In the following, we used a 20 ns detection window, unless otherwise specified. This corresponds to $\beta = 0.57$ and $\eta_{det} = 0.04$.

5.1.2.2 Behavior as a function of pump power

The main free parameter of our QFCD is the power of the pump used for the conversion. It will affect the noise level and the conversion efficiency, henceforth also the SNR.

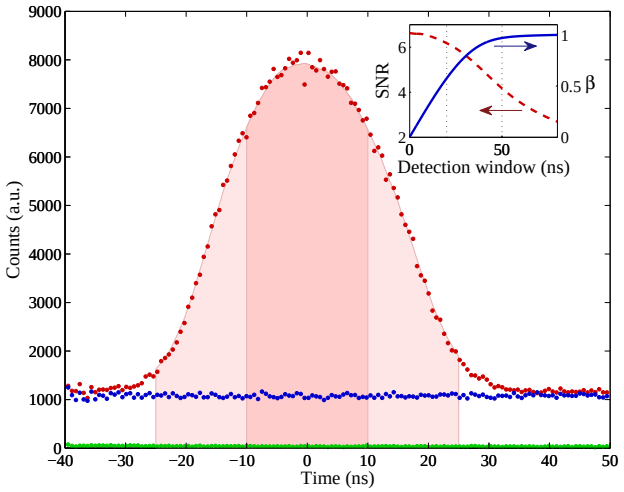

FIGURE 5.3: **Temporal profile of converted weak coherent states** [121]**.** Green: Dark counts. Blue: Pump noise. Red: Converted signal. Light-shaded area: 50 ns detection window. Dark-shaded area: 20 ns detection window. Inset: Signal-to-noise ratio (left axis) and β factor (right axis)

Pump noise

To measure the noise induced by the pump light, we block the signal input before the dichroic mirror. The noise level N varies linearly with the pump power P_p measured after the waveguide as

$$p_N(P_p) = \alpha \cdot P_p + p_{DC}. \tag{5.1}$$

Since the pump wavelength is larger than the output wavelength of the converted light, there is no spurious down-conversion from the pump [163]. No other non-linear processes could produce light at the output wavelength. This suggests that the origin of the detected noise is a combination of pump leakage and Raman noise, even though we didn't measure the noise spectrum to confirm this assumption. Fig. 5.4 (red squares) shows the measured noise detection probability p_N as a function of P_p. A fit with the formula of eq. (5.1) gives $\alpha \approx 6 \times 10^{-6}/\,\mathrm{mW}$ for the noise level of the detected events. This corresponds to $\alpha\prime \approx 10^{-4}/\,\mathrm{mW}$ at the output of the waveguide. Thanks to this simple relation, we can use the detected noise level in order to calculate the pump power at the output.

Conversion efficiency

To measure the conversion efficiency, we send WCPs with $\mu_{in} = 6.1$ and measure the probability to detect a photon p_S. The detection probabilities as a function of the pump power after the waveguide are shown in Fig. 5.4. The blue circle correspond to p_S, and the green triangles to $p_S - p_N$.

From this, we obtain the total efficiency $\eta_{tot} = (p_S - p_N)/\mu_{in}$. This quantity includes the conversion and detection efficiencies, as well as the losses. The maximum value for the total efficiency is $\eta_{tot}^M = 2.6 \times 10^{-3}$. We define the device efficiency η_{dev} as the total efficiency after correction accounting for the detection efficiency. This can be interpreted as the probability to obtain a converted photon in a single mode fiber at the output of the QFCD after the frequency filtering stage, when $\mu_{in} = 1$. We calculate $\eta_{dev}^M = 0.066$. We can then define the external conversion efficiency

$\eta_{ext} = \mu_{out}/\mu_{in}$, with μ_{out} the average number of photons per pulse at 1552 nm. η_{ext} is obtained by correcting η_{dev} for the transmission losses of the frequency filtering stage, giving a maximum value $\eta_{ext}^{M} = 0.25$. This value is limited by the incoupling of the signal to the waveguide $\eta_c = 0.61$. Finally, we obtain the internal conversion efficiency $\eta_{int} = \eta_{ext}/\eta_c$, with a maximum value of $\eta_{int}^{M} = 0.41$. In theory, this value should be 1. In practice, it is limited by the transmission of the waveguide, inferred to be $\eta_t = 0.7$ from the manufacturer's specifications, if the photons are created at the center of the waveguide. The remaining inefficiency can be due to imperfect mode matching between the pump (single-mode) and the signal (multi-mode), and variations in the poling period.

In Fig. 5.5, we can see the external conversion efficiency (red squares, left axis) and the signal-to-noise ratio (blue circles, right axis) as a function of the pump power.

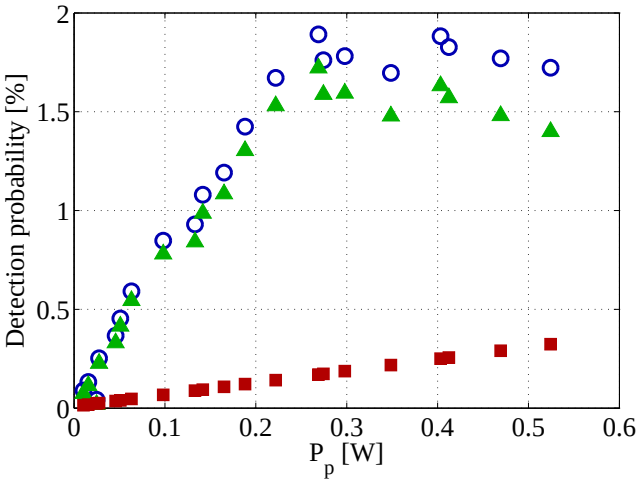

FIGURE 5.4: **Signal and noise detection probabilities after conversion** [121]**.** The data are plotted as a function of the pump power P_p measured after the waveguide. Red squares: noise. Blue circles: signal. Green triangles: Signal after noise subtraction.

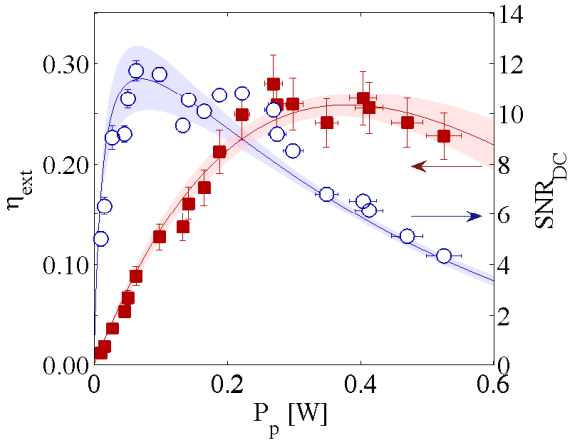

FIGURE 5.5: **External conversion efficiency and signal-to-noise ratio** [121]**.** The data are plotted as a function of the pump power P_p measured after the waveguide. Red squares, left axis: external conversion efficiency. Blue circles, right axis: signal-to-noise ratio, without dark counts subtraction. Solid lines: fits of the experimental data using Eqs. (5.2) and (5.3).

The data for η_{ext} are fitted with the formula

$$\eta_{ext} = \eta_{ext}^{M} \sin^2\left(L\sqrt{P_p \cdot \eta_n}\right), \tag{5.2}$$

where L is the length of the waveguide, and η_n is the normalized conversion efficiency. The free parameters for the fit are η_{ext}^{M} and η_n, leading to $\eta_n = 72 \pm 7\%/(\,\mathrm{W} \cdot \mathrm{cm}^2)$. The maximum conversion efficiency is achieved for a pump power $P_p = 400\,\mathrm{mW}$ at the output of the waveguide, corresponding to $1.33\,\mathrm{W}$ at its input.

Signal-to-noise ratio

In this part, we study the signal-to-noise ratio of the conversion. First, we investigate its dependence with the pump power. Combining the expression of η_{tot} and $\mathrm{SNR_{DC}}$, together with equations (5.1) and (5.2), we

obtain

$$\mathrm{SNR}_{\mathrm{DC}}(P_p) = \frac{\mu_{in} \cdot \eta_{tot}(P_p)}{p_N(P_p)} = \frac{\mu_{in} \cdot \eta_{tot}^M \sin^2\left(L\sqrt{P_p \cdot \eta_n}\right)}{\alpha \cdot P_p + p_{DC}}. \tag{5.3}$$

This formula is used to fit the blue circle data points of Fig. 5.5. Since the signal shows an oscillatory behavior while the noise increases linearly with the pump power, $\mathrm{SNR}_{\mathrm{DC}}$ first increases before dropping down to zero. In this case, the solid line has no free parameters, all the quantities having been measured independently. From the figure, we see that the maximum conversion efficiency and signal-to-noise ratio happen for different values of the pump power. We then selected a value of $P_p = 120\,\mathrm{mW}$ to reach a compromise for these two quantities.

5.1.2.3 Behavior as a function of frequency filtering bandwidth

Now, we investigate the dependence of the signal-to-noise ratio as a function of the frequency filtering bandwidth. Previously, I mentioned that there are two main sources of noise, which are leakage and Raman scattering of the pump. Since adding another bandpass filter centered at 1552 nm does not significantly reduce the noise anymore, we expect that Raman noise is the main contribution. This is expected, since the spectrum of Raman scattering usually extends over several hundred of nanometers around the pump wavelength. To verify this, we start by measuring the SNR as a function of μ_{in} for a given value of $\Delta\lambda$, which has a linear behavior if μ_{in} remains sufficiently low. An example of such measurement for $\Delta\lambda \approx 0.68\,\mathrm{nm}$ is shown if Fig. 5.6.

From this measurement, we calculate the quantity μ_1, defined as the mean input photon number per pulse necessary to obtain a signal-to-noise ratio of 1, such that $\mathrm{SNR} = \mu_{in}/\mu_1$. Doing a linear fit of the SNR, μ_1 corresponds to the inverse of the slope. This quantity is a good figure of merit for our system, since it accounts for the conversion efficiency as well as the added noise. We repeat this measurement for several values of $\Delta\lambda$, and plot the

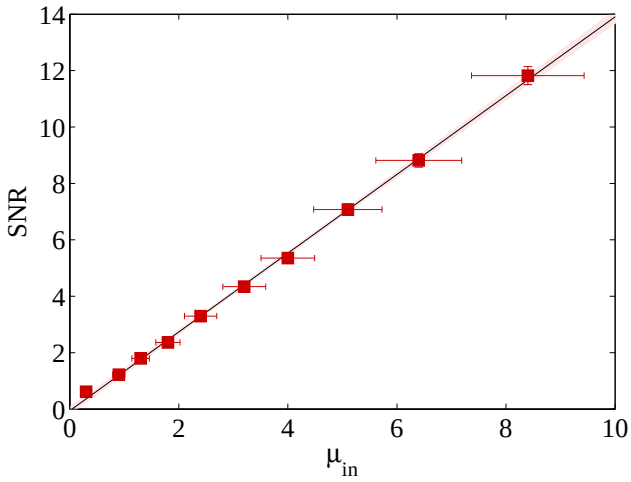

FIGURE 5.6: **Signal-to-noise ratio as a function of the mean input photon number** [121]**.** Red squares: experimental data, with dark counts subtraction. Solid line: linear fit, giving a value of $\mu_1 = 0.7 \pm 0.1$.

various calculated values of μ_1 as a function of $\Delta\lambda$, as shown in Fig. 5.7. If Raman scattering of the pump is the main contribution for the noise, and its level is constant around the output wavelength of 1552 nm, we expect a linear behavior of the noise level as a function of the filtering bandwidth, leading to a linear dependence for μ_1. The experimental data points are in correct agreement with the linear fit, confirming our explanation. This also strongly suggests that a narrower frequency filtering would lead to lower noise level following this linear behavior. Further experimental evidence of this are shown in section 5.2 of this chapter. With the filtering used for this experiment, we were already able to reach the low noise regime with a minimum value of $\mu_{1_{min}} = 0.7 \pm 0.1 < 1$.

The values of $\Delta\lambda$ for each point of Fig. 5.7 have been obtained by varying the position of the outcoupling lens $L2$ along its axis. This modifies the aspect ratio of the output mode. The combination of the diffraction grating with the single mode fiber then allows to select different bandwidths depending on this aspect ratio. For each position, we measure the transmission spectrum of the filtering stage as a function of the wavelength using a tunable laser (Tunics Plus, from Photonetics). The result of this

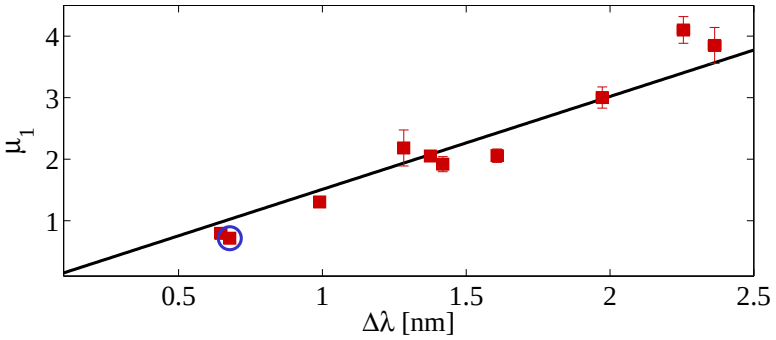

FIGURE 5.7: **Mean input photon number per pulse necessary to obtain a signal-to-noise ratio of 1 as a function of the frequency filter bandwidth** [121]**.** Red squares: experimental data. Solid line: linear fit with no offset.

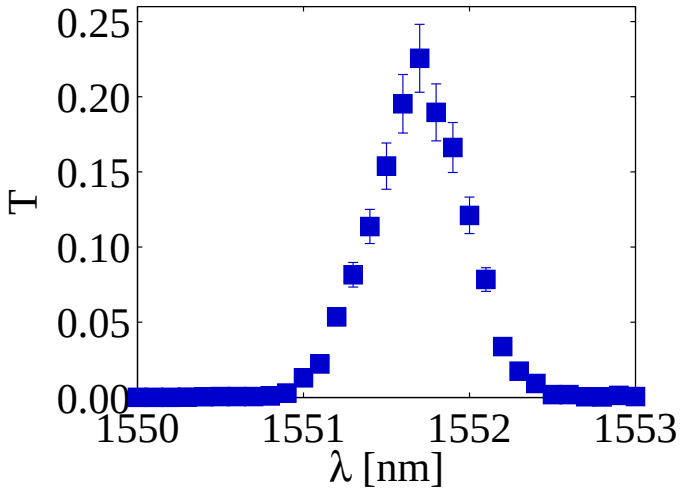

FIGURE 5.8: **Transmission spectrum of the filtering stage** [121]**.**

measurement for the circled point of Fig. 5.7 is shown in Fig. 5.8 as an example.

5.1.2.4 Coherence preservation of the frequency conversion

We verified the preservation of quantum coherence after conversion, in a similar way as in [135, 138]. Quantum coherence preservation in entanglement experiments has been shown as well [140–142, 164]. For this, we performed an interference experiment with a pair of input pulses separated by $\tau = 100\,\text{ns}$ with a phase difference ϕ_l. The input state $|\psi\rangle_{in} = |e\rangle + e^{i\phi_l}|l\rangle$ simulates a time-bin qubit in the early/late ($|e\rangle$ / $|l\rangle$) basis. An interferometer is placed before the telecom SPD in order to measure the coherence of the time-bin qubit. It is realized by combining two 50/50 beamsplitters. The short arm (denoted as S) contains a polarization controller in order to adjust the relative polarization between the two arms, and the long arm (denoted as L) is a $20m$ single mode fiber, introducing a 100 ns time delay between the two arms. The relative path length is passively stabilized by placing the interferometer inside a polystyrene foam box. The measured visibility of the interferences fringes with classical light at 1569 nm is $V_{max} = 96\%$. Since the travel time difference between the two arms of the interferometer equals the time delay τ between the two input pulses, they can exit the interferometer in three temporally separated time slots. The first one corresponds to $|e, S\rangle$, the last one to $|l, L\rangle$, and the intermediate one to an interference between the two indistinguishable states $|e, L\rangle$ and $|l, S\rangle$. The count rate in this central time slot will depend on the relative phase $\phi_l - \phi_i$, where ϕ_i corresponds to the extra phase introduced by the interferometer. The visibility is measured by recording the detection events in the central time slot while the phase ϕ_i is changed. A measurement of the visibility V as a function of μ_{in} is shown in Fig. 5.9. The red squares (resp. blue circles) correspond to a detection gate time of $\Delta t_G = 20\,\text{ns}$ (resp. 50 ns). The values are corrected for the maximal visibility of the interferometer V_{max}, which we mainly attribute to the 500 kHz linewidth of the telecom seed laser. For high values of μ_{in}, we can achieve $V > 0.9$, indicating that the conversion process preserves the coherence of the input state to a great extent. The decrease in visibility with μ_{in} is due to a reduction in the SNR. This is also consistent with the fact that, for a

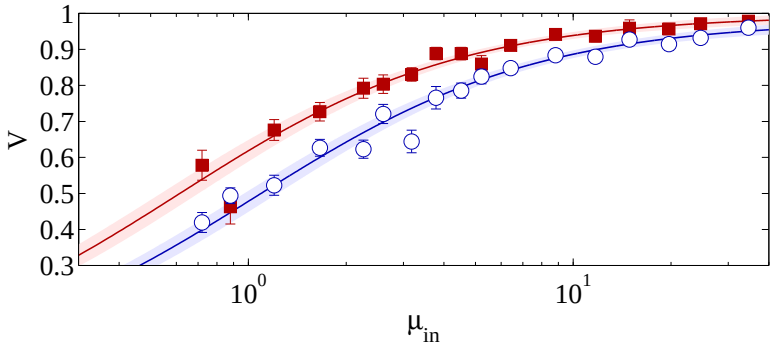

FIGURE 5.9: **Interferences visibility as a function of mean input photon number per pulse** [121]**.** Red plain squares: experimental data with a 20 ns detection gate. Blue open circles: experimental data with a 50 ns detection gate. Solid lines: fits with eq. (5.4). Shaded areas: 95% confidence interval of the fits. The visibilities are corrected for the maximal visibility of the interferometer $V_{max} = 0.96$.

given value of μ_{in}, we observe higher values of V for the shorter detection gate. Both datasets are fitted with the formula

$$V = V_0 \frac{\mu_{in}}{\mu_{in} + \mu_1 \times 2} = V_0 \frac{\mathrm{SNR}}{\mathrm{SNR} + 2}. \tag{5.4}$$

The visibility can be used in order to calculate the conditional fidelity $F_c = (1 + V)/2$ of the output qubit with respect to the input qubit [165], assuming that the conversion has been successful. It is defined as $F_c = \langle \phi_{in} | \rho_{out} | \phi_{in} \rangle$, where ρ_{out} is the density matrix of the output qubit.

In this section, we presented a waveguide-based photonic interface to convert rubidium 87 atoms-resonant light from 780 nm to 1552 nm. We demonstrated conversion of 30 ns weak coherent states with $\mu_1 < 1$. We also showed that the noise generated by the QFCD is broadband, which suggests that it could be diminished by using narrower spectral filtering. In addition, we showed that the conversion process preserves the coherence of time-bin qubits and that the device can operate in the quantum regime. However, the level of noise in this experiment remained too high to allow the conversion of single photons emitted from the quantum memory. This is because the limited retrieval efficiency combined with losses on the way

to the converter would correspond to an input pulse with $\mu_{in} < 1$. In the next section of this chapter, I will present our results on this last point.

5.2 Quantum Frequency Conversion of heralded single photons

In this section, I will present our results on QFC of heralded single photons [26]. We now use heralded single photons emitted by our DLCZ QM as an input to the QFCD, which strengthens the requirements on the μ_1. In this new situation, the mean input photon number per pulse μ_{in} now corresponds to the heralding efficiency η_H propagated to the input of the QFCD. We define η_H as the retrieval efficiency of the QM corrected for the detection efficiency, multiplied by the propagation losses between the two systems. Hence, SNR $= \eta_H/\mu_1$, which means that we need to have $\mu_1 \ll \eta_H$ in order to obtain a high SNR with single photons. In this light, we modified the filtering stage of the QFCD presented in the first section to obtain a narrower frequency filtering. We also operate the QM using short read pulses, producing short read photons. In this way, we limit the noise contribution of the converted read photons, allowing us to obtain a lower value for the μ_1 than the one of section 5.1. This improvement allowed us to operate the device in the quantum regime and to preserve the non-classical nature of the correlations between the write and converted read photons. In the following, I will first give more details about the modified experimental setup, before presenting our experimental results.

5.2.1 Experimental setup

As mentioned previously, two main modifications have been made to the experimental setup for this experiment with respect to the one presented in section 5.1.

Narrower frequency filtering for the QFCD

The frequency filtering stage placed after the waveguide have been modified with respect to the one described in paragraph 5.1.1. The long-pass filter (cut-off at 1450 nm) and diffraction grating have been removed. Instead, we installed a fiber Bragg grating (FBG) with a bandwidth of 2.5 GHz and a transmission efficiency of 0.7. It is placed between the single-mode fiber coupling and the telecom SPD. With this new configuration, the total transmission is slightly higher than previously, and the filtering bandwidth passes from a minimum of ~ 80 GHz to 2.5 GHz, which was the key element for the obtention of a lower value for the μ_1.

DLCZ quantum memory as input light source

Instead of sending WCPs to the input of the QFCD, we now use heralded read (anti-Stokes) photons retrieved from the quantum memory, as depicted in Fig. 5.10. The $|g\rangle$, $|e\rangle$ and $|s\rangle$ states respectively correspond to the $|F = 1\rangle$, $|F' = 2\rangle$ and $|F = 2\rangle$ hyperfine levels of the D_2 line of ^{87}Rb. The atoms are initially prepared in $|g\rangle$. No homogeneous magnetic field is applied, so the Zeeman levels are degenerate. Weak write pulses with a FWHM of 16 ns and blue detuned by 40 MHz from the $|g\rangle \rightarrow |e\rangle$ transition are sent to the atoms until the detection of a write (Stokes) photon heralds the creation of a spin-wave. The photons/spin-waves pairs are created with a probability p in the collection mode, and the photons are detected with a probability $p_w < p$ due to the various transmission and detection inefficiencies. After a 330 ns delay, an 11 ns read pulse resonant with the $|s\rangle \rightarrow |e\rangle$ transition is sent and converts the spin-wave onto a read photon. Conditioned on the detection of a write photon, the telecom SPD is triggered to detect the converted read photon.

A more detailed representation of the experimental setup is shown in Fig. 5.11. The duration of the write photons (16 ns) corresponds to a FWHM of 27.5 MHz for bandwidth-limited Gaussian pulses, leading to a spectral transmission through the cavity of 91%, for a total transmission of the photons of $\sim 45\%$. The value of 91% is calculated from the convolution

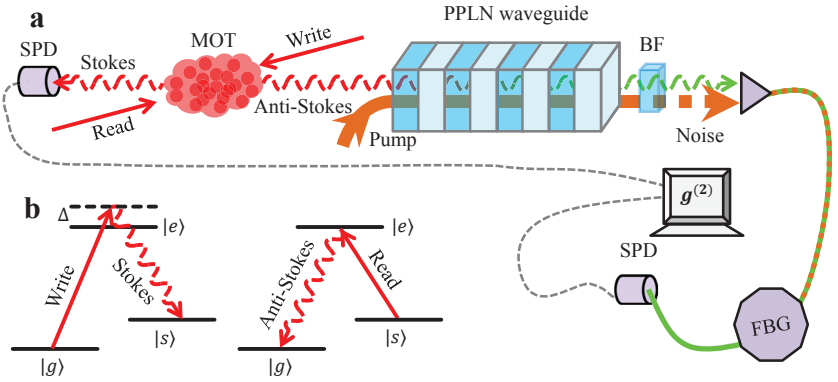

FIGURE 5.10: **Experimental setup for the QFC of heralded single photons.** SPD: single photon detectors. BF: bandpass filter. FBG: fiber Bragg grating.

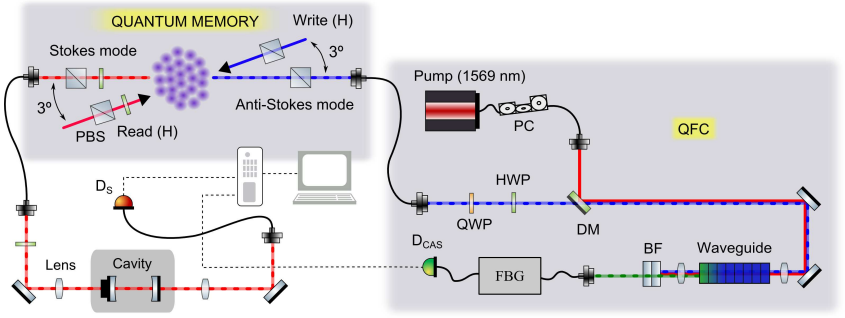

FIGURE 5.11: **Detailed experimental setup for the QFC of heralded single photons** [26]**.** D_S: write (Stokes) photons detector. D_{CAS}: converted read (anti-Stokes) photons detector. QWP: quarter-wave plate. HWP: half-wave plate. PC: polarization control. DM: dichroic mirror. BF: bandpass filters.

product of two Gaussian functions with FWHM of 60 MHz and 27.5 MHz, corresponding to the FFC and the write photons respectively. Calling f

the FFC spectrum and g the write photon spectrum, we have

$$f(\nu) = \frac{1}{\sigma_{FFC}\sqrt{2\pi}} e^{-\frac{\nu^2}{2\sigma_{FFC}^2}}, \tag{5.5}$$

$$g(\nu) = \frac{1}{\sigma_w\sqrt{2\pi}} e^{-\frac{\nu^2}{2\sigma_w^2}}, \text{and} \tag{5.6}$$

$$(f * g)(\nu) = \frac{1}{\sqrt{2\pi(\sigma_{FFC}^2 + \sigma_w^2)}} e^{-\frac{\nu^2}{2(\sigma_{FFC}^2+\sigma_w^2)}}. \tag{5.7}$$

The maximum spectral transmission of the write photons through the cavity T_{FFC}^w is then the amplitude of the convolution relative to the FFC transmission, given by

$$T_{FFC}^w = \frac{(f * g)(0)}{f(0)} = \frac{\sigma_{FFC}}{\sqrt{\sigma_{FFC}^2 + \sigma_w^2}} \approx 0.91. \tag{5.8}$$

A subsequent fiber coupling with 50% efficiency brings the filtered light to the SPD. The transmission of light from the write pulses, detuned by 6.8 GHz from the write photons, is below 1%. We estimate that $p_w = 0.07\times p$, accounting for the coupling efficiency of the photons into the collection fiber (0.7), FFC and subsequent fiber coupling transmission (0.23), and the visible SPD efficiency ($\eta_{d,780} = 0.43$). Third, we use spatial filtering by setting a 3° angle between the write pulse and write photons detection modes, to avoid direct coupling of the light in the detection arm. With these three methods, only a small fraction of unpolarized scattered light can reach the detector, which level is low enough not to be a limitation for our experiment.

In order to distinguish the read photons from the read pulses, only the polarization and spatial filtering are used, without the FFC. This is because the finite cavity transmission, together with the imperfect mode-matching between its output mode and the waveguide input mode, were reducing the heralding efficiency η_H. In terms of SNR, this proved to be more detrimental than the remaining noise present without the FFC and reducing

the μ_1 value. It was then more profitable to have a higher heralding efficiency together with a slightly lower μ_1 due to the lack of noise filtering. We selected the value of 3° for the spatial filtering angle in order to reduce this noise level as much as possible without significantly decreasing the retrieval efficiency of the QM at our short storage time.

5.2.2 Experimental results

5.2.2.1 Characterization of the Quantum Memory

We first performed some measurements on the DLCZ QM while it was not connected to the QFCD. Instead, the read photons were sent directly to a visible SPD, also without passing through the FFC. The results of these measurements are shown if Fig. 5.12. Part (a) shows the temporal shape of

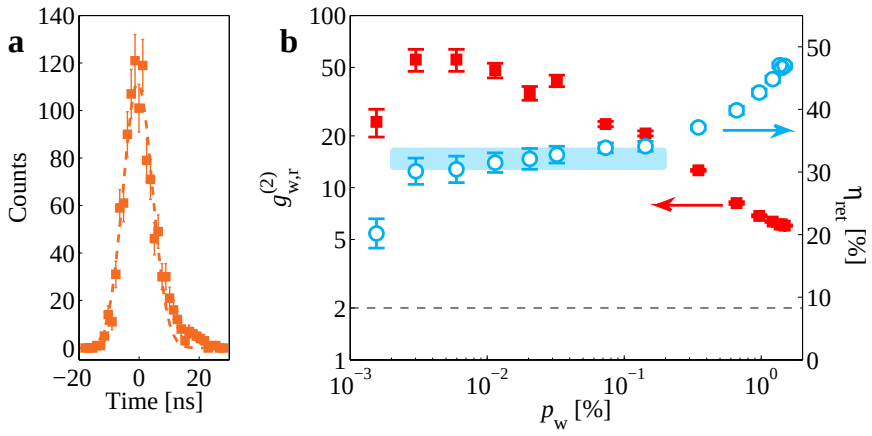

FIGURE 5.12: **Characterization of the DLCZ QM** [26]**.** (a) Temporal shape of the retrieved read photons, integrated over 109 s, with $p_w = 0.15\%$. (Dashed line) Gaussian fit with FWHM $= 11.4 \pm 0.9$ ns. (b) Second order cross-correlation function between the write and read photons $g^{(2)}_{w,r}$ (red plain squares, left axis) and retrieval efficiency η_{ret} (blue open circles, right axis), as a function of p_w.

the retrieved photons. A Gaussian fit yields a FWHM of 11.4±0.9 ns, which is shorter than the spontaneous decay time constant of 26 ns due to the

excited state lifetime, and shorter than previous single photons generated by the same method [114, 120]. As mentioned previously, short photons are desirable in view of QFC experiments, since shorter detection gates on the telecom SPDs lead to higher SNR. In Fig. 5.12 (b), we show measurements results for the second order cross-correlation function between the write and read photons $g^{(2)}_{w,r}$ (red plain squares, left axis) and the retrieval efficiency η_{ret} (blue open circles, right axis), as a function of p_w. Here, it reaches 56 ± 8 for low values of p_w, before dropping due to the detectors dark counts. The dashed line indicates the classical limit for the value of $g^{(2)}_{w,r}$ assuming thermal statistics for the auto-correlation functions of the write and read fields taken independently ($g^{(2)}_{w,w} = g^{(2)}_{r,r} = 2$). The retrieval efficiency is only compensated for detection efficiency. It is approximately constant and equal to $32 \pm 2\%$ in the region of the blue shaded area, for p_w between 0.002 and 0.2%. This corresponds to the single excitation regime, where the high order terms in the two-mode squeezed state of eq. (2.3) are negligible. The value drops also for low values of p_w due to the dark counts limitation. It increases for high values of p_w, because when multiple spin-waves are created in our detection mode, the conditional probability to retrieve a read photon increases artificially.

5.2.2.2 Ultra-low noise frequency conversion

After the characterization of the DLCZ QM, we separately characterized the QFCD using WCPs, in a similar way as for the experiment presented in the first section (5.1) of this chapter. The results of this characterization are summarized in Fig. 5.13. The data of Fig. 5.13 (a) can be compared wit the ones of Fig. 5.5, keeping in mind that the former one were acquired with $\mu_{in} = 0.37$, while the latter with $\mu_{in} = 6.1$, which will affect the SNR but not the conversion efficiency. The data of the device efficiency are fitted with a formula similar to the one of eq. (5.2) but for η_{dev},

$$\eta_{dev} = \eta^{M}_{dev} \sin^2 \left(L \sqrt{P_p \cdot \eta_n} \right). \tag{5.9}$$

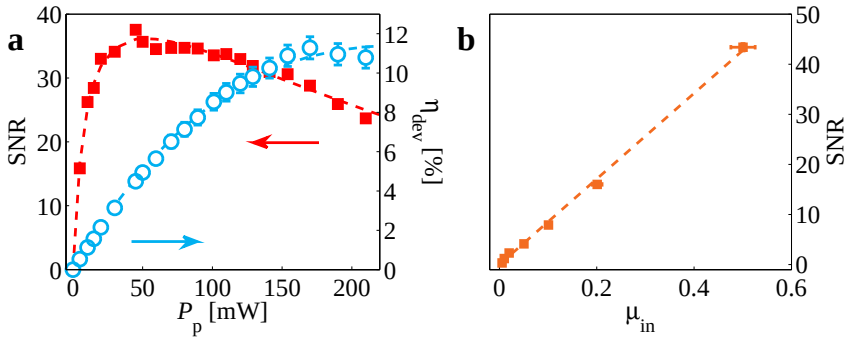

FIGURE 5.13: **Characterization of the QFCD with WCPs** [26]**.** (**a**) Signal-to-noise ratio (plain red squares, left axis) and device efficiency (empty blue circles, right axis) as a function of the pump power measured at the output of the waveguide, for $\mu_{in} = 0.37$. (**b**) Signal-to-noise ratio after dark-counts subtraction, as a function of the mean input photon number per pulse.

The fit yields $\eta_{dev}^{M} = 11.4 \pm 0.4\%$ and $\eta_n = 119 \pm 9\%/(\,\mathrm{W} \cdot \mathrm{cm}^2)$. These values can be compared with the ones given at the end of paragraph 5.1.2.2. They were 6.6% and $72 \pm 7\%/(\,\mathrm{W} \cdot \mathrm{cm}^2)$ respectively. The fact that we get a higher normalized efficiency means that we are able to achieve the maximum conversion efficiency for a lower pump power. Moreover, this maximum conversion efficiency is also higher as seen from the value of η_{dev}^{M}. This is due to an improvement of the mode overlap between the pump and signal light fields inside the waveguide, as well as lower transmission losses in the filtering stage. However, the maximum measured device efficiency η_{dev}^{M} corresponds to a maximum internal waveguide conversion efficiency $\eta_{int}^{M} = 77\%$. This means that despite this improvement, the mode overlap is still not perfect. The maximum achievable device efficiency is calculated to be 17.6%, limited only by optical losses. This includes the waveguide incoupling (60%) and transmission (70%) efficiencies of the photons at 780 nm, and the fiber coupling efficiency (60%) and FBG transmission (70%) for the converted photons at 1552 nm. The data of the dark-counts subtracted signal-to-noise ratio are fitted with eq. (5.3). The data of Fig. 5.13 (a) can be directly compared wit the ones of Fig. 5.6. We use the same formula

SNR $= \mu_{in}/\mu_1$ for the fit, and find $\mu_1 = (11.8 \pm 0.4) \times 10^{-3}$. This is about 60 times smaller than the value of 0.7 ± 0.1 obtained in the previous experiment. This is due to the narrower bandwidth of the FBG replacing the diffraction grating and the increase of the device efficiency, as well as the use of shorter photons.

5.2.2.3 Quantum frequency conversion of heralded single photons from the DLCZ quantum memory

We then connected the output of the DLCZ QM to the input of the QFCD. We chose a value for p_w of 0.16%, close to the limit of the single excitation regime. From the measured retrieval efficiency and the transmission losses between the two systems η_{trans}, we infer a mean read photon number before the QFCD corresponding to $\eta_{ret}^{in} = 0.25 \pm 0.02$, conditioned on the detection of a write photon. We use a SPD with an efficiency $\eta_{d,1552} = 0.1$ and 400 Hz dark counts rate (ID220, from ID Quantique). In Fig. 5.14 (a), we show the temporal shape of the heralded read photons after conversion (orange squares). We fit it with a 13 ± 1 ns FWHM Gaussian profile, very similar to the value before conversion. From this we deduce that the conversion preserves the temporal shape of the photons. The green circles correspond to the QFCD noise, obtained by blocking the input signal. The calculated value of 18 ± 5 gives an upper bound for the achievable value of the cross-correlation function between write and converted read photons $g_{w,r}^{(2)c}$ (see paragraph 5.2.2.3). We also measured the device efficiency as a function of the pump power in this configuration, as shown in Fig. 5.14 (b), on the right axis. Here, the device efficiency corresponds to the probability to obtain a converted read photon in a single mode fiber after the QFCD (including the frequency filtering stage), conditioned on the detection of a write photon, such that $\eta_{dev} = p_{w,r}^{c}/(p_w \eta_{ret}^{in} \eta_{d,1552})$, where $p_{w,r}^{c}$ is the probability to detect a coincidence between write and converted read photons. The data are fitted with eq. (5.9). From this fit, we find $\eta_{dev}^{M} = 13.6 \pm 0.1\%$, and $\eta_n = 120 \pm 10\%/(\mathrm{W} \cdot \mathrm{cm}^2)$. These values are compatible with the one which we

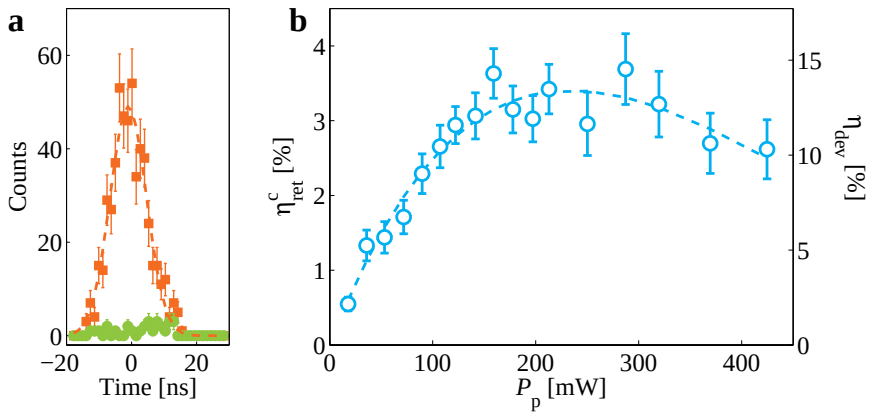

FIGURE 5.14: **Characterization of the QFCD with heralded read photons** [26]**.** (**a**) Temporal shape of the retrieved read photons after conversion, integrated over 2180 s (10^8 trials), with $p_w = 0.16\%$ and $P_p = 120$ mW. The measured signal-to-noise ratio is 18 ± 5. (**b**) Conversion efficiency as a function of pump power after the waveguide measured with heralded read photons. (Right axis) Device efficiency. (Left axis) Retrieval efficiency after conversion, which is the probability to find a converted photon before the SPD, conditioned on a write photon detection. (Dashed line) Fit of the experimental data using eq. (5.9). For this measurement the number of trials varies from 10^7 to 2×10^7.

obtained from the characterization with WCPs. The left axis of Fig. 5.14 (b) shows $\eta^c_{ret} = \eta^{in}_{ret}\eta_{dev}$, which is the combined conditional efficiency of the QM + QFCD system, including all losses.

Non-classical correlations preservation

After the temporal shape preservation and efficiency characterization, we verified that the QFCD also preserves the non-classicality of the correlations. For this, we measured the value of $g^{(2)c}_{w,r}$ as a function of p_w. The results of this measurement are shown in Fig. 5.15 (red squares). We observe a behavior comparable with the one of the $g^{(2)}_{w,r}$ shown in Fig. 5.12. One difference is that the maximum value of $g^{(2)c}_{w,r}$ is achieved for much higher value of p_w, due to the background noise induced by the telecom pump. Still, this noise level remains sufficiently low to observe values of $g^{(2)c}_{w,r}$ well above 2. Another difference is that its maximum value is much

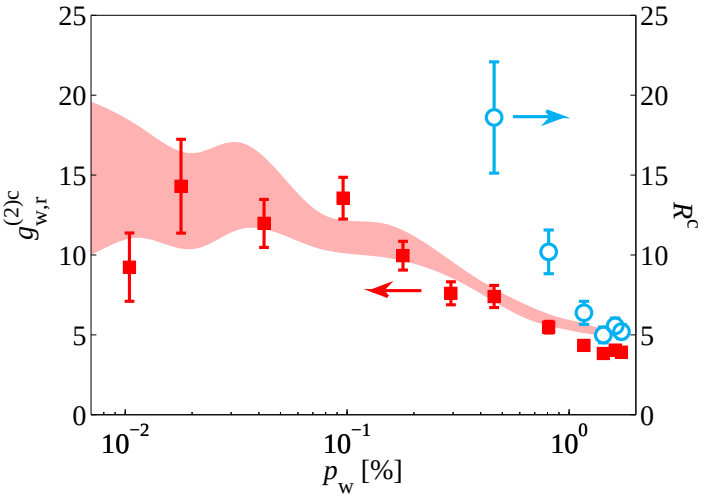

FIGURE 5.15: **Characterization of the correlations between write and converted read photons** [26]**.** The data are plotted as a function of p_w. Red plain squares, left axis: second order cross-correlation function between write and converted read photons, at 140 mW pump power. The shaded area represents the expected calculated value according to eq. (5.12). Blue open circles, right axis: Cauchy-Schwarz parameter.

lower than the one of $g^{(2)}_{w,r}$ without conversion. This is expected, and can be explained in the following manner. The probability to detect a read photon after conversion is $p^c_r = \eta_{conv} \cdot p_r + p_n$, where p_n is he probability to detect a noise photon and $\eta_{conv} = \eta_{trans} \cdot \eta_{dev} \cdot (\eta_{d,1552}/\eta_{d,780})$. The probability to detect an accidental coincidence is $p^c_r \cdot p_w = \eta_{conv} \cdot p_r \cdot p_w + p_n \cdot p_w$, while the probability to detect a correlated coincidence is $p^c_{w,r} = \eta_{conv} \cdot p_{w,r} + p_n \cdot p_w$. We can then express the second-order cross-correlation function between write and converted read photons as

$$g^{(2)c}_{w,r} = \frac{\eta_{conv} \cdot p_{w,r} + p_n \cdot p_w}{\eta_{conv} \cdot p_r \cdot p_w + p_n \cdot p_w}. \tag{5.10}$$

From this expression, it is clear that a noiseless conversion would not reduce the value of $g^{(2)c}_{w,r}$ with respect to the one before conversion, independently of the efficiency of the conversion process. Defining the signal-to-noise

ratio for the conversion process of the heralded read photons as

$$\mathrm{SNR} = \frac{\eta_{conv} \cdot p_{w,r}}{p_n \cdot p_w}, \tag{5.11}$$

we get the more intuitive expression

$$g^{(2)c}_{w,r} = g^{(2)}_{w,r} \frac{\mathrm{SNR} + 1}{\mathrm{SNR} + g^{(2)}_{w,r}}. \tag{5.12}$$

We see from this formula that $g^{(2)c}_{w,r} \xrightarrow[g^{(2)}_{w,r} \to \infty]{} = 1 + \mathrm{SNR}$. The SNR limits the non-classicality of the correlations after conversion, independently of their level before. The shaded area in Fig. 5.15 corresponds to the expected value of $g^{(2)c}_{w,r}$ obtained according to the formula (5.12), using the values taken from the data of Fig. 5.12 (b) for $g^{(2)}_{w,r}$. We took the value $\mathrm{SNR} = \eta^{in}_{ret}/\mu_1 = 21.2 \pm 0.1$.

The blue open circles on Fig. 5.15 represent the Cauchy-Schwarz parameter R^c (right axis). It is defined as

$$R^c = \frac{\left(g^{(2)c}_{w,r}\right)^2}{g^{(2)}_{w,w} \cdot g^{(2)c}_{r,r}}, \tag{5.13}$$

where $g^{(2)}_{w,w}$ (resp. $g^{(2)c}_{r,r}$) are the unconditional auto-correlation function for the write (resp. converted read) photons. For classical fields, the Cauchy-Schwarz inequality $R^c \leq 1$ must be satisfied. This inequality is clearly violated with our data, which proves the non-classical nature of the correlations.

The measurement of the auto-correlation functions for the write and the converted read photons are shown in Fig. 5.16. To perform these measurements, we prepared Hanbury-Brown and Twiss interferometers by separating the photonic fields on a balanced beam-splitter before detection by two SPDs. The expected value for the auto-correlation functions is 2, because these fields taken independently have a thermal distribution [150, 151]. This is the case for the write photons. However, for the read photons, the

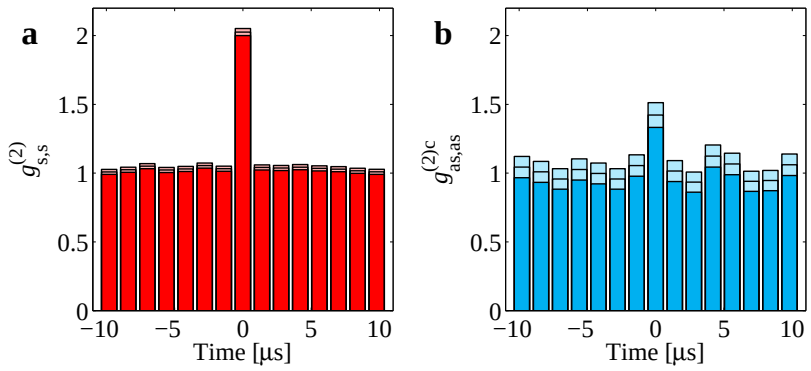

FIGURE 5.16: **Auto-correlation measurements** [26]**.** (a) Measurement for the write photons, with a value of $g^{(2)}_{w,w} = 2.03 \pm 0.03$. (b) Measurement for the converted read photons, with a value of $g^{(2)}_{r,r} = 1.4 \pm 0.1$.

measured value is systematically below 2, even before the QFC operation. This can be explained by the absence of the FFC in this case, adding noise from the leakage of the read pulse to the read photons field. Since this noise is coherent light, it reduces the SNR by adding a background with an auto-correlation value of 1. After conversion, this component should be reduced by the FBG, but extra noise due to pump laser leakage and dark counts is added.

To further quantify the performances of the QFCD + QM system, we also measured the coincidences rates of our QM with and without QFC, as shown in Fig. 5.17. The coincidence probabilities $p_{w,r}$ with and without QFC as a function of p_w are displayed on the left axis, and the corresponding coincidence rates on the right axis. In the single excitation regime, the coincidence rates are below few 10^{-1} Hz. This value may not seem very impressive. However, these rates could be increased by several methods. The first method is to increase the duty cycle of the protocol. It is mainly limited by the loading time of the MOT, and the possible interrogation time of the ensemble. The duty cycle could be increased by optimization of the MOT loading sequence. The interrogation time could be extended by having a cloud with higher OD. A second method of particular interest

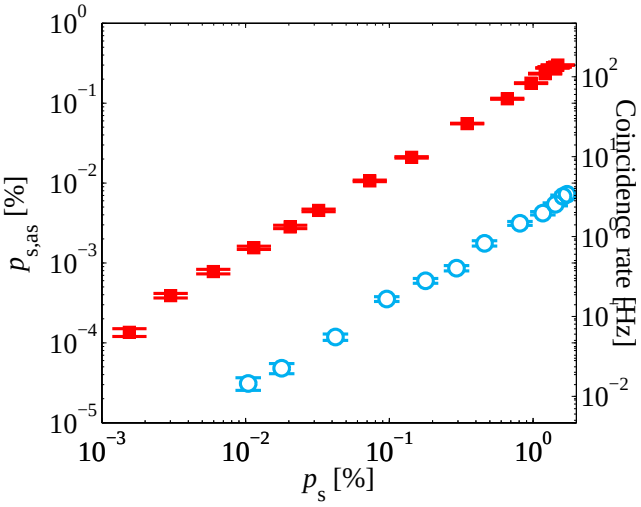

FIGURE 5.17: **Heralded read photons generation rates** [26]**.** The data are plotted as a functino of p_w. Left axis: probability to detect a coincidence per trial, without ($p_{w,r}$, red plain squares) and with QFC ($p^c_{w,r}$, blue open circles). Right axis: corresponding coincidences detection rates.

is the introduction of multiplexing in the DLCZ protocol. Since the rates in this protocol are also limited by the classical communication time between the SPDs and the control electronics, temporal multiplexing would be an important improvement.

5.3 Discussion on the Quantum Frequency Conversion experiments

The main limitation of our QFCD is the achievable SNR, as explained previously. There are three possible ways to increase this parameter. One would be to improve the device efficiency, mainly by obtaining a better mode overlap between the pump and input light within the waveguide. Another solution is to improve the retrieval efficiency of the QM, therefore increasing the effective μ_{in} via a higher value of η^{in}_{ret}. However, we are probably limited by the OD of the atomic cloud. The third possibility

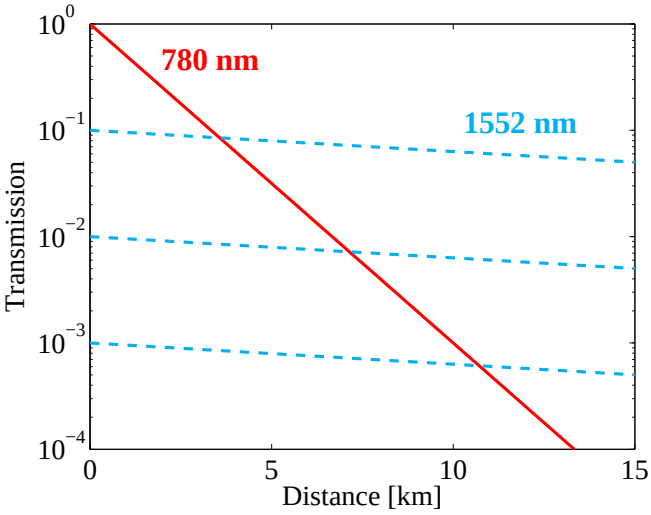

FIGURE 5.18: **Comparison between transmissions of photons with and without QFC** [26]**.** The transmission is plotted for standard optical fibers as a function of the distance. Red line: photons at 780 nm. Dashed blue lines: converted photons at 1552 nm, for device efficiencies of 10, 1 and 0.1% (top to bottom).

is to further decrease the bandwidth of the filtering stage, until we are limited by the spectral width of our read photons. This can be achieved by the addition of a Fabry-Perot etalon in combination with the FBG, and is actually used in further QFC experiments.

However, despite the finite efficiency and SNR of our QFCD, we are able to operate in the non-classical regime at the single photon level. In Fig. 5.18, we show a comparison for the transmission efficiency of single photons in optical fibers as a function of the distance, for 780 nm (losses of 3 dB/km) and 1552 nm (losses of 0.2 dB/km), with various device efficiencies. We see that even for a device efficiency as low as 0.1%, QFC-based protocols outperform direct transmission after only ≈ 11 km of propagation in optical fibers. In our case, with $\eta_{dev} > 10\%$, QFC becomes advantageous after ≈ 3 km.

In this chapter, we demonstrated quantum frequency conversion of weak

coherent states with $\mu_1 = 1.2 \times 10^{-2}$, corresponding to a maximum signal-to-noise ratio of ≈ 85 for an average input photon number of 1 per pulse. This allowed us to successfully convert heralded single photons produced by a DLCZ-type quantum memory while conserving the non-classical nature of the correlations between photon pairs. This approach, based on a solid-state waveguide technology, is appropriate for integration of a set of quantum repeater nodes within the existing telecom fibers network, in view of the development of a large scale quantum repeater. An important feature is the possibility to convert any input wavelength to a desired output wavelength by carefully selecting the appropriate pump wavelength and poling period of the crystal. This flexibility enables the use of this type of QFC with a broad range of quantum systems emitting at various wavelengths. In particular, QFC to telecom wavelength is required to enable long-distance DLCZ-like QRs based on atomic ensembles emitting light in the near infrared domain.

Chapter 6

Towards a temporally multiplexed quantum repeater

The first section of this chapter will be dedicated to the presentation of the temporally-multiplexed DLCZ protocol [166]. In the second section, I will present our experimental results which are the first enabling steps towards this goal. We performed controlled dephasing and rephasing of single collective atomic excitations, and selective rephasing of one out of two temporal modes[19].

6.1 Temporal multiplexing with the DLCZ protocol

The main interest of introducing temporal multiplexing in the DLCZ protocol is to offer a significant improvement in entanglement rates with respect to the non-multiplexed protocol for a given fidelity, which will be very beneficial for realistic quantum repeaters applications. This is done by sending a train of consecutive write pulses in each trial, and selectively reading out only the spin-wave in the temporal mode associated with a successful write photon detection event. This is possible by actively dephasing the spin-waves in all temporal modes, and ensuring that only the correct one is rephased at the readout time. In the first section, I will start by justifying more in details the interest of the temporally-multiplexed DLCZ protocol, before explaining the underlying processes.

6.1.1 Interest of temporal multiplexing

The DLCZ protocol is attractive for the realization of QRs due to the fact that it relies on atomic ensembles (enabling the possibility to reach high efficiencies) and linear optics (making it relatively simple to implement). However, as for any QR protocol, the entanglement generation rates decrease with distance, becoming too low for practical applications other than proof of principles after a few hundred kilometers [124].

Standard DLCZ protocol

In the standard DLCZ protocol, atoms are first loaded in a MOT and write pulses are sent until successful detection of a write photon, during a maximum duration called interrogation time (IT). If no write photon is detected before the end of the IT, the sequence is repeated. A successful write photon detection heralds the creation of a spin-wave, which can be read-out at a later time, creating a non-classically correlated (and ideally entangled) read photon. Neglecting the MOT loading time, the photon pairs generation rate is limited by the minimum possible delay between two consecutive write pulses. This delay can not be made arbitrarily short, due to the heralded nature of the protocol. With this type of QRs, one must wait to know if entanglement was successfully generated between two remote atomic ensembles, translating in a write photon detection at a central measurement station, before sending the next write pulse in the absence of such event. The waiting time is given by the sum of the propagation times of the write photon from the QM to the measurement station, and of the classical output signal back to the QM.

Calling l_{trans} the length of the transmission channel between the atomic ensemble and measurement stations, the communication time is $\Delta t_w = 2l_{trans}/v_p = 2l_{trans} \cdot n/c \approx 3l_{trans}/c$, corresponding to 10 ns per meter, with v_p the photons velocity and $n \approx 1.5$ the fiber refractive index. The corresponding maximum rate for the write pulses is given by $R_{w,1} = 1/\Delta t_w$. In the scale of a laboratory experiment, where l_{trans} is typically of the order of a few meters, this delay is negligible. However, in view of realistic QR applications where this length would be of the order of several tens of kilometers, Δt_w reaches several hundreds of microseconds. Considering a typical IT of the order of a millisecond, only a few trials could be performed for each MOT, limiting the write pulses rate to approximately the MOT repetition rate. As a consequence, the photon pairs and entanglement generation rates would become forbiddingly small.

Fortunately, a convenient solution around this major issue has been proposed [122, 166], based on temporal multiplexing. This allows us to partly

overcome the limitations due to the communication time, and to significantly increase the QR's repetition rate. In the following section, we will analyze the improvements allowed by the protocol presented in [166] in more details, considering an exact expression for the write pulses rate.

Temporally multiplexed DLCZ protocol

In the temporally multiplexed version of the protocol, a train of N consecutive write pulses separated by a time interval δt_w is sent during each trial, instead of a single pulse, as represented in Fig. 6.1. Here, the duration of

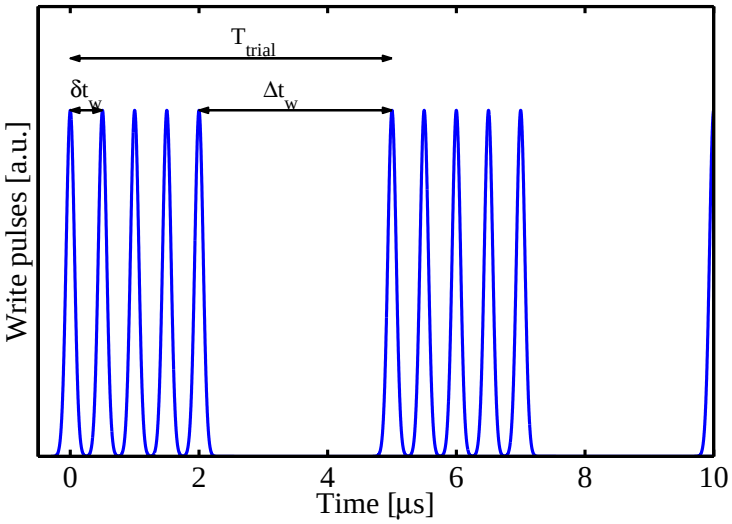

FIGURE 6.1: **Write pulses trains for temporal multiplexing.** In this example, trains of 5 consecutive pulses separated by $\delta t_w = 200\,\text{ns}$ are sent with a delay of $\Delta t_w = 3\,\mu\text{s}$.

one trial is $T_{trial} = \Delta t_w + (N-1)\delta t_w$. It is not necessary anymore to wait for Δt_w between each pulse, but only after the last pulse of each train, in order to verify if heralded entanglement has been generated. This is affecting the pulses rate, which is not increasing linearly with the number of pulses per train. In [166], it was implicitly assumed that $(N-1)\delta t_w << \Delta t_w$. Here, we relax this hypothesis and consider cases where the two values are comparable.

The enhancement of write pulses rate in the multiplexed case can be written as

$$R_{w,N} = \frac{N}{T_{trial}} = \frac{N}{\Delta t_w + (N-1)\delta t_w} = \frac{N}{1 + (N-1)/b_t} R_{w,1}, \qquad (6.1)$$

where $b_t = \frac{\Delta t_w}{\delta t_w}$ is the "temporal bandwidth" of the memory, approximately equal to the number of temporal modes fitting within the delay given by the communication channel length.

Each pulse is sent in a well-defined time-bin (or temporal mode), so that they do not overlap in time. The detection of a write photon associated with the pulse $i \in [1; N]$ heralds the creation of a spin-wave in the corresponding time-bin. It is then possible to selectively read-out only this specific spin-wave and convert it to a single read photon which will be strongly correlated with the detected write photon.

In Fig. 6.2, we show this rate enhancement factor as a function of the number of write pulses per train. The chosen values for δt_w and Δt_w

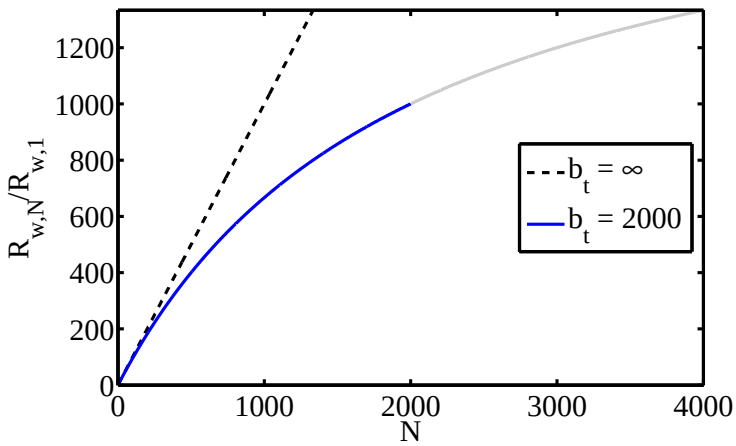

FIGURE 6.2: **Write pulses rate enhancement with temporal multiplexing.** Relative enhancement factor in the write pulses rate as a function of the number of pulses per train. (Blue line) Region with an important enhancement factor varying from N to $N/2$, up to $N-1 = b_t$. (Grey line) Region where the benefit of increasing N starts to become less important, limited by the temporal bandwidth. (Dashed black line) Linear limit with unit slope ($b_t \to \infty$).

are 500 ns and 1 ms respectively, the latter corresponding to a distance between two nodes of 200 km. The temporal bandwidth in this case is $b_t = 2000$. These values will also be used in the following figures of the present section. In the case where $N - 1 \ll b_t$, eq. (6.1) simplifies to $R_{w,N} \approx N \cdot R_{w,1}$, represented by the dashed line. With the chosen values, this approximation is valid up to $N \approx 400$, corresponding to a pulse train duration of $\sim 200\,\mu$s. The benefit of increasing N starts to become less important when $N - 1 = b_t$. The enhancement factor reaches a value of $N/2$ at this point.

The maximum possible enhancement strongly depends on b_t, as shown in Fig. 6.3. Higher values will allow greater benefits from the temporal

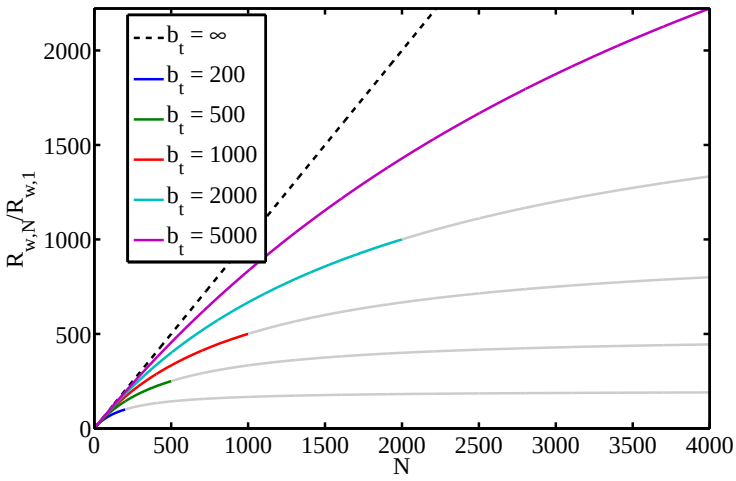

FIGURE 6.3: **Write pulses rate enhancement dependence on the temporal bandwidth.** Relative enhancement factor in the write pulses rate as a function of the number of pulses per train, for several temporal bandwidths. (Color lines) Regions with an important enhancement factor varying from N to $N/2$, up to $N - 1 = b_t$. (Grey line) Region where the benefit of increasing N starts to become less important, limited by the temporal bandwidth. (Dashed black line) Linear limit with unit slope ($b_t \to \infty$).

multiplexing. This clearly illustrates that the longer the communication channel, the more useful temporal multiplexing is. For a fixed length,

higher values of b_t can also be achieved by reducing δt_w. However, this requires a larger spectral bandwidth for the QM.

Temporal multiplexing requires multimode QMs, and its implementation in the DLCZ protocol was proposed using CRIB on the spin transition [166]. The ability to read out the spin-wave created in only one specific temporal mode is the key point of this protocol, and I will now detail its functioning.

6.1.2 Temporally multiplexed DLCZ repeater

6.1.2.1 Comparison between standard and selective readout

I will now consider and compare different cases in order to demonstrate the necessity of the selective readout via controlled rephasing of the spin-wave. For simplicity, I will assume that there is no dephasing induced by atomic motion or spurious magnetic fields.

Case 1: 1 write pulse, standard readout
This case is the one of a standard DLCZ experiment. At each trial, a single write pulse is sent on the atoms. The detection of a write photon, with a probability $p_w \ll 1$, heralds the creation of a spin-wave, which is then read out and mapped onto a correlated read photon.

Case 2: N write pulses, standard readout
In this case, a train of several write pulses is sent on the atoms. The detection of a write photon, with a probability $p_{w,N} \leq 1$, also heralds the creation of a spin-wave, which can be associated with one of the write pulses, depending on the moment when the photon was detected. This spin-wave can also be read out and mapped onto a correlated read photon. The only difference is that the values of $g^{(2)}_{w,r}$, and/or η_{ret} may be different, depending on the difference between p_w and $p_{w,N}$. However, if $p_{w,N} > p_w$,

as it should be in order to achieve higher write photons detection rates, $g^{(2)}_{w,r}$ will be lower, hence counterbalancing the gain in rates. In the absence of any dephasing of the spin-wave, this case is formally equivalent to the first one.

Case 3: 1 write pulse, controlled rephasing

In this case we consider again a single write pulse per trial. In addition to the first case, we now assume that the created spin-wave heralded by a write photon detection will quickly dephase, and rephase at a given time $t_r = 2t_0$ before dephasing again indefinitely, allowing to read it out efficiently only at this specific time. t_0 is defined as the time at which the rephasing command is given with respect to the write pulse time. Sending the read pulse at a different time than t_r will produce an uncorrelated read photon in a random direction.

Case 4: N write pulses, controlled rephasing with selective read-out

We now consider a combination of cases 2 and 3. A train of N write pulses is sent, and we call $t_1, \cdots, t_N$ the times of each pulse of the train. Again, the rephasing command is given at $t_0 > t_N$. A spin-wave associated with the pulse i will then rephase symmetrically with respect to t_0, at a time $t_{r,i} = 2t_0 - t_i$, while all the others will be dephased. In the case of a write photon detection associated with the pulse i, it is now possible to read-out only the spin-wave heralded by this one photon, efficiently creating a correlated read photon, while all the other possible spin-waves will be dephased. Assuming no errors, it would be possible to operate with the same probability p_w per pulse as in the single-pulse case, such that $p_{w,N} = 1 - (1 - p_w)^N$, while still obtaining the same value for $g^{(2)}_{w,r}$.

However, in practice, the fact that multiple write pulses are sent introduces errors depending on $p_{w,N}$, limiting the advantage of this type of temporal multiplexing without a proper handling of these errors. Fortunately,

their contribution can be made negligible by introducing an optical cavity around the atomic ensemble [166], which has to be resonant with the write photons but transparent for the read ones. In the next section I will detail these errors, before explaining the role and effect of the optical cavity following [166].

6.1.2.2 Errors limiting the fidelity in temporal multiplexing

The errors limiting the fidelity have two main sources: the spin-waves associated with write photons emitted outside the detection mode, to which I will refer as "undetected spin-waves", and the multiple excitations component in the detection mode. They each give a different contribution to the total error, principally depending of whether they are created in the time-bin of the detected write photon or in another one. Since a required fidelity is necessary in this QR protocol, these errors would ultimately limit the benefit of temporal multiplexing if not dealt with.

Error from spin-waves in the time bin of the detected write photon

Since the write photon emission by Raman scattering is isotropic, each write pulse actually creates several undetected spin-waves associated with write photons emitted outside our detection mode. Let us first consider these undetected spin-waves created in the time-bin of the detected write photon. At the readout time, all the spin-waves created in this specific time-bin will be rephased. The read photons emitted by the readout of the undetected spin-waves will be emitted in the direction opposed to the undetected write photons, and therefore will not be detected either. These events will therefore not contribute to errors.

We can rewrite the two-mode squeezed state of eq. (2.3) for the write-read photon pairs emission as

$$|\phi\rangle = \sqrt{1-p}\sum_{n=0}^{\infty} p^{n/2}\,|n_w, n_r\rangle\,, \tag{6.2}$$

where p is the probability to create at least one photon pair in the detection mode, for each write pulse. Calling n_p the number of created pairs in one trial, we get the following probabilities for the low order terms:

TABLE 6.1: **Event probabilities for a two-mode squeezed state.** $n_p = i$ (resp. $n_p \geq i$) refers to the case where exactly i (resp. at least i) photon pairs have been created in the detection mode.

Events	$n_p = 0$	$n_p = 1$	$n_p = 2$	$n_p \geq 1$	$n_p \geq 2$
Probabilities	$1-p$	$p(1-p)$	$p^2(1-p)$	p	p^2

In the case of a write photon detection, it is not possible to determine the actual number of write photons emitted in our detection mode, and multiple excitations will introduce errors decreasing the fidelity of the created state. We are now interested in the probability to have created more than one pair once we detected one write photon. It is given by

$$p(n_p \geq 2 | n_p \geq 1) = \frac{p(n_p \geq 2 \cap n_p \geq 1)}{p(n_p \geq 1)} = p. \tag{6.3}$$

This effect is also present in the standard DLCZ protocol, and limits the value p depending on the required fidelity of the created state [124].

Error from spin-waves in different time-bins

The undetected spin-waves created in different time-bins will be dephased at the moment of the readout. Hence, the read pulse will emit uncorrelated read photons in random directions, a fraction of which will be detected. Let us call β the fraction of the detected photons, which is given by the solid angle of the detection modes. For the moment, β is assumed to be similar for the write and read photons due to the symmetry of the experimental setup. The mean number of created spin-waves in each time-bin is $\frac{p}{\beta} \gg 1$

typically, giving a total of $(N-1)\frac{p}{\beta}$ dephased spin-waves in average. Since only a fraction β of them will give rise to read photons emitted in the detection mode, the error probability due to these spin-waves is $(N-1)p$. The total two-photon error due to the undetected spin-waves in any time-bin and to the possible multiple excitations is finally $E_{tot} = Np$. Let us call $p^{(N)}$ the spin-wave creation probability per write pulse of a train of N pulses. We see that $p^{(N)} = E_{tot}/N = p^{(1)}/N$. As such, this would strongly limit the advantage of using the multimode protocol as explained in the following.

The requirement on the fidelity of the produced states will give a maximum value for the acceptable two-photon error ϵ, which appears when more than one photon is emitted in the write or read detection modes. This, in turn, limits the value of p, as the condition $E_{tot} = \epsilon$ must be fulfilled. The write photon rate $C^{(N)}$ scales as the write pulses rate multiplied by $p^{(N)}$. According to eq. (6.1), this gives

$$C^{(N)} = \frac{Np^{(N)}}{1+(N-1)/b_t} R_{w,1} = \frac{p^{(1)}}{1+(N-1)/b_t} R_{w,1} = \frac{1}{1+(N-1)/b_t} C^{(1)}. \tag{6.4}$$

In this situation, increasing N actually does not allow to achieve higher photon rates while keeping the error at the level of ϵ. On the contrary, it would even be lowering them, as can be seen in Fig. 6.4.

I will now explain how the introduction of the previously mentioned cavity allows to get around this limit and to effectively increase the write photons rate.

6.1.2.3 Rates increase

The idea is to decrease the error originating from spin-waves in different time-bins by decreasing the mean number of unwanted spin-waves created for each detected write photon, while keeping the fraction of detected non-directional read photons the same. Calling β_w and β_r the fractions of

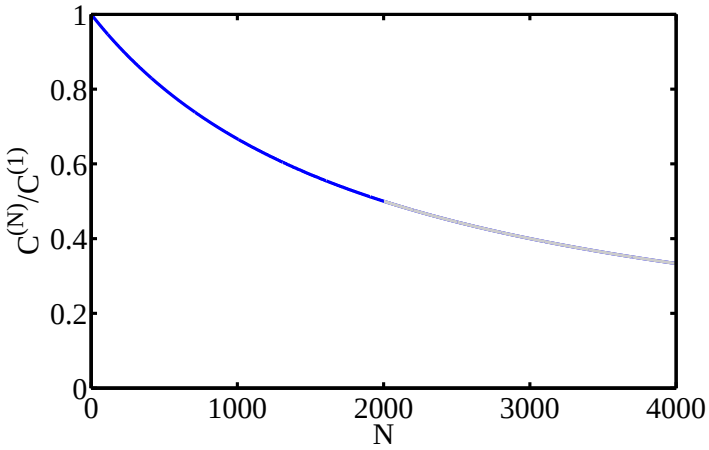

FIGURE 6.4: **Write photons rate gain without cavity.** The write photons rate gain is plotted as a function of the number of pulses per train in the case without cavity, to keep a constant two-photon error. The blue and red lines separate the limit where $N-1=b_t$.

the detected write and read photons, this amounts to get $\beta_w \gg \beta_r$. The solution proposed in [166] to achieve this imbalance is to place the atomic ensemble inside a cavity of finesse F, resonant with the write photons but not with the read photons. On the one hand the emission of the write photons into a cavity mode will be enhanced by a factor F. This will lead to an increase of β_w with respect to the factor β given by the solid angle of the detection mode. On the other hand, due to the non-resonance for the read photons, the dephased ones will not be affected and still be non-directionally emitted, such that β_r remains equal to β. In this case, we obtain that $\frac{\beta_w}{\beta_r} = F$. In addition, the cavity also must be transparent to the read photons emitted in its modes. This is because the correlated read photons retrieved from rephased spin-waves must be able to exit the cavity with high efficiency. This can be achieved by obtaining write and read photons with orthogonal polarizations, and placing a PBS inside the cavity. Let us now explain the influence of such a cavity on the write photons rate.

In this new situation, for each write photon detection, there will be a total of $(N-1)\frac{p}{\beta_w}$ dephased spin-waves. However, the associated error will now

only be of $(N-1)p\frac{\beta_r}{\beta_w} = (N-1)p/F$, which can be made much smaller than $(N-1)p$, the value without the cavity. The total error when a cavity is present is now

$$E_{tot}^{cavity} = p(1+(N-1)/F) = \epsilon. \tag{6.5}$$

We now redefine $p^{(N)} = E_{tot}^{cavity}/(1+(N-1)/F) = p^{(1)}/(1+(N-1)/F)$. The corresponding write photon rate becomes

$$C^{(N)} = \frac{Np^{(N)}}{1+(N-1)/b_t} R_{w,1} = \frac{1}{1+(N-1)/b_t} \frac{N}{1+(N-1)/F} C^{(1)}. \tag{6.6}$$

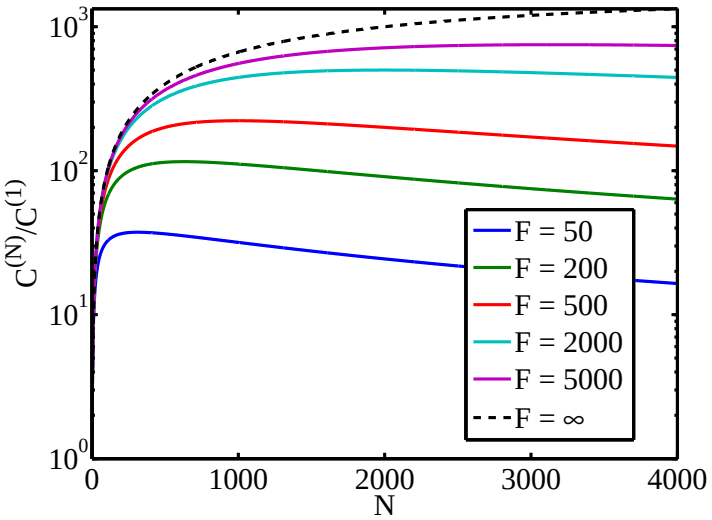

FIGURE 6.5: **Write photons rate gain with a cavity.** Write photons rate gain in log scale as a function of the number of pulses per train in the presence of a cavity, for different cavity finesses, at a constant two-photon error and for $b_t = 2000$. (Dashed line) Asymptotic behavior for infinite finesse.

Comparing eq. (6.4), corresponding to the case without cavity, with the new expression of eq. (6.6), we see that the introduction of the cavity allows a relative photons rate increase of a factor $N/(1+(N-1)/F)$, which tends towards F for large values of N. The write photons rate dependency as a

function of N in the case with the cavity is shown in Fig. 6.5, for different values of the cavity finesse. We see that they follow a linear behavior for low values of N, before reaching a maximum, as illustrated in Fig. 6.6. The left plot is the maximum write photons rate gain as a function of the cavity finesse for a given temporal bandwidth, called $\mathrm{Gain_M}$. The right plot shows $N\,(\mathrm{Gain_M})$, the number of pulses in the train necessary to achieve this optimal gain, expressed as

$$N\,(\mathrm{Gain_M}) = \sqrt{F \cdot b_t - (F + b_t) + 1}, \tag{6.7}$$

which is obtained by nulling the derivative of $C^{(N)}$ defined in eq. (6.6).

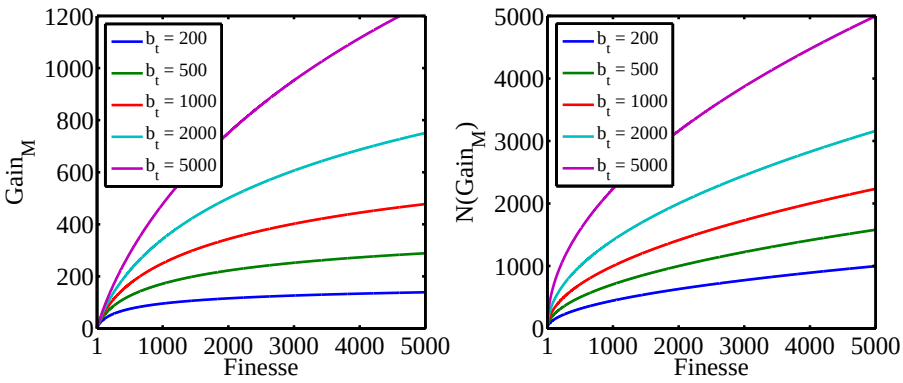

FIGURE 6.6: **Write photons rate gain as a function of cavity finesse, for different values of b_t.** (Left plot) Maximum gain. (Right plot) Number of pulses per train to reach the maximum gain.

As can be seen in Fig 6.6, the maximum gain strongly depends on the temporal bandwidth b_t of the memory. Note that in practice it may be challenging to achieve simultaneously high values of b_t and high cavity finesse, as this would require very small cavities to ensure that the cavity linewidth does not limit b_t.

Another requirement to enable the selective readout capability is that the spin-waves created in different time-bins must be fully temporally distinguishable, which means that each of them must have the time to fully dephase before sending the next write pulse of the train. In this way, only

the spin-waves in a single time-bin will be rephased at the selected readout time. Since the dephasing speed is inversely proportional to the inhomogeneous broadening applied to the atoms, this will limit the minimum delay δt_w between each pulse of the train and in turn the value of N. The write photons duration will never be a limitation, since it follows the temporal shape of the write pulse due to the nature of the Raman scattering process.

6.1.3 Implementation of DLCZ temporal multiplexing

I will now explain how [166] proposed to realize the temporal multiplexing in practice, using CRIB of the spin states. Upon detection of a write photon, the state describing the associated spin-wave is eq. (2.2), which I recall here:

$$|\psi(0)\rangle = \frac{1}{\sqrt{N}} \sum_{j=1}^{N} e^{i\mathbf{x}_j \cdot (\mathbf{k}_W - \mathbf{k}_w)} |g_1 \dots s_j \dots g_N\rangle \,. \tag{6.8}$$

In the absence of any unwanted dephasing mechanism other than atomic motion, the temporal evolution is

$$|\psi(t)\rangle = \frac{1}{\sqrt{N}} \sum_{j=1}^{N} e^{i(\mathbf{x}_j + \mathbf{v}_j t) \cdot (\mathbf{k}_W - \mathbf{k}_w)} |g_1 \dots s_j \dots g_N\rangle \,, \tag{6.9}$$

where $\mathbf{v}_j$ is the velocity of atom j. The controlled dephasing of the spin-wave is realized by the introduction of an inhomogeneous broadening on the atomic states involved in the spin-wave. This introduces an extra dephasing term in the phase factor of the state describing the spin-wave, which becomes

$$|\psi(t)\rangle = \frac{1}{\sqrt{N}} \sum_{j=1}^{N} e^{i \int_0^t \Delta\omega_j(t')dt' + i(\mathbf{x}_j + \mathbf{v}_j t) \cdot (\mathbf{k}_W - \mathbf{k}_w)} |g_1 \dots s_j \dots g_N\rangle \,. \tag{6.10}$$

Here, $\Delta\omega_j(t)$ is the relative detuning of the state associated with atom j in $|s\rangle$, and is different for each atom. We can now reverse this inhomogeneous broadening at a time T_{rev}, such that the extra phase term will cancel when $\int_0^{T_{rev}} \Delta\omega_j(t')dt' + \int_{T_{rev}}^{t} \Delta\omega_j(t')dt' = 0$. If a read pulse is sent at this moment, the spin-wave can be read-out efficiently. Otherwise, it will simply dephase again. In our case, we use a magnetic field gradient produced by the MOT coils to induce this inhomogeneous broadening. However, it could also be induced by other effects such as light-induced ac Stark-shifts [167].

6.2 Controlled rephasing of single collective spin excitations in a cold atomic quantum memory

In this section, I will present our experimental results towards the realization of a temporally multiplexed DLCZ-type quantum repeater node. We demonstrated the first enabling steps, namely the controlled dephasing and rephasing of single spin-waves, together with the selective readout of a single temporal mode. I will first quickly present the experimental setup and the sequence timeline, and then I will show our results before discussing them.

6.2.1 Experimental setup

The experimental setup is shown in Fig. 6.7(a). We initially load the atoms in the MOT, before preparing them in the $|F = 2, m_F = +2\rangle$ Zeeman sublevel. This is because in order to perform the CRIB with magnetic field gradients, we need to use a magnetically sensitive transition. To do so, we shine an optical pumping beam on the $|F = 2\rangle \rightarrow |F' = 2\rangle$ transition together with the read light, both σ^+-polarized, while applying an homogeneous magnetic field along the probing axis in order to lift the degeneracy of the Zeeman levels and to define a quantization axis for the polarizations. In this case, the angle between the pulses and photons detection mode arms is set to 0.95°, and we use the spectral filtering cavities for both the write and the read photons. The write and read pulses are σ^-- and σ^+-polarized in the frame of the atoms, while the detected write and read photons are σ^+- and σ^- respectively, as shown in Fig. 6.7(b). The timeline is shown if Fig. 6.7(c). Each cycle starts with a 15 ms-long MOT loading phase directly followed by a 1.6 ms optical molasses phase and a 10 μs optical pumping phase, during which the magnetic field gradient is switched off. In order to generate an inhomogeneous broadening of the atomic states,

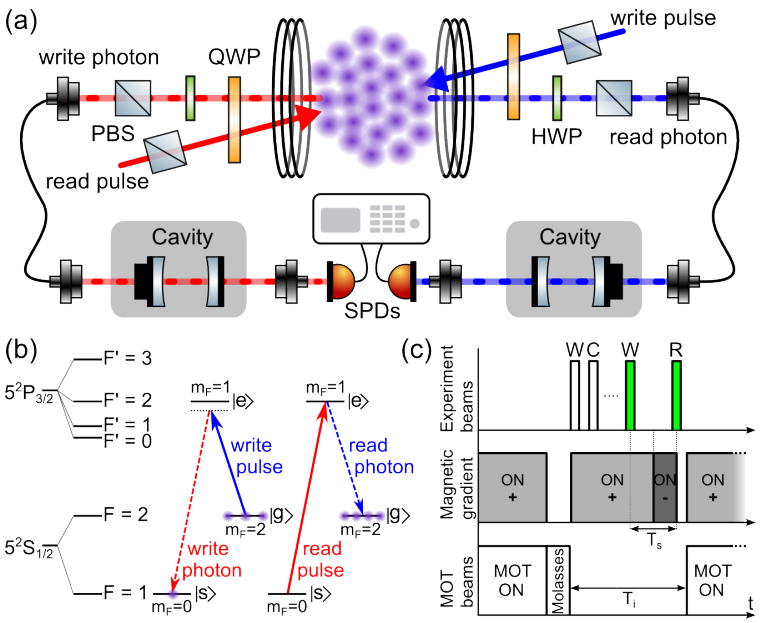

FIGURE 6.7: **Experimental setup for the controlled rephasing experiment.** (**a**) Schematic of the experimental setup. HWP: half-wave plate, QWP: quarter-wave plate, PBS: polarizing beam splitter, SPDs: single photon detectors. (**b**) Energy levels structure. (**c**) Experimental sequence timeline for the active rephasing experiment. W: write pulse, C: cleaning stage, R: read pulse, T_s: storage time, T_i: interrogation time

this magnetic field gradient is then switched on again during the interrogation time, during which up to 200 write pulses, or write pulses pairs depending on the experiment, are sent, followed each time by a cleaning stage. The aim of the cleaning stage is to reset the initial state of the atoms by emptying the atomic population transferred in $|F = 1, m_F = 0\rangle$ by each write pulse, and ideally replacing them in $|F = 2, m_F = +2\rangle$. In case of a successful write photon detection (green event in the timeline), the sign of the magnetic field gradient is reversed and a read pulse is sent after a programmable storage time T_s.

6.2.2 Experimental results

I will now present the experimental results, starting with the case where a single write pulse is sent at each trial.

6.2.2.1 Controlled dephasing and rephasing of single spin-waves

Magnetic field gradient reversal

For this experiment, we used our MOT coils driving circuit described in 3.4.1 to reverse the magnetic field gradient after the detection of a write photon. A trace of the amplitude of this gradient acquired with a Hall probe placed near the science chamber is shown in Fig. 6.8. We observe two different slopes due to the way the circuit operates, as explained in appendix D.

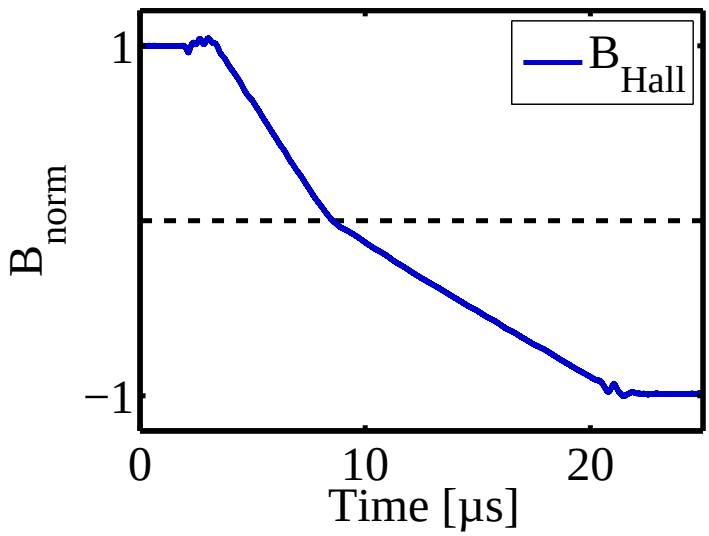

FIGURE 6.8: **Magnetic field gradient reversal.** Normalized amplitude of the magnetic field gradient during the reversal, measured with a Hall probe.

Retrieval efficiency in the standard and controlled rephasing experiments

We use the retrieval efficiency, defined as

$$\eta_{ret}(t) \propto |\langle\psi(0)|\psi(t)\rangle|^2 , \tag{6.11}$$

to monitor the dephasing and rephasing of the spin-waves, which directly represents the temporal evolution of the phase factor. We measure it as $p_{w,r}/p_w$, as previously shown in section 4.2.1.

The results of this experiment are shown if Fig. 6.9. We plot the retrieval

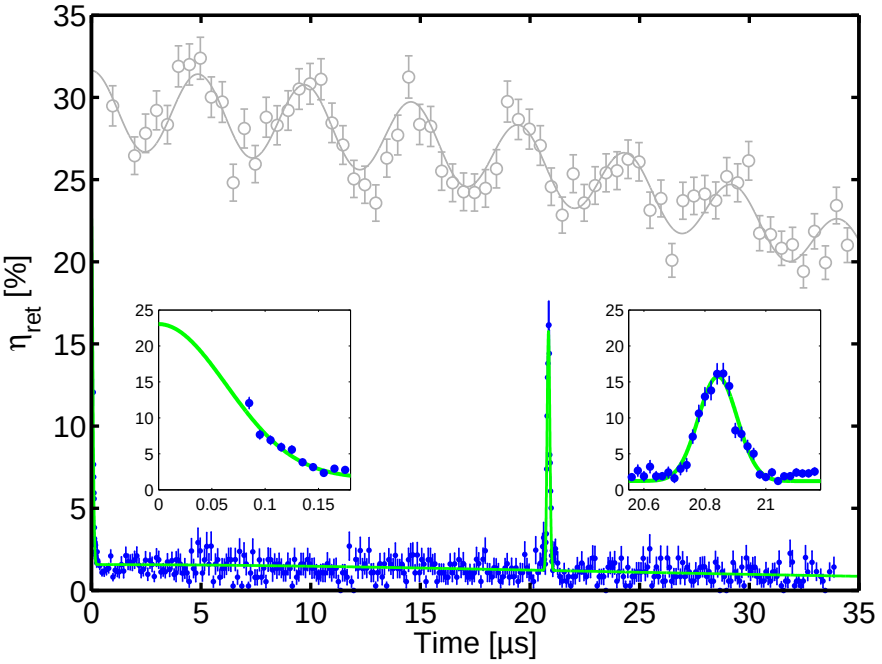

FIGURE 6.9: **Retrieval efficiency vs. readout time.** (Grey open circles) Standard DLCZ experiment. The line is a fit using eq. (6.12). (Blue dots) Controlled rephasing experiment, with the green line as a fit. (Left inset) Zoom on the initial dephasing. (Right inset) Zoom on the rephasing peak. The data are taken with $p_w = 1\%$.

efficiency η_{ret} as a function of time, for the standard DLCZ experiment (grey open circles) and for the controlled rephasing experiment (blue dots and green line).

In the standard DLCZ experiment, we observe oscillations attributed to interferences between two classes of spin-waves. Imperfect optical pumping in $|F = 2, m_F = +2\rangle$ allows some atoms to remain in $|F = 2, m_F = +1\rangle$. The write pulse can then create a spin-wave starting from this latter state and transfer an atom to $|F = 0, m_F = -1\rangle$. These data are fitted with the

formula

$$\eta_{ret_{DLCZ}}(t) = \eta_{0_{DLCZ}} e^{-\frac{t^2}{2\sigma^2_{DLCZ}}} \left| w + (1-w)e^{i2\pi\cdot 2bt} \right|^2 + d. \tag{6.12}$$

Here, $\eta_{0,DLCZ}$ is the retrieval efficiency at zero storage time, with a value of $30.1 \pm 0.3\,\%$. It is corrected for the FFC transmission (0.4) and subsequent fiber coupling (0.5), and detection efficiency (0.43). The weight coefficient w is an indicator of the atomic population distribution between the different Zeeman levels, the parameter b is related to the period of the oscillations due to the bias homogeneous magnetic field, and d is an offset. σ_{DLCZ} is the standard deviation of the temporal Gaussian decay, corresponding to a $1/e$ time constant of the decay in retrieval efficiency equal to $57 \pm 1\,\mu$s. This decay is mainly due to thermal atomic motion and spurious magnetic field gradients. Assuming a Gaussian distribution of the atoms positions and only motional dephasing as explained in section 2.1.4 (see eq. (2.12)), we find

$$\eta_{ret}(t) \propto e^{-\frac{k_B T \Delta k^2 t^2}{m}} = e^{-\frac{t^2}{\tau^2}}, \tag{6.13}$$

with k_B the Boltzmann's constant, $\Delta\mathbf{k} = \mathbf{k}_W - \mathbf{k}_w$, T the temperature of the atoms and m the atomic mass of ^{87}Rb. The corresponding value for T is $180 \pm 6\,\mu$K, which is a higher bound, since other causes such as spurious magnetic gradients could also participate to the observed dephasing. We find $w = 0.957 \pm 0.003$, meaning that $96\,\%$ of the detected correlations arise from atoms in the correct initial state $|F = 2, m_F = +2\rangle$.

In the controlled rephasing experiment, the magnetic field gradient is kept on during the interrogation time. This leads to a rapid dephasing of the spin-wave as seen in the left inset, and the retrieval efficiency vanishes. The magnetic field gradient is then reversed using the circuit described above after the detection of a write photon, leading to the rephasing of the spin-wave and an enhancement of η_{ret} at the rephasing time $T_{reph} = 20.84\,\mu$s, as shown in the right inset. Note that the temporal profile of the rephasing peak is given by the amplitude of the inhomogeneous broadening over

the extent of the atomic cloud, and does not necessary correspond to the temporal shape of the read pulses or photons. In our case, the FWHM of the rephasing profile is $\sim 150\,\mathrm{ns}$ while the one of the read photons is $\sim 20\,\mathrm{ns}$. The data are fitted with the formula

$$\eta_{ret}(t) \propto \left| e^{-\left(\frac{\mu_B \sigma B_0}{\sqrt{2}\hbar}\right)^2 a^2 \left[\ln\left(\cosh\left(\frac{t-t_0}{a}\right)\right) - \ln\left(\cosh\left(\frac{t_0}{a}\right)\right)\right]^2} \right|^2, \tag{6.14}$$

obtained by combining equations (6.8), (6.10) and (6.11). This formula corresponds to the phase factor while not considering atomic motion. We correct it by multiplying it with the Gaussian envelope of the standard DLCZ experiment data, and by a Lorentzian decay representing a slow temperature drift of the FFC's temperature, leading to a decrease in transmission efficiency over the experiment time.

We observe a reduction in the retrieval efficiency at T_{reph} with respect to the Gaussian envelope of the standard DLCZ experiment. The maximum efficiency for the fit in the controlled rephasing experiment corresponds to 56% of this Gaussian envelope at the same storage time. However, for the fit of the controlled rephasing data, part of the reduction in efficiency is due to the FFC temperature drift, which was not present in the standard DLCZ experiment due to the much shorter duration necessary for the data acquisition. If we don't take the Lorentzian decay into account, the relative efficiency increases to 73%.

To understand the decrease in efficiency in the rephasing experiment, we use the following model for the rephasing curve. We approximate the temporal behavior of the magnetic field gradient as a negative hyperbolic tangent with a measured amplitude $B_0 = 20\,\mathrm{G/cm}$ (see Appendix D). The only unknown parameter is σ, corresponding to the standard deviation of the Gaussian spatial profile of the atomic cloud. A fluorescence measurement with a CCD camera gives a FWHM of 2.2 mm for the size of the cloud. Back-propagating this value into eq. (6.14) yields a FWHM for the rephasing peak of 100 ns. However, the measured width of the rephasing peak's temporal profile is $150 \pm 3\,\mathrm{ns}$.

The discrepancy between these two values, together with a reduction in the efficiency, can be attributed to several effects. The main effect is probably fluctuations in the rephasing time T_{reph}. In an ideal case with a perfectly symmetric inversion of the current in the coils, only the FWHM should vary. However, due to the way our coils current driver circuit works, T_{reph} also depends on the current flowing in the coils. Such current fluctuations have two causes. The first one is temperature fluctuations of the coils, leading to current fluctuations, because we run the power supply in voltage source mode. The second reason are shot-to-shot fluctuations, due to the fact that we employ an external high-voltage source for the coils loading.

On the one hand, we measured a linear dependency of T_{reph} with the coils current around our usual operating value of 7 A. We observed a drift of T_{reph} of 2 ns per milliampere change in the current. On the other hand, we simulated the resulting averaged temporal shape of many identical Gaussians with a fluctuating mean value, as shown in Fig. 6.10. As a starting point, we construct an initial Gaussian with a FWHM of 100 ns. The fluctuations of the mean values are taken as a uniform distribution with a range of ± 70 ns around the original value. Averaging over 10^3 realizations results in an approximate Gaussian profile of ~ 150 ns FWHM and 68% relative efficiency. This demonstrates that the observed rephasing shape can be explained to a great extent by fluctuations in the coils current of the order of 1%.

Signal-to-noise ratio of the rephasing peak

We measured the SNR at the rephasing time. It is calculated as the maximum efficiency of the fit at the rephasing time, divided by the averaged background efficiency. In the case of the data shown in Fig. 6.9, we obtain $SNR = 13.3 \pm 0.9$. Its value also depends on p_w, as can be seen in Fig. 6.11. An interesting observation is that although the SNR displays a similar behavior to the on of $g^{(2)}_{w,r}$ as a function of p_w, they have different values. This can be seen by expressing them in terms of probabilities. On

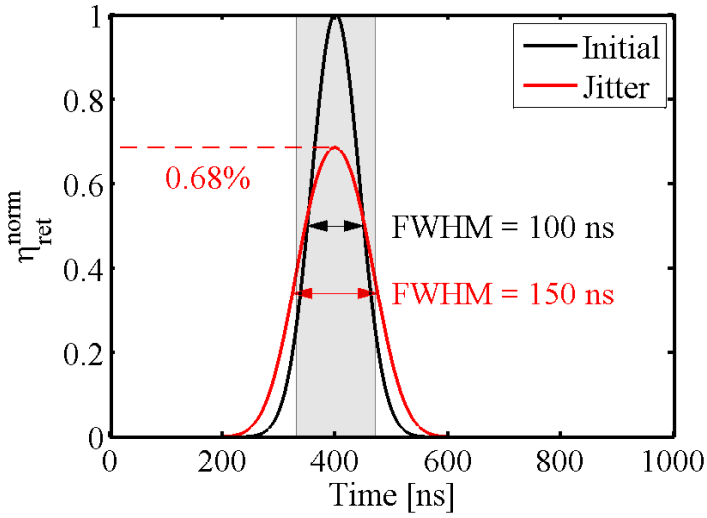

FIGURE 6.10: **Effect of mean value fluctuations on a Gaussian distribution.** (Black line) Initial Gaussian with a FWHM of 100 ns. (Red line) Average of 10^3 realizations with a mean value jitter of ± 70 ns corresponding to the grey shaded area. The resulting distribution is approximately a Gaussian with a FWHM of $\sim$ 150 ns and a relative efficiency of 68%.

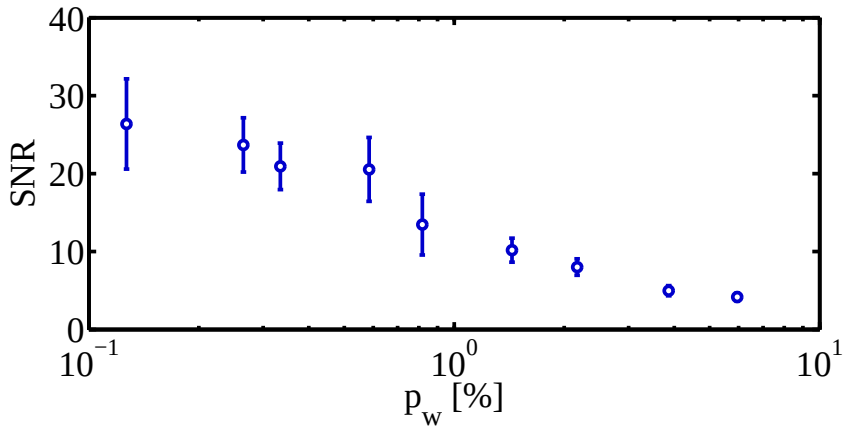

FIGURE 6.11: **Signal-to-noise ratio at the rephasing time.** The value of the SNR varies with p_w, reaching up to 26.4±5.8 for $p_w = 0.13\%$.

the one hand,

$$g^{(2)}_{w,r} = \frac{p_{w,r}}{p_w \cdot p_r} = \frac{\eta_{ret}}{p_r}. \tag{6.15}$$

On the other hand, as we define it,

$$SNR = \frac{\eta_{ret}}{\eta_{ret}^{back}}, \tag{6.16}$$

with η_{ret}^{back} the efficiency in the background. It is expressed as $\eta_{ret}^{back} = \frac{p_{w,r}^{back}}{p_w}$, with $p_{w,r}^{back}$ the probability to detect a coincidence outside of the rephasing peak. Since in this case, all the spin-waves are dephased, those are only accidental coincidences, so $p_{w,r}^{back} = p_w \cdot p_r^{back}$, and $\eta_{ret}^{back} = p_r^{back}$, with p_r^{back} the probability to detect a read photon in the background. When all the spin-waves are dephased, the situation is similar to the one of the standard DLCZ experiment presented in the second part of section 4.2.2. There, we saw that p_r is decreasing when the storage time increases, reaching a minimum for long storage times, when the spin-waves are fully dephased (see Fig. 4.12). As a consequence, $p_r^{back} < p_r$. Combining equations (6.15) and (6.16) after the previous simplifications results in

$$\frac{g_{w,r}^{(2)}}{SNR} = \frac{p_r^{back}}{p_r} < 1. \tag{6.17}$$

Therefore, the value of $g_{w,r}^{(2)}$ is always lower than the one of the SNR.

Auto-correlation measurement at the rephasing time

We investigated on the single-photon nature of the retrieved read photons at the rephasing time. To do so, we modified the setup by preparing a Hanbury-Brown and Twiss interferometer. This allows us to measure the conditional auto-correlation function of the read photons $\alpha_{r,r}$ (see section 2.1.5), also called anti-bunching parameter in the case of non-classical fields where it takes values below one. We measured the values of $\alpha_{r,r}$ as a function of p_w, as shown in Fig. 6.12. The fit is based on eq. (2.26). This equation is obtained for a perfect two-mode squeezed state, and is valid for ideal values of $\alpha_{r,r}$ and $g_{w,r}^{(2)i}$. In order to account for various experimental imperfections, we assume that the measured values of the cross-correlation function $g_{w,r}^{(2)m}$ are lower but proportional to the ideal

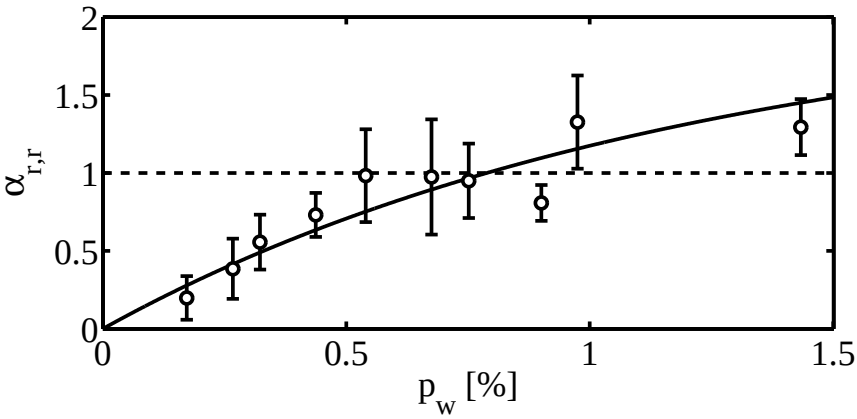

FIGURE 6.12: **Anti-bunching parameter of the read photons at the rephasing time.** The values of $\alpha_{r,r}$ are plotted as a function of p_w, reaching values as low as 0.20 ± 0.14 for $p_w 0.17\%$. (Solid line) Fit of the experimental data. (Dashed line) Lower limit of one for classical states.

ones, such that $g^{(2)m}_{w,r} = c \cdot g^{(2)i}_{w,r}$ with $c < 1$. We can the express the measured value of $\alpha^m_{r,r}$ as a function of $g^{(2)m}_{w,r}$, leading to (see Appendix A)

$$\alpha^m_{r,r} = \frac{4}{g^{(2)m}_{w,r}} - \frac{2}{\left(g^{(2)m}_{w,r}\right)^2} = \frac{4}{c}\frac{p}{1+p} - \frac{2}{c^2}\left(\frac{p}{1+p}\right)^2. \tag{6.18}$$

We derive the values of p from the ones of p_w, knowing the transmission losses and detection efficiency. Eq. (6.18) is used to fit the data of Fig. 6.12. We see that for sufficiently low values of p_w, the retrieved photons exhibit anti-bunching, which is a proof of non-classicality.

After this characterization of the controlled dephasing and rephasing of single spin-waves, I will now show the results obtained when sending two write pulses in different temporal modes.

6.2.2.2 Controlled dephasing and rephasing of multiple spin-waves

We now send two write pulses separated by 600 ns, first independently and then jointly, before sending the read pulse. The read-out time is scanned around the rephasing time. Fig. 6.13 (a) shows the coincidence probabilities per trial $p_{w,r}$ when each write pulse is send independently.

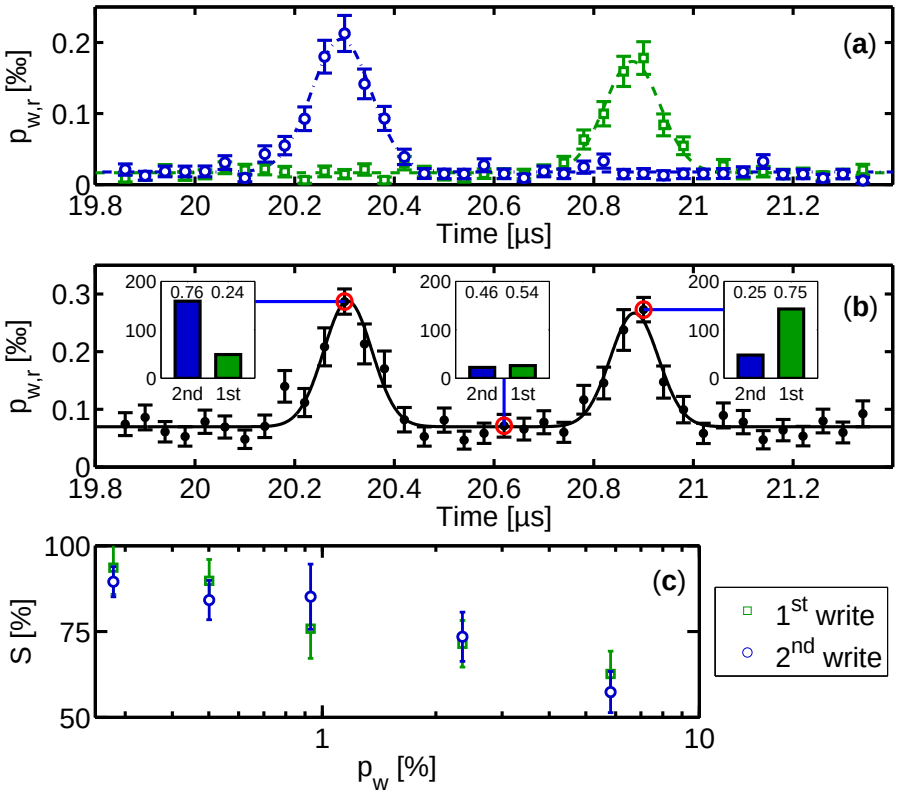

FIGURE 6.13: **Multiple write pulses creating spin-waves in separated time-bins.** (**a**) Single rephasing case for $p_w = 1\%$: first write pulse in green, second write pulse in blue. (**b**) Both pulses sent in black. The histograms display the relative weight of each peak, at the circled points. (**c**) Selectivity as a function of p_w for each rephasing.

The readout time is defined as the time between the first write pulse and the read pulse. As expected, the spin-wave created by the first write pulse (green data) rephases later, while the one created by the second write pulse

rephases earlier (blue data). Fig. 6.13 (b) shows the coincidence probability when both write pulses are sent conjointly. The values at the maximum of the rephasing peaks are similar, when background-subtracted. However, the probability to detect an accidental coincidence in the background (outside the rephasing peaks) is higher in this case, which will lead to lower $g^{(2)}_{w,r}$ and fidelity, as explained in section 6.1.2.2. This can be explained by expressing the coincidence probability in the background as $p_B = p_w \cdot p_r$. Noting that $p_r \propto p_w$ [162], one gets $p_B \propto p_w^2$. In the case where we send two write pulses, the write detection probability p_{2w} is twice the one of the single write pulse case p_w. Therefore, the background probability for two write pulses becomes $p_B^{(2)} \propto p_{2w}^2 = 4 \cdot p_w^2$. This factor of 4 is compatible with the measured value of 4.1 ± 0.3 from our data. This is also consistent with the discussion on the error originating from multiple spin-waves presented in section 6.1.2.2. In our data, the noise probability increases as the square of the number of temporal modes, $p_B^{(N)} \propto N^2$. However, the error can be defined as $E = \text{noise}/(\text{signal} + \text{noise}) \sim \text{noise}/\text{signal}$. The signal is also increasing with N, such that we find back that the error increases linearly with N.

To investigate the cross-talk between the two spin-waves, we construct the histograms shown in the insets of Fig. 6.13 (b) by performing start-stop measurements. The starts are write photon detections, and the stops are read photon detections. The two contributions are equally weighted in the noise region, but on each rephasing peak, we detect a significant imbalance. This shows that mostly only one spin-wave rephases at a time. To quantify the process, we calculate the relative weight of each peak, which we call selectivity: $S(i) = p_{C,i}/\sum_k p_{C,k}$, with $p_{C,i}$ the probability to detect a coincidence in the binning corresponding to the peak number i. Its value depends on the rephasing SNR which varies with p_w (see Fig. 6.13 (c)). For the results shown in Fig. 6.13 (b) we find an average selectivity $S = (S(1) + S(2))/2 = 76 \pm 6\%$. For the lowest $p_w = 0.28\%$ shown in Fig. 6.13 (c), we obtain an average selectivity of $92 \pm 4\%$.

The results of Fig. 6.13 show that when several spin-waves are created, the rephasing efficiency of each one remains the same, but the background noise increases. With the current status of the experiment, this limits the benefit of multiple temporal mode storage, since the excitation probability needs to be reduced for each pulse in order to keep the same SNR. However, as explained in the previous section of this chapter, this issue is addressed in the scheme proposed in [168].

We expect that the rephasing time T_{reph} should be symmetrical from the write pulse time with respect to the magnetic field gradient reversal time T_{rev}. First, this is confirmed by the fact that the separation of 600 ns between the two rephasing peaks of Fig. 6.13 is equal to the separation between the two write pulses. Second, we also measured T_{reph} as a function of T_{rev}, which in this case is defined as the delay between the center of the write photon, and the moment when the reversal instruction is sent in the experimental sequence. This measurement is shown in Fig. 6.14. The data are fitted with a linear function, and we find

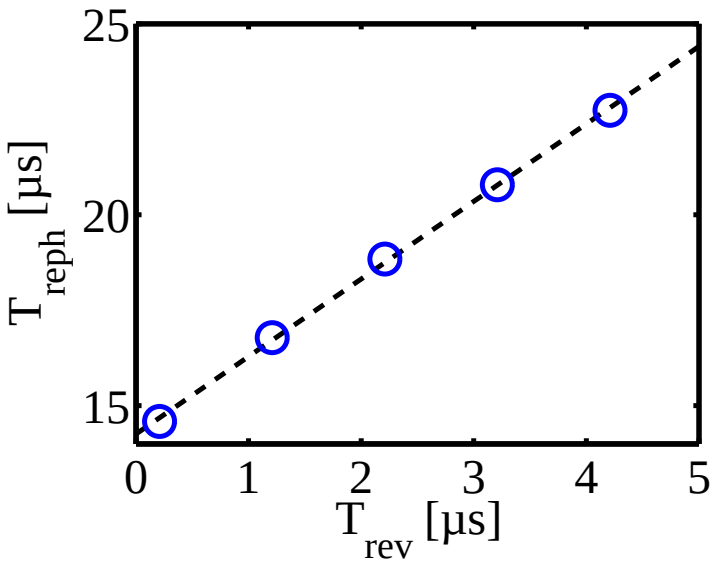

FIGURE 6.14: **Rephasing time as a function of the magnetic field gradient reversal time.** Open circles: data points. Dashed line: linear fit.

$T_{reph} = (2.03 \pm 0.04) \cdot T_{rev} + T_0$. The proportionality factor of nearly 2 is consistent with the expected behavior. We find a value of $14.26\,\mu$s for T_0, which corresponds to the minimum rephasing time when the magnetic field gradient is reversed at the exact same time of a write photon detection. This time is limited by the charge and discharge time of the MOT coils allowed by our current driver.

Finally, we studied the width of the rephasing profile for several durations of the write pulse, which are translated in the durations of the write photons, as shown in Fig. 6.15. The magnitude of the inhomogeneous broadening applied to the atomic ensemble defines a minimal width for the rephasing profile in our experiment. We expect the shape of the measured rephasing to be the convolution of the write and read photons temporal modes, and of that magnetically induced rephasing profile. In this case, the duration of the write and read pulses should be short compared to the rephasing profile in order to maximize the retrieval efficiency at the rephasing time. To verify this, we measured the retrieval efficiency as a function of the storage time for several write pulse durations. Longer write pulses give rise to longer rephasing profiles with lower maximum efficiency, which is consistent with our expectations.

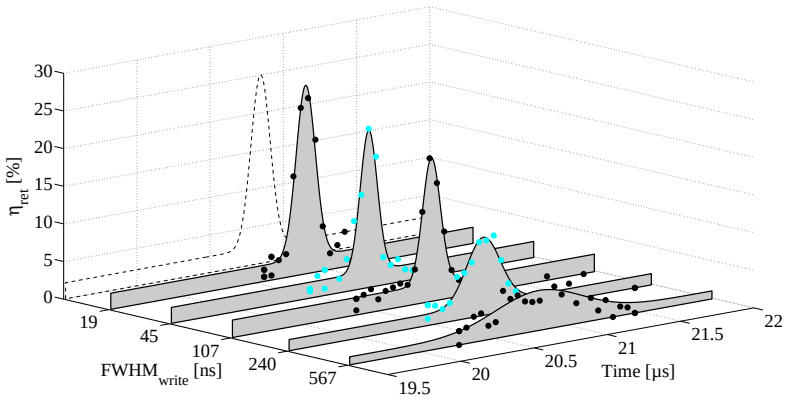

FIGURE 6.15: **Temporal shape of the measured rephasing profile for several write pulse durations.** Blue and black dots: data points. Blue and grey surfaces: Gaussian fits.

In conclusion, we demonstrated active rephasing of a single spin-wave at a controllable time by inverting the polarity of an external inhomogeneous broadening created by a magnetic gradient. We showed that in this case, the retrieved photons still exhibit anti-bunching, which proves that active rephasing preserves single photons statistics. Finally, we demonstrated experimentally that this technique enables the creation of a spin-wave in multiple time-bins that can be read-out individually with high selectivity. These results pave the way towards the realization of a temporally multiplexed DLCZ-type quantum repeater node.

Chapter 7

Conclusion and future directions

7.1 Summary of my PhD work

The goal of my PhD thesis work was to implement a proof of principle experiment towards the realization of a functional temporally multiplexed quantum repeater node based on the DLCZ protocol [15]. We focused on two important properties for such systems. The first one is the demonstration of the multimode capability of a DLCZ quantum memory at the single excitation level. The second one is to enable the connection of this type of quantum repeater node to the telecom c-band via ultra-low noise quantum frequency conversion, in view of future integration in the existing telecom fiber network.

The first important step was the entire design and building of the cold atom trap used for the rest of the experiments. This includes mainly the vacuum chamber and the magnetic coils' driving circuit, together with the laser system for atom trapping and probing. We then implemented a DLCZ-type quantum memory protocol using cold ^{87}Rb atoms in a magneto-optical trap. Our DLCZ quantum memory is capable of producing highly non-classically correlated photon pairs, together with a reasonable retrieval efficiency and memory lifetime. The measured second-order auto-correlation function reached up to 200, the inferred intrinsic retrieval efficiency inside the science chamber up to 44%, and the longest memory lifetime was 55 μs. In parallel, the quantum frequency conversion experiment has been designed and built by other members of the group. We performed and experiment on quantum frequency conversion of weak coherent pulses compatible with cold atomic quantum memories. For this, we verified that light with a frequency and bandwidth allowing it to interact with the ^{87}Rb atoms was converted, and that the process was preserving the coherence of a time-bin qubit. We also showed that the device could operate at the single photon level, and demonstrated a signal-to-noise ratio of 1.3 for a mean input photon number $\mu_{in} = 1$.

Afterwards, we used the DLCZ quantum memory in combination with the quantum frequency conversion setup. The quantum memory was used as

an heralded single photon source, connected at the input of the quantum frequency conversion device. The detection of write photons was triggering the readout of the memory followed by the detection of the converted read photons. The performances of the quantum frequency conversion device in terms of device efficiency and noise suppression have been improved enough to significantly increase the signal-to-noise ratio, reaching up to 80 for $\mu_{in} = 1$. This allowed us to show the preservation of the non-classical nature of the correlations between the write and converted read photons, via the violation of the Cauchy-Schwarz inequality.

Finally, we investigated the multimode capability of the DLCZ quantum memory. Our goal was to show that a spin-wave could be created in the atomic ensemble in multiple temporal modes, and that only a single one of these could be read-out at a specific later time. This constitutes the building block for the temporal multiplexing protocol proposed in [166]. First, we used the controlled and reversible inhomogeneous broadening technique to demonstrate active dephasing and then rephasing of a single spin-wave. The inhomogeneous broadening was generated by the magnetic coils of the MOT. The magnetic field was applied during the write process, before being reversed after the complete dephasing of the spin-wave, leading to a rephasing at a later and controllable time. The retrieval efficiency was used in order to assess the phase of the spin-wave. We then showed that in this case, the retrieved photons still exhibit anti-bunching, which proves that non-classical photon statistics can be preserved by this active rephasing technique. We also made sure that the rephasing time was dependent on the delay between the write process and the reversal time of the magnetic field gradient. Second, we performed a similar experiment while sending two consecutive temporally-separated write pulses. In this way, the spin-wave was created in two temporal modes. We verified that in this new situation, the retrieval efficiency was similar to the previous one. We then demonstrated the possibility to selectively read-out only one out of the two temporal modes, with a selectivity up to 92%. In this way,

non-classical correlations between the write and read photons are observed only if their two temporal modes are matched with each other.

All these results pave the way towards the realization of future temporally multiplexed quantum repeater nodes based on the DLCZ protocol.

7.2 Future directions

7.2.1 Improving the performances of the quantum memory

A general objective is to continue the optimization work of the quantum memory. The retrieval efficiency could be improved by better mode matching between the excitation and detection modes, together with the implementation of more advanced atom trapping and cooling schemes allowing to reach higher optical depth. The storage time could be increased via the obtention of a colder atomic cloud, and by creating spin-waves on magnetically-insensitive clock transitions in the single-mode case. If CRIB has to be implemented, one can use a passive magnetic shielding around the science chamber in order to strongly reduce spurious magnetic field gradients. Loading the atomic cloud in an optical lattice [169] and using a collinear configuration [120] can also be used to eliminate motional dephasing. Finally, the values of the auto-correlation function could be increased at low excitation powers by using single photon detectors with lower dark counts rates.

Following the quantum frequency conversion's line of work, conversion of the write photons followed by characterization of the correlations is planned. This would lead to non-classical correlations between a telecom C-band photon and a long-lived spin-wave, as required for the DLCZ protocol.

7.2.2 Temporally multiplexed quantum memory

Work on the temporal multiplexing project is still ongoing. The next step will be to include an optical cavity in the quantum memory setup, in order to fully implement the temporal multiplexing proposal of [166]. This cavity will be of moderate finesse, resonant with the write photons and invisible to the read photons. It will be challenging to achieve a high finesse with the current setup, because the cavity will have to be placed outside of the science chamber. However, similar cavities with moderate finesses have been already built for DLCZ experiments in other groups [16, 117, 120]. With this modified setup, it will then become possible to create spin-waves in many more temporal modes, up to the finesse of the cavity, without decreasing the quality of the non-classical correlations between the photons pairs. If successful, this will be the first experimental realization of a functional temporally-multiplexed DLCZ quantum repeater node.

7.2.3 Temporal shaping of single photons

Temporal shaping of the heralded read photons is currently investigated. The goal of this experiment is to enable the connection between our DLCZ quantum memory, used as a heralded single photon source, and other quantum systems of different types, which may have specific bandwidth requirements. In this way, it will become possible to integrate such quantum memories within future heterogeneous quantum networks. Single heralded read photons with a Gaussian temporal profile exhibiting a FWHM duration ranging from $\sim 20\,\mathrm{ns}$ up to $\sim 10\,\mu\mathrm{s}$ could be generated. This feature will be used to connect our DLCZ quantum memory with two other quantum memory experiments developed in the QPSA group. It could also be used to connect atomic ensembles quantum memories to single ions [170]. Photons with a rising exponential temporal profile could be generated as well, which is optimal for absorption by single atoms or ions [171] and can also be advantageous for absorption in atomic ensembles [172].

7.2.4 Collaboration with other projects in the group

Our experimental setup in its current state will be used as a heralded singe photon source in combination with two other experiments done by different members of the QPSA group. One is a Rydberg electromagnetically-induced transparency (EIT) quantum memory in a cold ^{87}Rb atomic ensemble. The second one is an atomic frequency comb (AFC) quantum memory in a praseodymium-doped crystal.

Connection to the Rydberg EIT quantum memory

Heralded single read photons will be sent to the Rydberg EIT quantum memory. In order to do so, the bandwidth of the read photons must match the one of the EIT quantum memory, which is typically $\sim 1.5\,\mathrm{MHz}$, corresponding to a duration of $\sim 300\,\mathrm{ns}$ for Fourier-transform-limited Gaussian photons. These photons will then be retrieved, and cross-correlation measurements between the write and retrieved read photons after Rydberg EIT storage will be performed. Studying the behavior of the single photons statistics and of the cross-correlation function between the write and read photons after passing through a Rydberg-blockaded ensemble is also of interest.

Connection to the AFC quantum memory

Further work about QFC is on progress in our group, with the objective of connecting the DLCZ quantum memory to a separate solid-state based quantum memory operating at 606 nm. The idea is to convert heralded read photons from 780 to 606 nm via two consecutive quantum frequency conversion stages. This experiment would be the first proof of principle of a hybrid quantum network segment able to connect a cold-atomic and a solid-state quantum memory. The DLCZ quantum memory will be used as an heralded single photon source for this project. The bandwidth of the heralded read photons will have to be matched with the AFC bandwidth,

which is typically 3 MHz, corresponding to a duration of $\sim$ 140 ns for Fourier-transform-limited Gaussian photons.

7.2.5 Developments in the field of quantum communications

In order to build large-scale quantum repeaters, one requires scalable, rapid and efficient quantum repeater nodes capable of producing and storing high-purity entangled photons pairs and of performing entanglement swapping operations with high fidelity.

A promising platform in terms of efficiency and scalability is the coupling between cold atoms and nanofibers. Trapping atoms around a nanofiber with a sub-wavelength diameter by means of a nano-scale potential created with evanescent light fields allows strong interaction with light guided in the fiber. This allows one to achieve very high optical depth with very few atoms [173]. Since the light remains confined in the fiber, the coupling with different systems will be excellent. Such systems could be used to engineer quantum states useful for precision measurements and quantum information [174] and to realize optical quantum memories [175–177]. Spatial multiplexing could be investigated by placing several nanofibers inside a single atomic ensemble.

Scalability includes multiplexing and miniaturizing aspects. Besides the temporal multiplexing explored in this thesis, spatial multiplexing can be achieved with cold atomic ensembles by addressing several spatial modes in the same atomic cloud [178]. The miniaturization is potentially more demanding due to the need of ultra-high vacuum chambers. However, very compact and functional experimental setups are commercially available. An alternative approach is to use room-temperature vapor cells. Their strong advantage is that they can present a reduced centimeter-scale size. However, they usually have strong limitations with respect to the memory lifetime due to thermal motion of the atoms. A solution to this issue

has been proposed recently [179], where the concept of motional averaging could enable room temperature discrete variable quantum memories and coherent single photon sources.

The practical realization of a quantum repeater able to distribute entanglement over large distance would be a major achievement in the field of quantum information, and would open new opportunities for quantum key distribution and future quantum networks. However, although initial steps have been taken (including in this thesis), the realization of such a practical quantum repeater is still a distant goal, and will probably require improved quantum memories and a combination of several of the techniques described above.

Appendix A

Cross-correlation function $g^{(2)}_{w,r}$ and anti-bunching parameter α calculations

In this appendix, I will detail the derivation of the expressions of the second order cross-correlation function $g^{(2)}_{w,r}$ and the anti-bunching parameter α as a function of p, obtained in Ch. 2. Here, p is the probability to create one or more spin-wave or write/read photon pair per write pulse, appearing in the two-mode squeezed state which I recall in the photon pairs case:

$$|\Psi\rangle = \sqrt{1-p}\left(\sum_{n=0}^{\infty} p^{n/2}\,|n_w, n_r\rangle\right). \tag{A.1}$$

A.1 Cross-correlation function $g^{(2)}_{w,r}$

By definition,

$$g^{(2)}_{w,r} = \frac{p_{w,r}}{p_w \cdot p_r} = \frac{\left\langle : a_w^\dagger a_w a_r^\dagger a_r : \right\rangle}{\left\langle : a_w^\dagger a_w : \right\rangle \cdot \left\langle : a_r^\dagger a_r : \right\rangle} = \frac{\left\langle a_w^\dagger a_r^\dagger a_r a_w \right\rangle}{\left\langle a_w^\dagger a_w \right\rangle \cdot \left\langle a_r^\dagger a_r \right\rangle}, \tag{A.2}$$

where the : symbol denotes the normal ordering of the photon operators, which commute between each other.

Let us start by evaluating the mean photon number in the write mode $\left\langle a_w^\dagger a_w \right\rangle$, which can be rewritten as

$$\left\langle \psi | a_w^\dagger a_w | \psi \right\rangle = \left| a_w \left| \psi \right\rangle \right|^2 . \tag{A.3}$$

Applying the write photon annihilation operator to the state of Eq. (A.1) yields

$$a_w \left| \psi \right\rangle = \sqrt{1-p} \left(\sum_{n=0}^{\infty} p^{n/2} \sqrt{n} \left| (n-1)_w, n_r \right\rangle \right), \tag{A.4}$$

hence

$$\left| a_w \left| \psi \right\rangle \right|^2 = (1-p) \left(\sum_{n=0}^{\infty} p^n n \right) = (1-p) \frac{p}{(1-p)^2} = \frac{p}{1-p}. \tag{A.5}$$

By symmetry of the two-mode squeezed state and the $g^{(2)}_{w,r}$, we obtain the same expression for the mean read photons number, such that

$$\left\langle a_w^\dagger a_w \right\rangle = \left\langle a_r^\dagger a_r \right\rangle = \frac{p}{1-p}. \tag{A.6}$$

Proceeding in a similar way for the mean coincidences number $\left\langle a_w^\dagger a_r^\dagger a_r a_w \right\rangle$, we obtain

$$a_r a_w \left| \psi \right\rangle = \sqrt{1-p} \left(\sum_{n=0}^{\infty} p^{n/2} \sqrt{n} \sqrt{n} \left| (n-1)_w, (n-1)_r \right\rangle \right), \tag{A.7}$$

hence

$$\left| a_r a_w \left| \psi \right\rangle \right|^2 = (1-p) \left(\sum_{n=0}^{\infty} p^n n^2 \right) = (1-p) \frac{p(1+p)}{(1-p)^3} = \frac{p(1+p)}{(1-p)^2}. \tag{A.8}$$

Combining equations (A.2), (A.6) and (A.8) we obtain the following expression

$$g^{(2)}_{w,r} = \frac{\frac{p(1+p)}{(1-p)^2}}{\left(\frac{p}{1-p}\right)^2} = 1 + \frac{1}{p}. \tag{A.9}$$

A.2 Anti-bunching parameter α

The definition of α is [152]

$$\alpha = \frac{p_{(r_1,r_2|w)}}{p_{(r1|w)} \cdot p_{(r2|w)}} = \frac{p_{w,r_1,r_2} \cdot p_w}{p_{w,r_1} \cdot p_{w,r_2}}. \tag{A.10}$$

Here, r_1 and r_2 are the two read photonic modes after sending the initial mode through a 50/50 beamsplitter. We can then express α in terms of the photonic annihilation and creation operators

$$\alpha = \frac{\left\langle a^\dagger_w a^\dagger_{r_1} a^\dagger_{r_2} a_{r_2} a_{r_1} a_w \right\rangle \cdot \left\langle a^\dagger_w a_w \right\rangle}{\left\langle a^\dagger_w a^\dagger_{r_1} a_{r_1} a_w \right\rangle \cdot \left\langle a^\dagger_w a^\dagger_{r_2} a_{r_2} a_w \right\rangle}. \tag{A.11}$$

We rewrite the two-mode squeezed state as

$$|\Psi\rangle = \sqrt{1-p} \left(\sum_{n=0}^{\infty} p^{n/2} \frac{1}{\sqrt{n!}} (a^\dagger_r)^n \, |n_w, 0_r\rangle \right). \tag{A.12}$$

In the case where the read photonic mode is sent through a 50/50 beamsplitter, this formula becomes

$$|\Psi\rangle = \sqrt{1-p} \left(\sum_{n=0}^{\infty} p^{n/2} \frac{1}{\sqrt{n!}} \left(\frac{a^\dagger_{r_1} + i a^\dagger_{r_2}}{\sqrt{2}} \right)^n |n_w, 0_{r_1}, 0_{r_2}\rangle \right), \tag{A.13}$$

which can be rewritten as

$$|\Psi\rangle = \sqrt{1-p} \left(\sum_{n=0}^{\infty} \left(\frac{p}{2}\right)^{n/2} \sum_{j=0}^{n} i^j \sqrt{\frac{n!}{j! \cdot (n-j)!}} \, |n_w, (n-j)_{r_1}, j_{r_2}\rangle \right). \tag{A.14}$$

Evaluating the terms of Eq.(A.11) with this state, one gets

$$\left\langle \Psi \left| a_w^\dagger a_w \right| \Psi \right\rangle = \left| a_w \left| \Psi \right\rangle \right|^2 = \frac{p}{1-p}, \tag{A.15}$$

$$\left\langle \Psi \left| a_w^\dagger a_{r_1}^\dagger a_{r_1} a_w \right| \Psi \right\rangle = \left| a_{r_1} a_w \left| \Psi \right\rangle \right|^2 = \frac{p(1+p)}{2(1-p)^2}, \tag{A.16}$$

$$\left\langle \Psi \left| a_w^\dagger a_{r_2}^\dagger a_{r_2} a_w \right| \Psi \right\rangle = \left| a_{r_2} a_w \left| \Psi \right\rangle \right|^2 = \frac{p(1+p)}{2(1-p)^2}, \tag{A.17}$$

$$\left\langle \Psi \left| a_w^\dagger a_{r_1}^\dagger a_{r_2}^\dagger a_{r_2} a_{r_1} a_w \right| \Psi \right\rangle = \left| a_{r_2} a_{r_1} a_w \left| \Psi \right\rangle \right|^2 = \frac{p^2(2+p)}{2(1-p)^3}. \tag{A.18}$$

Finally, combining equations (A.11), (A.15), (A.16), (A.17) and (A.18) we obtain the following expression

$$\alpha = \frac{\left\langle a_w^\dagger a_w \right\rangle \cdot \left\langle a_w^\dagger a_{r_1}^\dagger a_{r_2}^\dagger a_{r_2} a_{r_1} a_w \right\rangle}{\left\langle a_w^\dagger a_{r_1}^\dagger a_{r_1} a_w \right\rangle \cdot \left\langle a_w^\dagger a_{r_2}^\dagger a_{r_2} a_w \right\rangle} = \frac{2p(2+p)}{(1+p)^2}. \tag{A.19}$$

Appendix B

Physical processes in a MOT

B.1 Doppler cooling

Doppler cooling derivation

Doppler cooling of neutral atoms was proposed in 1975 by Hänsch and Schawlow [180], and the first optical molasses has been realized in 1985 by Chu and coworkers, allowing them to cool sodium atoms down to a temperature of about 240 μK. It is based on the Doppler effect, which changes the frequency of a wave for an observer moving relative to its source. This effect can directly be applied to moving atoms illuminated by laser beams. When an atom is moving with a velocity $\mathbf{v}$, it will only be able to absorb photons which are detuned from its resonant frequency at rest ω_0. A counter-propagating atom with respect to a laser beam will see the light frequency up-shifted, while a co-propagating one will see the light frequency down-shifted. Due to this effect, a laser light beam with negative detuning (also called red detuned) can interact with the atom only if they are counter-propagating. Since photons carry energy and momentum, the atom gets a momentum kick each time it absorbs a photon reducing its initial velocity. The subsequent spontaneous emission, on the other hand, is isotropic, in average not affecting the velocity of the

atom. This will produce a total net force in the opposite direction of the atom's propagation direction. It is a friction force, which is proportional to the velocity of the atom. The following explanations are based on a lecture by Helene Perrin in Les Houches summer school of 2012 [181] and [182].

The force applied to the atoms can be expressed by the radiation pressure for a plane wave of wavevector $\mathbf{k}_L$ as

$$\mathbf{F}_{rp} = \frac{\Gamma}{2}\frac{s_0}{1+s_0}\hbar\mathbf{k}_L, \tag{B.1}$$

where Γ is the natural linewidth of the transition, s_0 is the saturation parameter which can be expressed in terms of the Rabi frequency Ω, the natural linewidth and the effective detuning δ' as $s_0 = \frac{\Omega^2/2}{\delta'^2+\Gamma^2/4}$. $\mathbf{F}_{rp}$ is the mean force due to the momentum transfer of one recoil $\hbar\mathbf{k}_L$ each time a photon is absorbed by the atom.

For an atom with a velocity $\mathbf{v}$, the effective detuning includes the Doppler shift and becomes $\delta' = \delta - \mathbf{k}_L \cdot \mathbf{v}$, giving

$$\mathbf{F}_{rp}(\mathbf{v}) = \frac{\Gamma}{2}\frac{\Omega^2/2}{\Omega^2/2+\Gamma^2/4+(\delta-\mathbf{k}_L\cdot\mathbf{v})^2}\hbar\mathbf{k}_L. \tag{B.2}$$

For low velocities where $|2\delta\mathbf{k}_L \cdot \mathbf{v}| << \Omega^2/2+\Gamma^2/4+\delta^2$ (true for $|\mathbf{k}_L \cdot \mathbf{v}| << \Gamma^2/2$), the expression of Eq. (B.2) can be linearized and becomes

$$\mathbf{F}_{rp}(\mathbf{v}) \simeq \frac{\Gamma}{2}\frac{\Omega^2/2}{\Omega^2/2+\Gamma^2/4+\delta^2}\hbar\mathbf{k}_L + \frac{\Omega^2/2}{(\Omega^2/2+\Gamma^2/4+\delta)^2}\delta\Gamma\hbar(\mathbf{k}_L\cdot\mathbf{v})\mathbf{k}_L. \tag{B.3}$$

The first term is the force for zero velocity, and the second term is proportional to the atomic velocity component in the direction of the laser. Calling $\mathbf{e}_z$ the direction of the wavevector, $\mathbf{k}_L = k_L\mathbf{e}_z$, then $(\mathbf{k}_L \cdot \mathbf{v})\mathbf{k}_L = k_L^2 v_z \mathbf{e}_z$, with v_z the z component of $\mathbf{v}$, we obtain the final expression for

the radiation pressure

$$\mathbf{F}_{rp}(\mathbf{v}) \simeq \mathbf{F}_{rp}(\mathbf{v}=\mathbf{0}) - \frac{\alpha}{2} v_z \mathbf{e}_z, \tag{B.4}$$

where $\alpha = -2\frac{s_0}{(1+s_0)^2}\hbar k_L^2 \frac{\delta\Gamma}{\delta^2+\Gamma^2/4}$ is the friction coefficient. The friction force is opposite to the direction of the atomic velocity only for $\alpha > 0$, which means $\delta < 0$.

However, the main component of this force is for zero velocity, and would accelerate the atoms in the direction of the laser beam. This term can simply be canceled by adding a second counter-propagating beam with wavevector $\mathbf{k}'_L = -\mathbf{k}_L$. Adding the two contributions, the total force in the z direction becomes

$$\mathbf{F}_{rp}(\mathbf{v}) = -\alpha v_z \mathbf{e}_z. \tag{B.5}$$

This can be generalized to 3 dimensions by using a pair of counter-propagating beams in each directions of space.

Doppler cooling temperature limit

For a classical particle of mass m and initial velocity $\mathbf{v}_0$, the temporal evolution of the velocity is calculated with Newton's second law of motion $m\frac{d\mathbf{v}}{dt} = -\alpha\mathbf{v}$, giving

$$\mathbf{V}(t) = \mathbf{v}_0 e^{-\alpha t/m}. \tag{B.6}$$

This would allow the velocity and temperature to reach a null value, which does not happen in real experiments. In fact, a heating process due to random recoil is competing with the Doppler cooling, due to the natural linewidth of the transition. The Doppler temperature T_D, which is the lowest temperature achievable through the use of the Doppler effect, is

$$k_B T_D = \frac{\hbar\Gamma}{2}. \tag{B.7}$$

For rubidium, this temperature is equal to 140 μK, and can be achieved in a few milliseconds only due to the important scattering rate of the relevant atomic transition.

Cooling of the atoms only is not sufficient in order to keep them around the same position for an extended period of time, since they are lost as soon as they leave the laser beams intersection. This requires the addition of a position dependent potential, which can conveniently be produced by adding a magnetic field gradient on the atoms.

B.2 Quadrupolar magnetic potential

The magnetic field gradient is produced by a pair of magnetic coils. An equal in amplitude but opposite in sign current flows in each coil. This produces a gradient of magnetic field, passing from a positive maximum at the position of one of the coils, to zero between the two coils, to a negative maximum at the position of the second coil. This gradient can be linear if the coils are setup in the anti-Helmholtz configuration. This means that, in addition to having opposite sign currents, they must share a common axis, and the distance separating them must be equal to their radius.

Magnetic interaction

The interaction of an atom with a non zero total spin ($\mathbf{J} = \mathbf{L} + \mathbf{S}$) and a magnetic field is

$$\hat{V}_m = -\hat{\mathbf{J}} \cdot \mathbf{B}(\mathbf{r}). \tag{B.8}$$

The Zeeman sub-levels denoted as $|F, m_F\rangle$ are shifted by an amount $m_J g_J \mu_B B$, with m_J the z-component of the total angular momentum, g_J the Landé g-factor, and μ_B the Bohr magneton. In order to simply explain the effect of this interaction in the context of the magneto-optical trapping, let us consider a transition between a ground state where $J = 0$ and an excited state where $J' = 1$. The excited states $|J', m'\rangle$ will be shifted by $m'_J g_J \mu_B B$.

Consequently, the transitions frequencies between $|J=0,m=0\rangle$ and $|J'=1,m'\rangle$ will be $\omega_0 + \frac{m'_J g_J \mu_B B}{\hbar} = \omega_0 + \frac{m'_J g_J \mu_B b' x}{\hbar}$ for a one-dimensional linear gradient $B(\mathbf{r}) = b'x$. In this case, the radiation pressure force will depend on the position and internal atomic state, since the effective detuning of Eq. (B.2) becomes

$$\delta' = \delta - \frac{m' g_J \mu_B b' x}{\hbar} = \delta - m' \gamma_m b' x, \tag{B.9}$$

where $\gamma_m = g_J \mu_B / \hbar$ is called the gyromagnetic ratio. For this protocol to work properly, the polarization of the laser beams must also be chosen properly. Let us consider an atom along the x axis, and two counter-propagating beams with opposite polarizations σ^+ along $+\mathbf{e}_x$ and σ^- along $-\mathbf{e}_x$ (in the reference frame of the atoms). The $\sigma^\pm$ polarized light induces a transition between $|J=0,m=0\rangle$ and $|J'=1,m'=\pm 1\rangle$ with $\Delta_m = \pm 1$, and the effective detunings are $\delta' = \delta \mp \gamma_m b' x$. If we consider an atom with zero velocity, the expression of the radiation pressure force created by $\sigma^\pm$ light propagating along $\pm x$ is

$$\mathbf{F}_\pm(x) = \pm \frac{\Gamma}{2} \frac{\Omega^2/2}{\Omega^2/2 + \Gamma^2/4 + (\delta \mp \gamma_m b' x)^2} \hbar \mathbf{k}_L. \tag{B.10}$$

Adding the two forces in the low saturation regime ($s_0 << 1$) and around the center ($|x| << |\delta|/(\gamma_m b'), \Gamma/(\gamma_m b')$), we obtain

$$\mathbf{F} = -\kappa x \mathbf{e}_x, \tag{B.11}$$

with $\kappa = \frac{\gamma_m b'}{k_L}\alpha = -2\frac{s_0}{(1+s_0)^2}\frac{\delta\Gamma}{\delta^2+\Gamma^2/4}\hbar k_L \gamma_m b'$ the restoring coefficient. For negative detunings, this is a restoring force which is proportional to the position of the atoms. This can be generalized in 3 dimensions, noting that the expression of the quadrupolar magnetic field is $\mathbf{B}(\mathbf{r}) = b'(x\mathbf{e}_x + y\mathbf{e}_y - 2z\mathbf{e}_z)$, with z being the central axis of the coils:

$$\mathbf{F} = -\kappa x \mathbf{e}_x - \kappa y \mathbf{e}_y - 2\kappa z \mathbf{e}_z. \tag{B.12}$$

Finally, we can see that for atoms close to the center of the trap and low velocities, the total force given by the Doppler cooling and the magnetic interaction can be approximated as a damped oscillator in the form

$$\mathbf{F} \simeq -\alpha \mathbf{v} - \kappa \mathbf{r}. \tag{B.13}$$

MOT size

The size of an atomic cloud is determined by re-absorption of scattered photons by other atoms before these photons leave the cloud. This phenomenon, called radiation trapping, creates an interatomic repulsive force, and ultimately limits the achievable atomic density. In this case, adding more atoms will then increase the size of the cloud instead of the density. The photon scattering rate from a single atom in the low saturation limit is

$$\Gamma_{sc} = 3\Gamma s_0. \tag{B.14}$$

A second atom placed at a distance r with an absorption cross section $\sigma = \sigma_{res}\frac{\Gamma^2}{4\delta^2+\Gamma^2}$ where $\sigma_{res} = 3\lambda^2/(2\pi)$ is the resonant cross section, will absorb a fraction $\sigma/(4\pi r^2)$ of these scattered photons. In case of reabsorption, a momentum change of $\hbar k_L$ in the direction of the second atom occurs. This leads to the following force, which is equivalent to a Coulomb force:

$$\mathbf{F}_{reabs} = 3\Gamma s_0 \frac{\sigma}{4\pi r^2}\hbar k_L \mathbf{u}_r. \tag{B.15}$$

This expression allows to find an expression for the atomic density in this regime, considering the analogy with a positively charged plasma in an harmonic trap:

$$n_0 = \frac{4}{3\pi}\frac{|\delta|}{\Gamma}\frac{\gamma_m b'}{\Gamma}k_L^2. \tag{B.16}$$

For rubidium atoms, with a detuning $\delta = \Gamma/2$ and a magnetic field gradient $b' = 10\,\mathrm{G}\cdot\mathrm{cm}^{-1}$, the calculated value is $n_0 = 3\times 10^9\,\mathrm{cm}^{-3}$. Considering an isotropic magnetic field gradient, the radius of such a cloud of N atoms

can be approximated as

$$R = \left(\frac{3}{4\pi}\frac{N}{n_0}\right)^{1/3}. \tag{B.17}$$

According to this formula, a standard MOT with a typical number of trapped atoms of 2.5×10^8, the radius of the cloud would be 2.7 mm, which is an estimation consistent with our measurements.

B.3 Sub-Doppler cooling

Experimental observations showed that temperatures below the theoretical Doppler limit are commonly achieved in many atom trapping experiments. This can be explained by considering the optical pumping dynamics of atoms with multiple sub-levels of the ground states (like Zeeman levels) by light fields with spatial polarization gradients [183–185]. This cooling process is known as sub-Doppler cooling, or Sisyphus cooling.

Standing wave

Let us first consider two counter-propagating laser beams along the z direction, of frequency $\omega_l = 2\pi c/\lambda$, and with identical polarization. The resulting field has the same polarization as the one of the incoming beams. The two plane-waves interfere and create a standing wave whose electric field, for a linear polarization of unit vector $\boldsymbol{\epsilon}$ can be written as

$$\begin{aligned}\mathbf{E}(z,t) &= E_0\boldsymbol{\epsilon}\cos(\omega_l t - kz) + E_0\boldsymbol{\epsilon}\cos(\omega_l t + kz)\\ &= 2E_0\boldsymbol{\epsilon}\cos(kz)\cos(\omega_l t),\end{aligned} \tag{B.18}$$

where $k = 2\pi/\lambda$ is the modulus of the wave-vector.

Polarization gradient

A light field with a polarization gradient can be obtained as the result of

two counter-propagating beams. There are two different cases to consider here. In the first case, called "lin $\perp$ lin", the two counter-propagating beams have orthogonal linear polarization, let us say along $\mathbf{x}$ and $\mathbf{y}$. The resulting field can be written as

$$\begin{aligned}\mathbf{E}(z,t) &= E_0\left[\mathbf{x}\cos(\omega_l t - kz) + \mathbf{y}\cos(\omega_l t + kz)\right] \\ &= E_0\left[(\mathbf{x}+\mathbf{y})\cos(\omega_l t)\cos(kz) + (\mathbf{x}-\mathbf{y})\sin(\omega_l t)\sin(kz)\right]. \quad \text{(B.19)}\end{aligned}$$

Its polarization will vary periodically over half of the wavelength, alternating between linear and circular with sign changes. At $z = 0$, we have

$$\mathbf{E}(z=0,t) = E_0(\mathbf{x}+\mathbf{y})\cos(\omega_l t), \quad \text{(B.20)}$$

corresponding to linear polarization at a $+\pi/4$ angle. Similarly, at $z = \lambda/4$ the field has a linear polarization at a $-\pi/4$ angle. For $z = \lambda/8$, the total field is

$$\mathbf{E}(z=\lambda/8,t) = E_0\left[\mathbf{x}\sin(\omega_l t + \pi/4) + \mathbf{y}\cos(\omega_l t + \pi/4)\right]. \quad \text{(B.21)}$$

Here, the $\mathbf{x}$ and $\mathbf{y}$ components are out of phase by $\pi/2$, corresponding to σ^- polarization, while when $z = 3\lambda/8$, the polarization is σ^+.

The second case, called "σ^+-σ^-" is when one beam is σ^+-polarized, and the other one is σ^--polarized. The resulting field is

$$\begin{aligned}\mathbf{E}(z,t) = E_0&\left[\mathbf{x}\cos(\omega_l t - kz) + \mathbf{y}\sin(\omega_l t - kz)\right] \\ &+ E_0\left[\mathbf{x}\cos(\omega_l t + kz) - \mathbf{y}\sin(\omega_l t + kz)\right] \\ &= 2E_0\cos(\omega_l t)\left[\mathbf{x}\cos(kz) + \mathbf{y}\sin(kz)\right]. \quad \text{(B.22)}\end{aligned}$$

This corresponds to a linear polarization uniformly rotating by 180° over half of the wavelength. In the following, I will explain the lin $\perp$ lin case.

Lin ⊥ lin: optical pumping

Let us consider a transition between a ground state with electron angular momentum $J_g = 1/2$ and an excited state with electron angular momentum $J_e = 3/2$, and a nuclear spin $I = 1$. In this case, the ground state has two magnetic sub-levels $M_g = \pm 1/2$. In the places where the light field is purely σ^+, the optical pumping drives the atomic population in $M_g = +1/2$, and in $M_g = -1/2$ where the polarization is σ^-. This means that traveling atoms will change ground states over a length of a quarter of the wavelength.

Lin ⊥ lin: light shifts

The interaction of a nearly resonant light field with atoms also gives rise to shifts of the energy levels, called light shifts. They are principally due to the AC-Stark effect from the electric field of the light. In the low intensity limit of two laser beams, the light shifts of the ground magnetic sub-levels are given by

$$\Delta E_g = \frac{\hbar \delta s_0 C_{ge}^2}{1 + (2\delta/\gamma)^2}, \tag{B.23}$$

with δ the light detuning, s_0 the saturation parameter, C_{ge} the Clebsch-Gordan coefficient for the transition, and γ the natural linewidth. In this case, $C^2_{-\frac{1}{2},+\frac{1}{2}} = 50$ and $C^2_{+\frac{1}{2},+\frac{3}{2}} = 150$ for σ^+ light, and resp. 150 and 50 for σ^- light. This means that the light shift for the sub-level $M_g = +1/2$ is three times larger than for $M_g = -1/2$ when light is σ^+-polarized. This is illustrated in Fig. B.1. An atom starting in $M_g = +1/2$ at a place where the polarization is purely σ^+ moves towards the right. The light shifts of the energy levels are changing on a length scale of $\lambda/2$ due to the polarization gradient. Moving towards $\lambda/4$, some part of the kinetic energy is converted to potential energy. When the atom reaches $\lambda/4$, it can absorb a photon (black vertical arrows) and be optically pumped to $M_g = -1/2$ because there the polarization is σ^-. The potential energy is radiated away by the emitted photon, since the emission is at higher frequency than the absorption. This process can occur as long as the energy of the atom is sufficient to reach the top of an energy potential

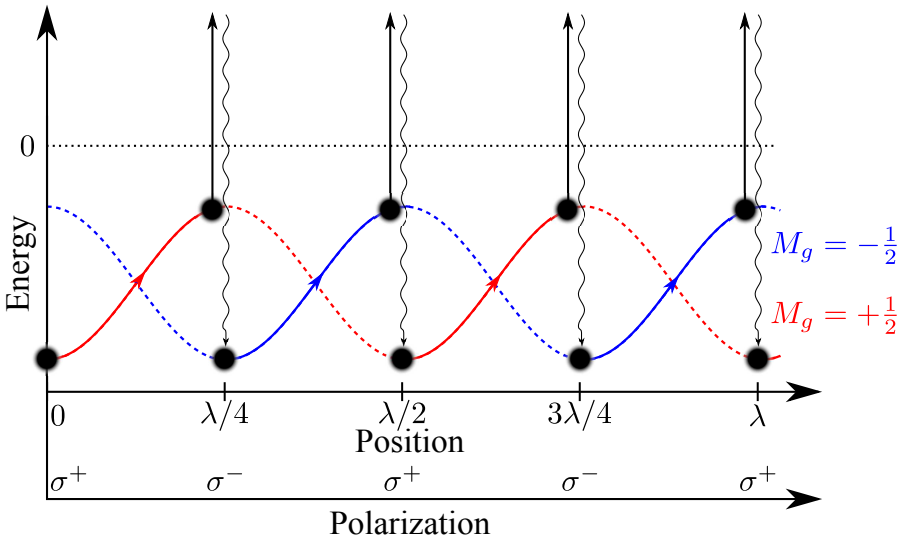

FIGURE B.1: **Polarization-dependent light shifts and optical pumping of ground sub-levels.**

hill. It is also more efficient for atoms whose velocity allows them to travel over $\lambda/4$ in the timescale of the optical pumping process. Slower or faster atoms will not be at a potential maximum when they absorb a photon, hence dissipating less energy.

Appendix C

Frequency modulation

The electric field of the laser is $E(t) = E_0 e^{-i\omega_0 t}$, with E_0 the amplitude and ω_0 the central frequency. A temporal phase modulation

$$\phi(t) = \beta \cdot \sin(\Omega t + \phi_m) \tag{C.1}$$

is applied to the electric field via frequency modulation of the AOM through which the laser is passing, with Ω the modulation of frequency, β the modulation index and a phase ϕ_m. The electric field becomes $E(t) = E_0 e^{-i\omega_0 t - i\phi(t)}$. The instantaneous optical frequency ω_{inst} is given by the instantaneous rate of change of the optical phase, such that

$$\omega_{inst} = \omega_0 + \frac{d\phi}{dt} = \omega_0 + \Delta\omega \cdot \cos(\Omega t + \phi_m), \tag{C.2}$$

with $\Delta\omega = \beta \cdot \Omega$ the maximum frequency excursion. For a high modulation index ($\beta = \Delta\omega/\Omega >> 1$), but with the maximum frequency excursion still low compared to the central frequency (which is the case for us), the voltage given by a photodiode for light modulated around ω_0 is given by

$$V(t) = V(\omega_0 + \Delta\omega \cdot \cos(\Omega t + \phi_m)), \tag{C.3}$$

which can be expanded as

$$V(t) = V(\omega_0) + \left.\frac{dV}{d\omega}\right|_{\omega_0} \Delta\omega \cdot \cos(\Omega t + \phi_m). \tag{C.4}$$

This signal is then demodulated by multiplying it with a reference signal at the same frequency as the one used for the modulation, written as

$$D(t) = D_0 \cos(\Omega t + \phi_d). \tag{C.5}$$

This is done by a module called lock-in amplifier. The result is an error signal

$$\begin{aligned} &Err(t) = V(t) \cdot D(t) = \\ &V(\omega_0) \cdot D_0 \cdot \cos(\Omega t + \phi_d) + D_0 \cdot \Delta\omega \cdot \left.\frac{dV}{d\omega}\right|_{\omega_0} (\cos(\Omega t + \phi_m) \cdot \cos(\Omega t + \phi_d)) = \\ &V(\omega_0) \cdot D_0 \cdot \cos(\Omega t + \phi_d) + D_0 \cdot \Delta\omega \cdot \left.\frac{dV}{d\omega}\right|_{\omega_0} \frac{1}{2} (\cos(2\Omega t + \phi_m + \phi_d) + \cos(\phi_m - \phi_d)) . \end{aligned} \tag{C.6}$$

A low-pass filter then removes the components of $Err(t)$ at frequencies Ω and 2Ω, leaving

$$Err = D_0 \cdot \Delta\omega \cdot \left.\frac{dV}{d\omega}\right|_{\omega_0} \frac{1}{2} \cos(\phi_m - \phi_d). \tag{C.7}$$

This expression is then proportional to the first order derivative of the spectroscopy signal and can be maximized by appropriately matching the modulation and demodulation phases.

Appendix D

Magnetic field gradient approximation

We use a negative hyperbolic tangent as the temporal profile of our magnetic field gradient in order to calculate the temporal behavior of the spin-wave's phase. The profile measured with a Hall probe placed on the coils axis is shown in Fig. D.1. The blue solid line is the normalized amplitude, which is proportional to the gradient. The dashed line is the normalized integral of the field's amplitude. The spin-wave is in phase when the integral is equal to zero, which is the case initially and at the rephasing time. There are two different slopes in the field's profile, corresponding to the "unloading" and "negative reloading" phases. During the unloading phase, the power supply of the coils is disconnected, and they are connected to the ground. For the negative reloading, the power supply is reconnected in such a way that the current flows in the opposite direction. Moreover, a capacitor loaded with high voltage is connected in parallel. This allows to have a resonant RLC circuit with a fast energy transfer from the capacitor to the coils. As a result, the current increases much faster than by passive loading using the power supply alone.

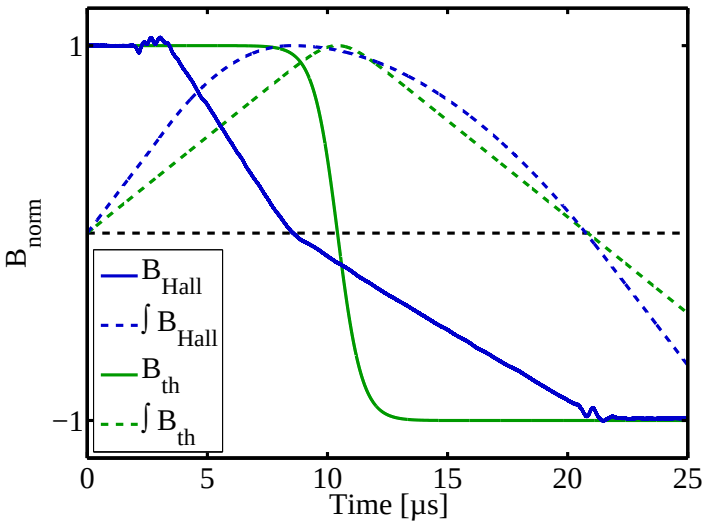

FIGURE D.1: **Magnetic field gradient reversal.** Blue solid line: normalized magnetic field gradient amplitude measured with a Hall probe. Green solid line: negative hyperbolic tangent used to approximate the magnetic field. Blue and green dashed lines: normalized integrals of the gradient amplitude and negative hyperbolic tangent.

The important point here is that the rephasing time does not depend on the temporal profile of the magnetic field itself, as long as the cancellation of the integral happens at the same time. In particular, it is not influenced by the switching speed if the rephasing occurs in a region of constant current. Moreover, the width of the rephasing peak depends on the amplitude of the gradient around the rephasing time. As a consequence, we can faithfully approximate the measured temporal profile by a negative hyperbolic tangent (green solid line). The corresponding integral is shown by the green dashed line. This approximation allows to simplify the calculations leading to eq. (6.14).

Bibliography

[1] P. Zoller, T. Beth, D. Binosi, R. Blatt, et al.: *Quantum information processing and communication*, Eur. Phys. J. D **36**, 203 (2005).

[2] T. D. Ladd, F. Jelezko, R. Laflamme, Y. Nakamura, et al.: *Quantum computers.*, Nature **464**, 45 (2010).

[3] N. Gisin, G. Ribordy, W. Tittel, and H. Zbinden: *Quantum cryptography*, Rev. Mod. Phys. **74**, 145 (2002).

[4] C. Monroe, D. M. Meekhof, B. E. King, W. M. Itano, et al.: *Demonstration of a Fundamental Quantum Logic Gate*, Phys. Rev. Lett. **75**, 4714 (1995).

[5] K. Boone, J.-P. Bourgoin, E. Meyer-Scott, K. Heshami, et al.: *Entanglement over global distances via quantum repeaters with satellite links*, Phys. Rev. A **91**, 052325 (2015).

[6] B. Korzh, C. C. W. Lim, R. Houlmann, N. Gisin, et al.: *Provably secure and practical quantum key distribution over 307 km of optical fibre*, Nat. Photonics **9**, 163 (2015).

[7] W. K. Wootters and W. H. Zurek: *A single quantum cannot be cloned*, Nature **299**, 802 (1982).

[8] H.-J. Briegel, W. Dür, J. I. Cirac, and P. Zoller: *Quantum Repeaters : The Role of Imperfect Local Operations in Quantum Communication*, Phys. Rev. Lett. **81**, 5932 (1998).

[9] J. F. Clauser, M. A. Horne, A. Shimony, and R. A. Holt: *Proposed Experiment to Test Local Hidden-Variable Theories*, Phys. Rev. Lett. **23**, 880 (1969).

[10] J. Calsamiglia and N. Lütkenhaus: *Maximum efficiency of a linear-optical Bell-state analyzer*, Appl. Phys. B **72**, 67 (2014).

[11] C. H. Bennett, C. Crepeau, R. Jozsa, and A. Peres: *Teleporting an Unknown Quantum State via Dual Classical and Einstein-Podolsky-Rosen Channels*, Phys. Rev. Lett. **70**, 1895 (1993).

[12] M. Żukowski, a. Zeilinger, M. Horne, and a. Ekert: *"Event-ready-detectors" Bell experiment via entanglement swapping*, Phys. Rev. Lett. **71**, 4287 (1993).

[13] A. I. Lvovsky, B. C. Sanders, and W. Tittel: *Optical quantum memory*, Nat. Photonics **3**, 706 (2009).

[14] K. Hammerer, A. S. Sø rensen, and E. S. Polzik: *Quantum interface between light and atomic ensembles*, Rev. Mod. Phys. **82**, 1041 (2010).

[15] L. M. Duan, M. D. Lukin, J. I. Cirac, and P. Zoller: *Long-distance quantum communication with atomic ensembles and linear optics.*, Nature **414**, 413 (2001).

[16] E. Bimbard, R. Boddeda, N. Vitrant, A. Grankin, et al.: *Homodyne Tomography of a Single Photon Retrieved on Demand from a Cavity-Enhanced Cold Atom Memory*, Phys. Rev. Lett. **112**, 033601 (2014).

[17] M. Afzelius, C. Simon, H. de Riedmatten, and N. Gisin: *Multimode quantum memory based on atomic frequency combs*, Phys. Rev. A **79**, 052329 (2009).

[18] Q. Glorieux, J. B. Clark, A. M. Marino, Z. Zhou, et al.: *Temporally multiplexed storage of images in a gradient echo memory.*, Opt. Express **20**, 12350 (2012).

[19] B. Albrecht, P. Farrera, G. Heinze, M. Cristiani, et al.: *Controlled rephasing of single collective spin excitations in a cold atomic quantum memory*, Arxiv Prepr. **1501.07559** (2015).

[20] S.-Y. Lan, A. G. Radnaev, O. A. Collins, D. N. Matsukevich, et al.: *A Multiplexed Quantum Memory*, Opt. Express **17**, 13639 (2009).

[21] J. Nunn, I. A. Walmsley, M. G. Raymer, K. Surmacz, et al.: *Mapping broadband single-photon wave packets into an atomic memory*, Phys. Rev. A **75**, 011401 (2007).

[22] D. V. Vasilyev, I. V. Sokolov, and E. S. Polzik: *Quantum memory for images: A quantum hologram*, Phys. Rev. A **77**, 020302 (2008).

[23] B. Lauritzen, J. Minář, H. de Riedmatten, M. Afzelius, et al.: *Telecommunication-Wavelength Solid-State Memory at the Single Photon Level*, Phys. Rev. Lett. **104**, 080502 (2010).

[24] E. Saglamyurek, J. Jin, V. B. Verma, M. D. Shaw, et al.: *Quantum storage of entangled telecom-wavelength photons in an erbium-doped optical fibre*, Nat. Photonics **9**, 83 (2015).

[25] A. G. Radnaev, Y. O. Dudin, R. Zhao, H. H. Jen, et al.: *A quantum memory with telecom-wavelength conversion*, Nat. Phys. **6**, 894 (2010).

[26] B. Albrecht, P. Farrera, X. Fernandez-Gonzalvo, M. Cristiani, et al.: *A waveguide frequency converter connecting rubidium-based quantum memories to the telecom C-band*, Nat. Commun. **5**, 3376 (2014).

[27] H. J. Kimble: *The quantum internet.*, Nature **453**, 1023 (2008).

[28] R. J. Thompson, G. Rempe, and H. J. Kimble: *Observation of normal-mode splitting for an atom in an optical cavity*, Phys. Rev. Lett. **68**, 1132 (1992).

[29] A. D. Boozer, A. Boca, R. Miller, T. E. Northup, et al.: *Reversible State Transfer between Light and a Single Trapped Atom*, Phys. Rev. Lett. **98**, 193601 (2007).

[30] T. Wilk, S. C. Webster, A. Kuhn, and G. Rempe: *Single-atom single-photon quantum interface.*, Science **317**, 488 (2007).

[31] H. P. Specht, C. Nölleke, A. Reiserer, M. Uphoff, et al.: *A single-atom quantum memory.*, Nature **473**, 190 (2011).

[32] S. Ritter, C. Nölleke, C. Hahn, A. Reiserer, et al.: *An elementary quantum network of single atoms in optical cavities.*, Nature **484**, 195 (2012).

[33] J. Hofmann, M. Krug, N. Ortegel, L. Gérard, et al.: *Heralded entanglement between widely separated atoms.*, Science **337**, 72 (2012).

[34] N. Kalb, A. Reiserer, S. Ritter, and G. Rempe: *Heralded Storage of a Photonic Quantum Bit in a Single Atom*, Phys. Rev. Lett. **114**, 220501 (2015).

[35] D. L. Moehring, P. Maunz, S. Olmschenk, K. C. Younge, et al.: *Entanglement of single-atom quantum bits at a distance.*, Nature **449**, 68 (2007).

[36] N. Piro, A. Haase, M. W. Mitchell, and J. Eschner: *An entangled photon source for resonant single-photon–single-atom interaction*, J. Phys. B At. Mol. Opt. Phys. **42**, 114002 (2009).

[37] P. C. Maurer, G. Kucsko, C. Latta, L. Jiang, et al.: *Room-temperature quantum bit memory exceeding one second.*, Science **336**, 1283 (2012).

[38] H. Bernien, L. Childress, L. Robledo, M. Markham, et al.: *Two-Photon Quantum Interference from Separate Nitrogen Vacancy Centers in Diamond*, Phys. Rev. Lett. **108**, 043604 (2012).

[39] A. Sipahigil, M. L. Goldman, E. Togan, Y. Chu, et al.: *Quantum Interference of Single Photons from Remote Nitrogen-Vacancy Centers in Diamond*, Phys. Rev. Lett. **108**, 143601 (2012).

[40] H. Bernien, B. Hensen, W. Pfaff, G. Koolstra, et al.: *Heralded entanglement between solid-state qubits separated by three metres.*, Nature **497**, 86 (2013).

[41] W. Pfaff, B. J. Hensen, H. Bernien, S. B. van Dam, et al.: *Quantum information. Unconditional quantum teleportation between distant solid-state quantum bits.*, Science **345**, 532 (2014).

[42] G. Heinze, C. Hubrich, and T. Halfmann: *Stopped Light and Image Storage by Electromagnetically Induced Transparency up to the Regime of One Minute*, Phys. Rev. Lett. **111**, 033601 (2013).

[43] W. Tittel, M. Afzelius, T. Chaneliére, R. Cone, et al.: *Photon-echo quantum memory in solid state systems*, Laser Photon. Rev. **4**, 244 (2009).

[44] M. D. Eisaman, a. André, F. Massou, M. Fleischhauer, et al.: *Electromagnetically induced transparency with tunable single-photon pulses.*, Nature **438**, 837 (2005).

[45] C. Kupchak, T. Mittiga, B. Jordaan, M. Namazi, et al.: *Room-temperature single-photon level memory for polarization states.*, Sci. Rep. **5**, 7658 (2015).

[46] M. D. Lukin: *Colloquium : Trapping and manipulating photon states in atomic ensembles*, Rev. Mod. Phys. **75**, 457 (2003).

[47] K.-J. Boller, A. Imamoğlu, and S. E. Harris: *Observation of electromagnetically induced transparency*, Phys. Rev. Lett. **66**, 2593 (1991).

[48] M. Fleischhauer, A. Imamoglu, and J. Marangos: *Electromagnetically induced transparency: Optics in coherent media*, Rev. Mod. Phys. **77**, 633 (2005).

[49] S. H. Autler and C. H. Townes: *Stark Effect in Rapidly Varying Fields*, Phys. Rev. **100**, 703 (1955).

[50] J. H. Eberly, M. L. Pons, and H. R. Haq: *Dressed-field pulses in an absorbing medium*, Phys. Rev. Lett. **72**, 56 (1994).

[51] T. Chanelière, D. N. Matsukevich, S. D. Jenkins, S.-Y. Lan, et al.: *Storage and retrieval of single photons transmitted between remote quantum memories.*, Nature **438**, 833 (2005).

[52] K. S. Choi, H. Deng, J. Laurat, and H. J. Kimble: *Mapping photonic entanglement into and out of a quantum memory*, Nature **452**, 67 (2008).

[53] M. Lettner, M. Mücke, S. Riedl, C. Vo, et al.: *Remote Entanglement between a Single Atom and a Bose-Einstein Condensate*, Phys. Rev. Lett. **106**, 210503 (2011).

[54] H. Zhang, X.-M. Jin, J. Yang, H.-N. Dai, et al.: *Preparation and storage of frequency-uncorrelated entangled photons from cavity-enhanced spontaneous parametric downconversion*, Nat. Photonics **5**, 628 (2011).

[55] S. Zhou, S. Zhang, C. Liu, J. F. Chen, et al.: *Optimal storage and retrieval of single-photon waveforms.*, Opt. Express **20**, 24124 (2012).

[56] Y.-H. Chen, M.-J. Lee, I.-C. Wang, S. Du, et al.: *Coherent Optical Memory with High Storage Efficiency and Large Fractional Delay*, Phys. Rev. Lett. **110**, 083601 (2013).

[57] Y. O. Dudin, L. Li, and A. Kuzmich: *Light storage on the time scale of a minute*, Phys. Rev. A **87**, 031801 (2013).

[58] L. Veissier, A. Nicolas, L. Giner, D. Maxein, et al.: *Reversible optical memory for twisted photons.*, Opt. Lett. **38**, 712 (2013).

[59] A. Nicolas, L. Veissier, L. Giner, E. Giacobino, et al.: *A quantum memory for orbital angular momentum photonic qubits*, Nat. Photonics **8**, 234 (2014).

[60] D.-S. Ding, W. Zhang, Z.-Y. Zhou, S. Shi, et al.: *Quantum Storage of Orbital Angular Momentum Entanglement in an Atomic Ensemble*, Phys. Rev. Lett. **114**, 050502 (2015).

[61] K. Honda, D. Akamatsu, M. Arikawa, Y. Yokoi, et al.: *Storage and Retrieval of a Squeezed Vacuum*, Phys. Rev. Lett. **100**, 093601 (2008).

[62] M. Arikawa, K. Honda, D. Akamatsu, S. Nagatsuka, et al.: *Quantum memory of a squeezed vacuum for arbitrary frequency sidebands*, Phys. Rev. A **81**, 021605 (2010).

[63] C. V. Raman and K. S. Krishnan: *A New Type of Secondary Radiation* (1928).

[64] K. F. Reim, J. Nunn, V. O. Lorenz, B. J. Sussman, et al.: *Towards high-speed optical quantum memories*, Nat. Photonics **4**, 218 (2010).

[65] K. F. Reim, P. Michelberger, K. C. Lee, J. Nunn, et al.: *Single-Photon-Level Quantum Memory at Room Temperature*, Phys. Rev. Lett. **107**, 053603 (2011).

[66] D. G. England, P. S. Michelberger, T. F. M. Champion, K. F. Reim, et al.: *High-fidelity polarization storage in a gigahertz bandwidth quantum memory*, J. Phys. B At. Mol. Opt. Phys. **45**, 124008 (2012).

[67] U. H. Kopvillem and V. R. Nagibarov: *Light echo on paramagnetic crystals*, Phys. Met. Phys. Metall. **15**, 313 (1963).

[68] N. A. Kurnit, I. D. Abella, and S. R. Hartmann: *Observation of a Photon Echo*, Phys. Rev. Lett. **13**, 567 (1964).

[69] S. Moiseev and S. Kröll: *Complete Reconstruction of the Quantum State of a Single-Photon Wave Packet Absorbed by a Doppler-Broadened Transition*, Phys. Rev. Lett. **87**, 173601 (2001).

[70] M. Nilsson and S. Kröll: *Solid state quantum memory using complete absorption and re-emission of photons by tailored and externally controlled inhomogeneous absorption profiles*, Opt. Commun. **247**, 393 (2005).

[71] B. Kraus, W. Tittel, N. Gisin, M. Nilsson, et al.: *Quantum memory for nonstationary light fields based on controlled reversible inhomogeneous broadening*, Phys. Rev. A **73**, 020302 (2006).

[72] A. L. Alexander, J. J. Longdell, M. J. Sellars, and N. B. Manson: *Photon Echoes Produced by Switching Electric Fields*, Phys. Rev. Lett. **96**, 043602 (2006).

[73] G. Hétet, J. J. Longdell, A. L. Alexander, P. K. Lam, et al.: *Electro-Optic Quantum Memory for Light Using Two-Level Atoms*, Phys. Rev. Lett. **100**, 023601 (2008).

[74] M. P. Hedges, J. J. Longdell, Y. Li, and M. J. Sellars: *Efficient quantum memory for light.*, Nature **465**, 1052 (2010).

[75] M. Hosseini, B. M. Sparkes, G. T. Campbell, P. K. Lam, et al.: *Storage and manipulation of light using a Raman gradient-echo process*, J. Phys. B At. Mol. Opt. Phys. **45**, 124004 (2012).

[76] M. Hosseini, B. M. Sparkes, G. Campbell, P. K. Lam, et al.: *High efficiency coherent optical memory with warm rubidium vapour.*, Nat. Commun. **2**, 174 (2011).

[77] M. Hosseini, G. Campbell, B. M. Sparkes, P. K. Lam, et al.: *Unconditional room-temperature quantum memory*, Nat. Phys. **7**, 794 (2011).

[78] M. Hosseini, B. M. Sparkes, G. Campbell, P. K. Lam, et al.: *High efficiency coherent optical memory with warm rubidium vapour.*, Nat. Commun. **2**, 174 (2011).

[79] O. Pinel, M. Hosseini, B. M. Sparkes, J. L. Everett, et al.: *Gradient echo quantum memory in warm atomic vapor.*, J. Vis. Exp. e50552 (2013).

[80] B. M. Sparkes, J. Bernu, M. Hosseini, J. Geng, et al.: *Gradient echo memory in an ultra-high optical depth cold atomic ensemble*, New J. Phys. **15**, 085027 (2013).

[81] H. de Riedmatten, M. Afzelius, M. U. Staudt, C. Simon, et al.: *A solid-state light-matter interface at the single-photon level*, Nature **456**, 773 (2008).

[82] M. Bonarota, J. Ruggiero, J. L. L. Gouët, and T. Chanelière: *Efficiency optimization for atomic frequency comb storage*, Phys. Rev. A **81**, 033803 (2010).

[83] M. Sabooni, F. Beaudoin, a. Walther, N. Lin, et al.: *Storage and Recall of Weak Coherent Optical Pulses with an Efficiency of 25%*, Phys. Rev. Lett. **105**, 060501 (2010).

[84] I. Usmani, M. Afzelius, H. de Riedmatten, and N. Gisin: *Mapping multiple photonic qubits into and out of one solid-state atomic ensemble.*, Nat. Commun. **1**, 12 (2010).

[85] M. Sabooni, S. Tornibue Kometa, a. Thuresson, S. Kröll, et al.: *Cavity-enhanced storage—preparing for high-efficiency quantum memories*, New J. Phys. **15**, 035025 (2013).

[86] F. Bussières, C. Clausen, A. Tiranov, B. Korzh, et al.: *Quantum teleportation from a telecom-wavelength photon to a solid-state quantum memory*, Nat. Photonics **8**, 775 (2014).

[87] P. Jobez, I. Usmani, N. Timoney, C. Laplane, et al.: *Cavity-enhanced storage in an optical spin-wave memory*, New J. Phys. **16**, 083005 (2014).

[88] N. Maring, K. Kutluer, J. Cohen, M. Cristiani, et al.: *Storage of up-converted telecom photons in a doped crystal*, New J. Phys. **16**, 113021 (2014).

[89] D. Rieländer, K. Kutluer, P. M. Ledingham, M. Gündoğan, et al.: *Quantum Storage of Heralded Single Photons in a Praseodymium-Doped Crystal*, Phys. Rev. Lett. **112**, 040504 (2014).

[90] C. Clausen, I. Usmani, F. Bussières, N. Sangouard, et al.: *Quantum storage of photonic entanglement in a crystal.*, Nature **469**, 508 (2011).

[91] E. Saglamyurek, N. Sinclair, J. Jin, J. A. Slater, et al.: *Broadband waveguide quantum memory for entangled photons*, Nature **469**, 512 (2011).

[92] I. Usmani, C. Clausen, P. Jobez, C. Laplane, et al.: *Heralded quantum entanglement between two crystals* (2012).

[93] C. Clausen, F. Bussières, M. Afzelius, and N. Gisin: *Quantum Storage of Heralded Polarization Qubits in Birefringent and Anisotropically Absorbing Materials*, Phys. Rev. Lett. **108**, 190503 (2012).

[94] M. Gündoğan, P. M. Ledingham, A. Almasi, M. Cristiani, et al.: *Quantum Storage of a Photonic Polarization Qubit in a Solid*, Phys. Rev. Lett. **108**, 190504 (2012).

[95] Z.-Q. Zhou, W.-B. Lin, M. Yang, C.-F. Li, et al.: *Realization of Reliable Solid-State Quantum Memory for Photonic Polarization Qubit*, Phys. Rev. Lett. **108**, 190505 (2012).

[96] M. Gündoğan, M. Mazzera, P. M. Ledingham, M. Cristiani, et al.: *Coherent storage of temporally multimode light using a spin-wave atomic frequency comb memory*, New J. Phys. **15**, 045012 (2013).

[97] N. Sinclair, E. Saglamyurek, H. Mallahzadeh, J. a. Slater, et al.: *Spectral Multiplexing for Scalable Quantum Photonics using an*

Atomic Frequency Comb Quantum Memory and Feed-Forward Control, Phys. Rev. Lett. **113**, 053603 (2014).

[98] M. Afzelius, I. Usmani, A. Amari, B. Lauritzen, et al.: *Demonstration of Atomic Frequency Comb Memory for Light with Spin-Wave Storage*, Phys. Rev. Lett. **104**, 040503 (2010).

[99] N. Timoney, B. Lauritzen, I. Usmani, M. Afzelius, et al.: *Atomic frequency comb memory with spin-wave storage in 153 Eu 3 + :Y 2 SiO 5*, J. Phys. B At. Mol. Opt. Phys. **45**, 124001 (2012).

[100] N. Timoney, I. Usmani, P. Jobez, M. Afzelius, et al.: *Single-photon-level optical storage in a solid-state spin-wave memory*, Phys. Rev. A **88**, 022324 (2013).

[101] M. Gündoğan, P. M. Ledingham, K. Kutluer, M. Mazzera, et al.: *Solid State Spin-Wave Quantum Memory for Time-Bin Qubits*, Phys. Rev. Lett. **114**, 230501 (2015).

[102] P. Jobez, C. Laplane, N. Timoney, N. Gisin, et al.: *Coherent spin control at the quantum level in an ensemble-based optical memory* 5 (2015).

[103] B. Julsgaard, J. Sherson, J. I. Cirac, J. Fiurášek, et al.: *Experimental demonstration of quantum memory for light.*, Nature **432**, 482 (2004).

[104] J. F. Sherson, H. Krauter, R. K. Olsson, B. Julsgaard, et al.: *Quantum teleportation between light and matter.*, Nature **443**, 557 (2006).

[105] K. Jensen, W. Wasilewski, H. Krauter, T. Fernholz, et al.: *Quantum memory for entangled continuous-variable states*, Nat. Phys. **7**, 13 (2010).

[106] H. Krauter, D. Salart, C. A. Muschik, J. M. Petersen, et al.: *Deterministic quantum teleportation between distant atomic objects*, Nat. Phys. **9**, 400 (2013).

[107] L. M. Duan, J. I. Cirac, and P. Zoller: *Three-dimensional theory for interaction between atomic ensembles and free-space light* 16 (2002).

[108] A. Kuzmich, W. P. Bowen, A. D. Boozer, A. Boca, et al.: *Generation of nonclassical photon pairs for scalable quantum communication with atomic ensembles*, Nature **423**, 731 (2003).

[109] C. H. van der Wal, M. D. Eisaman, A. André, R. L. Walsworth, et al.: *Atomic Memory for Correlated Photon States*, Science (80-.). **301**, 196 (2003).

[110] C.-W. Chou, J. Laurat, H. Deng, K. S. Choi, et al.: *Functional quantum nodes for entanglement distribution over scalable quantum networks*, Science **316**, 1316 (2007).

[111] Z.-S. Yuan, Y.-A. Chen, B. Zhao, S. Chen, et al.: *Experimental demonstration of a BDCZ quantum repeater node.*, Nature **454**, 1098 (2008).

[112] C. W. Chou, H. de Riedmatten, D. Felinto, S. V. Polyakov, et al.: *Measurement-induced entanglement for excitation stored in remote atomic ensembles.*, Nature **438**, 828 (2005).

[113] K. S. Choi, A. Goban, S. B. Papp, S. J. van Enk, et al.: *Entanglement of spin waves among four quantum memories.*, Nature **468**, 412 (2010).

[114] D. Felinto, C. W. Chou, J. Laurat, E. W. Schomburg, et al.: *Conditional control of the quantum states of remote atomic memories for quantum networking*, Nat. Phys. **2**, 844 (2006).

[115] Z. S. Yuan, Y. A. Chen, S. Chen, B. Zhao, et al.: *Synchronized independent narrow-band single photons and efficient generation of photonic entanglement*, Phys. Rev. Lett. **98**, 2 (2007).

[116] J. Laurat, H. de Riedmatten, D. Felinto, C.-W. Chou, et al.: *Efficient retrieval of a single excitation stored in an atomic ensemble*, Opt. Express **14**, 6912 (2006).

[117] J. Simon, H. Tanji, J. K. Thompson, and V. Vuletić: *Interfacing Collective Atomic Excitations and Single Photons*, Phys. Rev. Lett. **98**, 183601 (2007).

[118] R. Zhao, Y. O. Dudin, S. D. Jenkins, C. J. Campbell, et al.: *Long-lived quantum memory*, Nat. Phys. **5**, 100 (2008).

[119] B. Zhao, Y.-A. Chen, X.-H. Bao, T. Strassel, et al.: *A millisecond quantum memory for scalable quantum networks*, Nat. Phys. **5**, 95 (2008).

[120] X.-H. Bao, A. Reingruber, P. Dietrich, J. Rui, et al.: *Efficient and long-lived quantum memory with cold atoms inside a ring cavity*, Nat. Phys. **8**, 517 (2012).

[121] X. Fernandez-Gonzalvo, G. Corrielli, B. Albrecht, M. L. Grimau, et al.: *Quantum frequency conversion of quantum memory compatible photons to telecommunication wavelengths.*, Opt. Express **21**, 19473 (2013).

[122] C. Simon, H. de Riedmatten, M. Afzelius, N. Sangouard, et al.: *Quantum Repeaters with Photon Pair Sources and Multimode Memories*, Phys. Rev. Lett. **98**, 190503 (2007).

[123] N. Sangouard, C. Simon, B. Zhao, Y.-A. Chen, et al.: *Robust and efficient quantum repeaters with atomic ensembles and linear optics*, Phys. Rev. A **77**, 062301 (2008).

[124] N. Sangouard, C. Simon, H. de Riedmatten, and N. Gisin: *Quantum repeaters based on atomic ensembles and linear optics*, Rev. Mod. Phys. **83**, 33 (2011).

[125] J. Laurat, K. S. Choi, H. Deng, C. W. Chou, et al.: *Heralded Entanglement between Atomic Ensembles: Preparation, Decoherence, and Scaling*, Phys. Rev. Lett. **99**, 180504 (2007).

[126] N. Sangouard, R. Dubessy, and C. Simon: *Quantum repeaters based on single trapped ions*, Phys. Rev. A **79**, 042340 (2009).

[127] J. Borregaard, P. Kómár, E. M. Kessler, M. D. Lukin, et al.: *Long-distance entanglement distribution using individual atoms in optical cavities*, Phys. Rev. A **92**, 012307 (2015).

[128] Y. Han, B. He, K. Heshami, C.-Z. Li, et al.: *Quantum repeaters based on Rydberg-blockade-coupled atomic ensembles*, Phys. Rev. A **81**, 052311 (2010).

[129] B. Zhao, M. Müller, K. Hammerer, and P. Zoller: *Efficient quantum repeater based on deterministic Rydberg gates*, Phys. Rev. A **81**, 052329 (2010).

[130] W. J. Munro, a. M. Stephens, S. J. Devitt, K. a. Harrison, et al.: *Quantum communication without the necessity of quantum memories*, Nat. Photonics **6**, 777 (2012).

[131] S. Muralidharan, J. Kim, N. Lütkenhaus, M. D. Lukin, et al.: *Ultrafast and Fault-Tolerant Quantum Communication across Long Distances*, Phys. Rev. Lett. **112**, 250501 (2014).

[132] K. Azuma, K. Tamaki, and H.-K. Lo: *All-photonic quantum repeaters.*, Nat. Commun. **6**, 6787 (2015).

[133] P. Kumar: *Quantum frequency conversion.*, Opt. Lett. **15**, 1476 (1990).

[134] J. Huang and P. Kumar: *Observation of quantum frequency conversion*, Phys. Rev. Lett. **68**, 2153 (1992).

[135] N. Curtz, R. Thew, C. Simon, N. Gisin, et al.: *Coherent frequency-down-conversion interface for quantum repeaters.*, Opt. Express **18**, 22099 (2010).

[136] Y. Ding and Z. Y. Ou: *Frequency downconversion for a quantum network.*, Opt. Lett. **35**, 2591 (2010).

[137] J. S. Pelc, C. Langrock, Q. Zhang, and M. M. Fejer: *Influence of domain disorder on parametric noise in quasi-phase-matched quantum frequency converters.*, Opt. Lett. **35**, 2804 (2010).

[138] H. Takesue: *Single-photon frequency down-conversion experiment*, Phys. Rev. A **82**, 013833 (2010).

[139] S. Zaske, A. Lenhard, and C. Becher: *Efficient frequency downconversion at the single photon level from the red spectral range to the telecommunications C-band.*, Opt. Express **19**, 12825 (2011).

[140] S. Tanzilli, W. Tittel, M. Halder, O. Alibart, et al.: *A photonic quantum information interface.*, Nature **437**, 116 (2005).

[141] R. Ikuta, Y. Kusaka, T. Kitano, H. Kato, et al.: *Wide-band quantum interface for visible-to-telecommunication wavelength conversion.*, Nat. Commun. **2**, 1544 (2011).

[142] S. Ramelow, A. Fedrizzi, A. Poppe, N. K. Langford, et al.: *Polarization-entanglement-conserving frequency conversion of photons*, Phys. Rev. A **85**, 013845 (2012).

[143] M. T. Rakher, L. Ma, O. Slattery, X. Tang, et al.: *Quantum transduction of telecommunications-band single photons from a quantum dot by frequency upconversion*, Nat. Photonics **4**, 786 (2010).

[144] M. T. Rakher, L. Ma, M. Davanço, O. Slattery, et al.: *Simultaneous Wavelength Translation and Amplitude Modulation of Single Photons from a Quantum Dot*, Phys. Rev. Lett. **107**, 083602 (2011).

[145] A. P. VanDevender and P. G. Kwiat: *Quantum transduction via frequency upconversion (Invited)*, J. Opt. Soc. Am. B **24**, 295 (2007).

[146] L. Ma, M. T. Rakher, M. J. Stevens, O. Slattery, et al.: *Temporal correlation of photons following frequency up-conversion.*, Opt. Express **19**, 10501 (2011).

[147] J. S. Pelc: *Frequency Conversion of Single Photons: Physics, Devices, and Applications*, Ph.D. thesis, Stanford University (2012).

[148] A. V. Gorshkov, A. André, M. D. Lukin, and A. S. S\orensen: *Photon storage in Lambda-type optically dense atomic media. II. Free-space model*, Phys. Rev. A **76**, 33805 (2007).

[149] J. Bohr Brask: *Long-distance distribution of discrete and continuous variable entanglement with atomic ensembles*, Phd, University of Copenhagen (2010).

[150] C. C. Gerry and P. L. Knight: *Introductory Quantum Optics* (2008).

[151] R. Loudon: *The Quantum Theory of Light* (2000).

[152] P. Grangier, G. Roger, and A. Aspect: *Experimental Evidence for a Photon Anticorrelation Effect on a Beam Splitter: A New Light on Single-Photon Interferences*, Europhys. Lett. **1**, 173 (1986).

[153] J. F. Clauser: *Experimental distinction between the quantum and classical field-theoretic predictions for the photoelectric effects*, Phys. Rev. D **9**, 853 (1974).

[154] H. de Riedmatten, J. Laurat, C. W. Chou, E. W. Schomburg, et al.: *Direct Measurement of Decoherence for Entanglement between a Photon and Stored Atomic Excitation*, Phys. Rev. Lett. **97**, 113603 (2006).

[155] S. Massar and S. Popescu: *Optimal Extraction of Information from Finite Quantum Ensembles*, Phys. Rev. Lett. **74**, 1259 (1995).

[156] A. J. Armstrong, N. Bloembergen, J. Ducuing, and P. S. Pershan: *Interactions between Light Waves in a Nonlinear Dielectric*, Phys. Rev. **127**, 1918 (1962).

[157] R. W. Boyd: *Nonlinear Optics*, Elsevier (2008).

[158] E. L. Raab, M. Prentiss, A. Cable, S. Chu, et al.: *Trapping ofNeutral Sodium Atoms with Radiation Pressure*, Phys. Rev. Lett. **59**, 2631 (1987).

[159] D. R. Lide: *CRC Handbook of Chemistry and Physics, 94th Edition, 2013-2014*, vol. 53 (2013).

[160] D. A. Steck: *Rubidium 87 D Line Data*, http://steck.us/alkalidata (2010).

[161] P. Palittapongarnpim, A. MacRae, and a. I. Lvovsky: *Note: A monolithic filter cavity for experiments in quantum optics*, Rev. Sci. Instrum. **83** (2012).

[162] S. Chen, Y.-A. Chen, T. Strassel, Z.-S. Yuan, et al.: *Deterministic and Storable Single-Photon Source Based on a Quantum Memory*, Phys. Rev. Lett. **97**, 173004 (2006).

[163] M. Fejer, G. Magel, D. Jundt, and R. Byer: *Quasi-phase-matched second harmonic generation: tuning and tolerances*, IEEE J. Quantum Electron. **28** (1992).

[164] K. De Greve, L. Yu, P. L. McMahon, J. S. Pelc, et al.: *Quantum-dot spin-photon entanglement via frequency downconversion to telecom wavelength.*, Nature **491**, 421 (2012).

[165] I. Marcikic, H. de Riedmatten, W. Tittel, H. Zbinden, et al.: *Long-distance teleportation of qubits at telecommunication wavelengths.*, Nature **421**, 509 (2003).

[166] C. Simon, H. de Riedmatten, and M. Afzelius: *Temporally multiplexed quantum repeaters with atomic gases*, Phys. Rev. A **82**, 010304 (2010).

[167] B. M. Sparkes, M. Hosseini, G. Hétet, P. K. Lam, et al.: *ac Stark gradient echo memory in cold atoms*, Phys. Rev. A **82**, 043847 (2010).

[168] C. Simon, M. Afzelius, J. Appel, A. Boyer de la Giroday, et al.: *Quantum memories*, Eur. Phys. J. D **58**, 1 (2010).

[169] Y. Dudin, S. Jenkins, R. Zhao, D. Matsukevich, et al.: *Entanglement of a Photon and an Optical Lattice Spin Wave*, Phys. Rev. Lett. **103**, 020505 (2009).

[170] A. Stute, B. Casabone, P. Schindler, T. Monz, et al.: *Tunable ion–photon entanglement in an optical cavity*, Nature **485**, 482 (2012).

[171] M. Stobińska, G. Alber, and G. Leuchs: *Perfect excitation of a matter qubit by a single photon in free space*, EPL (Europhysics Lett. **86**, 14007 (2009).

[172] S. Zhang, C. Liu, S. Zhou, C.-S. Chuu, et al.: *Coherent Control of Single-Photon Absorption and Reemission in a Two-Level Atomic Ensemble*, Phys. Rev. Lett. **109**, 263601 (2012).

[173] A. Goban, K. S. Choi, D. J. Alton, D. Ding, et al.: *Demonstration of a State-Insensitive, Compensated Nanofiber Trap*, Phys. Rev. Lett. **109**, 033603 (2012).

[174] J.-B. Béguin, E. Bookjans, S. Christensen, H. Sø rensen, et al.: *Generation and Detection of a Sub-Poissonian Atom Number Distribution in a One-Dimensional Optical Lattice*, Phys. Rev. Lett. **113**, 263603 (2014).

[175] B. Gouraud, D. Maxein, A. Nicolas, O. Morin, et al.: *Demonstration of a Memory for Tightly Guided Light in an Optical Nanofiber*, Phys. Rev. Lett. **114**, 180503 (2015).

[176] F. Le Kien and A. Rauschenbeutel: *Electromagnetically induced transparency for guided light in an atomic array outside an optical nanofiber*, Phys. Rev. A **91**, 053847 (2015).

[177] C. Sayrin, C. Clausen, B. Albrecht, P. Schneeweiss, et al.: *Storage of fiber-guided light in a nanofiber-trapped ensemble of cold atoms*, Optica **2**, 353 (2015).

[178] A. Grodecka-Grad, E. Zeuthen, and A. S. Sø rensen: *High-Capacity Spatial Multimode Quantum Memories Based on Atomic Ensembles*, Phys. Rev. Lett. **109**, 133601 (2012).

[179] J. Borregaard, M. Zugenmaier, J. M. Petersen, H. Shen, et al.: *Room temperature quantum memory and scalable single photon source based on motional averaging*, Arxiv Prepr. **1501.0391**, 1 (2015).

[180] T. W. Hänsch and A. L. Schwalow: *Cooling of Gases by Laser Radiation*, Opt. Commun. **13**, 68 (1975).

[181] H. Perrin: *Lecture 2 Doppler cooling and magneto-optical trapping* (2012).

[182] H. J. Metcalf and P. van der Straten: *Laser Cooling and Trapping* (2007).

[183] J. Dalibard and C. Cohen-Tannoudji: *Laser cooling below the Doppler limit by polarization gradients: simple theoretical models* (1989).

[184] P. J. Ungar, D. S. Weiss, E. Riis, and S. Chu: *Optical molasses and multilevel atoms: theory*, J. Opt. Soc. Am. B **6**, 2058 (1989).

[185] C. N. Cohen-Tannoudji and W. D. Phillips: *New Mechanisms for Laser Cooling*, Phys. Today **43**, 33 (1990).